

**Computational Wavefront Sensing:
Theory, Practice, and Applications**

Dissertation by

Congli Wang

In Partial Fulfillment of the Requirements

For the Degree of

Doctor of Philosophy

King Abdullah University of Science and Technology

Thuwal, Kingdom of Saudi Arabia

June, 2021

EXAMINATION COMMITTEE PAGE

The dissertation of Congli Wang is approved by the examination committee.

Committee Chairperson: Prof. Wolfgang Heidrich

Committee Members: Prof. Bernard Ghanem, Prof. Peter Wonka, Prof. Laura Waller

©June, 2021

Congli Wang

All Rights Reserved

ABSTRACT

Computational Wavefront Sensing: Theory, Practice, and Applications

Congli Wang

Wavefront sensing is a fundamental problem in applied optics. Wavefront sensors that work in a deterministic manner are of particular interest. Initialized with a unified theory for classical wavefront sensors, this dissertation discusses relevant properties of wavefront sensor designs. Based on which, a new wavefront sensor, termed Coded Wavefront Sensor, is proposed to leverage the advantages of the analysis, especially the lateral wavefront resolution. A prototype was built to demonstrate this new wavefront sensor.

Given that, two specific applications are demonstrated: megapixel adaptive optics and simultaneous intensity and phase imaging. Combined with a spatial light modulator, a hardware deconvolution approach is demonstrated for computational cameras via a high resolution adaptive optics system. By simply switching the normal image sensor with the proposed one, as well as slight change of illumination, a bright field microscope can be configured to a simultaneous intensity and phase microscope. These show the broad application range of the proposed computational wavefront sensing approach.

Lastly, this dissertation proposes the idea of differentiable optics for wavefront engineering and lens metrology. By making use of automatic differentiation, a physically-correct differentiable ray tracing engine is built, with its potentials being illustrated via several challenging applications in optical design and metrology.

ACKNOWLEDGEMENTS

It has always been my great pleasure and fortune, to work and finish my MS and PhD under the supervision of Prof. Wolfgang Heidrich. I am thankful to his vision, guidance, and patience throughout my development as a junior researcher. I am highly appreciate that Prof. Heidrich gave me a total freeform to explore new research topics and opportunities. I benefit a lot from his taste, insight, knowledge, and thought process, in computations, optics, and graphics. I am grateful to being shaped by Prof. Heidrich.

I am grateful to KAUST, for this beautiful and revolutionary institute to offer me a worry-free life, allowing me to focus on research. I would also like to express my gratitude to the Visual Computing Center for all the generous supports.

I would like to thank all my wonderful friends and colleagues at the VCC Imaging Lab. I am grateful to my collaborators, Dr. Qiang Fu, Dr. Xiong Dun, and Dr. Ni Chen, for their helpful discussions and guidance. Dr. Fu fabricated the coding mask, he with Dr. Dun helped me with some of the initial optical setups and debugging. I learned from them. It is also my great luck to have Dr. Chen as a close collaborator to work together on interesting holography projects.

I would also like to thank my friends inside and outside the lab, who have made my years at KAUST enjoyable. Thank Dong Lao, Jinhui Xiong, Qilin Sun, Guangming Zang, Peihao Li, Tianbo Chen, and many others for the company and helps. I am also thankful to friends in industry who helped me in job seeking.

Finally, I would like to thank my family for their love and support throughout the years. I hope that this dissertation will summarize my efforts in the field of wavefront sensing, by making a tiny contribution to the optical society.

TABLE OF CONTENTS

Examination Committee Page	2
Copyright	3
Abstract	4
Acknowledgements	5
List of Abbreviations	10
List of Figures	11
List of Tables	13
1 Introduction	14
1.1 Overview	15
1.2 Dissertation structure	17
2 Background and Related Work	19
2.1 General wavefront sensing techniques	19
2.1.1 Background-oriented Schlieren	19
2.1.2 Wavefront sensors	20
2.1.3 Light field cameras	21
2.2 Proximal algorithms	21
2.2.1 Proximal operator	22
2.2.2 Alternating Direction Method of Multipliers (ADMM)	22
3 Theory and Practice	24
3.1 Introduction	24
3.2 Theory	25
3.2.1 Ray optics derivations	26
3.2.2 Connection to previous formulas	27
3.2.3 Lateral wavefront resolution and numerical conditioning analysis . .	31

3.2.4	Simulation	34
3.2.5	Discussion	37
3.3	Practice	38
3.3.1	Hardware prototype	38
3.3.2	Decoding algorithm	38
3.3.3	Simulation	40
3.3.4	Realistic wavefront sensing	42
3.3.5	Discussion	43
3.4	Conclusion	44
4	Application: Megapixel Adaptive Optics	45
4.1	Introduction	45
4.2	Related work	48
4.2.1	Coded apertures and image deblurring	48
4.2.2	Coded wavefront sensors	48
4.2.3	Adaptive optics	49
4.3	Megapixel adaptive optics	50
4.3.1	Closed loop adaptive optics	50
4.3.2	Wavefront solver	52
4.4	Prototype	56
4.4.1	Hardware	56
4.4.2	Software	58
4.5	Results	62
4.5.1	Simulation	63
4.5.2	Real experiments	65
4.6	Discussion and conclusion	67
5	Application: Intensity and Phase Microscopy	70
5.1	Introduction	70
5.2	Masked sensor for intensity and phase microscopy	73
5.2.1	Sensor principle	73
5.2.2	Simultaneous intensity and phase reconstruction	74
5.2.3	Computation	76
5.3	Results	82
5.3.1	Characterization of a microlens array	82
5.3.2	Influence of irradiance-varying samples	83
5.3.3	Imaging of transparent cells	85

5.3.4	Digital refocusing	85
5.4	Analysis and calibration	87
5.4.1	Wavefront resolution analysis	87
5.4.2	Calibration	89
5.5	Discussion and conclusion	90
5.5.1	Discussion	90
5.5.2	Conclusion	91
6	Differentiable Lens Design	92
6.1	Introduction	93
6.2	Differentiable lens design engine	95
6.2.1	Lens design with automatic differentiation	95
6.2.2	Lens system	96
6.2.3	Ray tracing engine	98
6.2.4	Image rendering from intersections	100
6.2.5	Implementation	102
6.3	Optimization	103
6.3.1	Unconstrained optimization methods	104
6.3.2	Constraint handling	105
6.4	Classical applications	106
6.4.1	Design optimization	106
6.4.2	Tolerance analysis	107
6.5	Advanced applications	109
6.5.1	Caustic engineering	109
6.5.2	End-to-end wavefront coding	110
6.5.3	Misalignment estimation	111
6.6	Discussion and conclusion	113
6.6.1	Discussion	113
6.6.2	Conclusion	115
7	Differentiable Refractive Deflectometry for Lens Metrology	116
7.1	Introduction	116
7.2	Method	118
7.3	Results	122
7.3.1	Simulation results	122
7.3.2	Experimental results	122
7.4	Discussion and conclusion	125

8 Concluding Remarks	127
8.1 Summary	127
8.2 Future work	127
References	129
Appendices	151
A Formulas and Derivations	151
A.1 Diffraction formulas	151
A.2 Wave optics derivations	153
B Parameterized Optical Surfaces	158
B.1 Aspheres	158
B.2 XY polynomials	159
B.3 B-splines	159
C Publications and Submissions	161

LIST OF ABBREVIATIONS

ADMM	Alternating Direction Method of Multipliers
AO	Adaptive Optics
BOS	Background Oriented Schlieren
CCD	Charge-Coupled Device
CMM	Coordinate Measuring Machine
DCT	Discrete Cosine Transforms
DIC	Differential Interference Contrast
FFT	Fast Fourier Transforms
FOV	Field of View
GPU	Graphics Processing Unit
LASSO	Least Absolute Shrinkage and Selection Operator
LCoS	Liquid Crystal on Silicon
MSE	Mean Square Error
NA	Numerical Aperture
OPD	Optical Path Difference
PSF	Point Spread Function
RMS	Root Mean Square
SLM	Spatial Light Modulator
SNR	Signal-to-Noise Ratio
TIE	Transport of Intensity Equation

LIST OF FIGURES

1.1	Definition of a wavefront.	14
3.1	General single-shot wavefront sensor model.	25
3.2	Image formation model for deterministic wavefront sensors (single-shot). .	27
3.3	Image formation model revised for deriving TIE (dual-plane).	28
3.4	Wavefront transfer function for different optics-sensor distance z configurations.	32
3.5	Errors of different formulas for a Gaussian wavefront propagating through z . .	35
3.6	Errors of different formulas for a real-captured cheek cell wavefront propagating through z	36
3.7	Prototype Coded Wavefront Sensor.	38
3.8	Accuracy experiments	41
3.9	Synthetic atmospheric turbulence	42
3.10	Wavefront visualization of the heat flow and the defocusing.	42
4.1	Megapixel AO for large distortion corrections in vision applications.	46
4.2	Adaptive optics system hardware schematic and control diagram.	51
4.3	Principle of the Coded Wavefront Sensor.	52
4.4	Comparison between our ADMM solver and conjugate gradient method.	54
4.5	The proposed warping scheme wavefront solver enables an improved estimation accuracy.	56
4.6	2D and 3D profile of the central area on the fabricated binary phase mask taken with Zygo NewView 7300.	57
4.7	Our high resolution AO prototype setup.	58
4.8	Adding a longpass filter in front of the guide star to suppress it from being visible to the vision camera.	58
4.9	Bilateral filtering of detected wavefront and the accumulated SLM phase. .	60
4.10	Calibration of inverse misalignment transform \mathbf{D}^{-1}	61
4.11	Synthetic comparison of large wavefront distortions corrected by AO systems with different wavefront sensors and correctors.	64
4.12	PSF experiment with test phase generated on the SLM.	65
4.13	Static deblurring for large distortions.	66
4.14	Comparison of our AO approach with software-only methods.	67

4.15 Anisoplanatism.	68
5.1 Quantitative phase imaging with a coded wavefront sensor.	73
5.2 Accuracy validation measurement using a microlens array.	83
5.3 Phase reconstruction comparison for an air-dried human red blood cell smear using different methods.	84
5.4 Experimental results with unstained thin transparent cells with the proposed quantitative phase imaging pipeline.	86
5.5 Post-capture refocusing by digitally propagating defocus distance Δf with the acquired complex field.	87
5.6 Wavefront resolution analysis and the phase transfer function.	89
5.7 Calibration of wavefront sensor scaling factor.	90
6.1 A lens parameterized by its first surface curvature θ is under investigation. .	96
6.2 Lens system schematic and its prescription file.	96
6.3 Root-finding solver via Newton's method for ray-surface intersection. . . .	99
6.4 Memory consumption comparison between two computation methods. . . .	99
6.5 Differentiable reconstruction filter is crucial in the forward tracing mode. .	101
6.6 Our versatile tracing engine can produce photorealistic renderings.	102
6.7 Entrance pupil calculation.	103
6.8 Spot diagrams of our engine highly resemble those by Zemax.	103
6.9 Spherical aberration minimization.	106
6.10 Nikon lens group total aberration minimization.	107
6.11 Tolerancing a nominal lens system.	108
6.12 Overview of advanced applications.	109
6.13 Caustic engineering.	110
6.14 Our differentiable engine can perform end-to-end wavefront coding. . . .	112
6.15 A differentiable engine can be employed to back-engineer setup misalignment parameters.	114
7.1 Dual-camera refractive deflectometry for lens metrology.	119
7.2 Assuming pinhole camera model and planar screen, our ray tracer reproduces real captured images in high fidelity.	120
7.3 Lens curvature $\theta = (c_1, c_2)$ metrology using synthetic data.	123
7.4 Freeform lens metrology using synthetic data.	123
7.5 Experimental lens curvature metrology for LE1234.	125
7.6 Experimental asphere-freeform lens metrology.	126

LIST OF TABLES

3.1	Optics and corresponding reference image of different wavefront sensors.	25
3.2	Theoretical models used in classical wavefront sensing research.	28
4.1	Performance characteristics of different wavefront sensing technologies.	46
4.2	Software performance of our algorithm (1024×1024 unknowns).	62
6.1	Differentiable parameters of the aspherical surface.	106
7.1	Experimental singlet lens curvature metrology results.	124

Chapter 1

Introduction

In optics, an optical wavefront is the locus of points propagating with the same phase. By definition, wavefront is only meaningful under purely coherent conditions, either spatially coherent (lighting from a single source) or temporally coherent (phases of light synchronize in time). Figure 1.1 visualizes the definition of a wavefront in wave and ray representations, where a plane wave is transformed into a spherical wave by a thin lens. Here, a wavefront is defined as a manifold curve along the propagation direction. An equivalent ray representation illustrates the same optical phenomenon.

Wavefront representation is an important criteria for characterizing imaging quality and quantifying aberration. Consequently, wavefront gives a sense for engineers to understand optical systems, alerting potential performance decrease for specific tasks. For example, perfect imaging requires a spherical wavefront, and hence the actual wavefront deviation defines more or less the degree of aberration of an imaging system. Once wavefront is measured, advanced techniques may be employed to improve imaging quality, *e.g.*, using

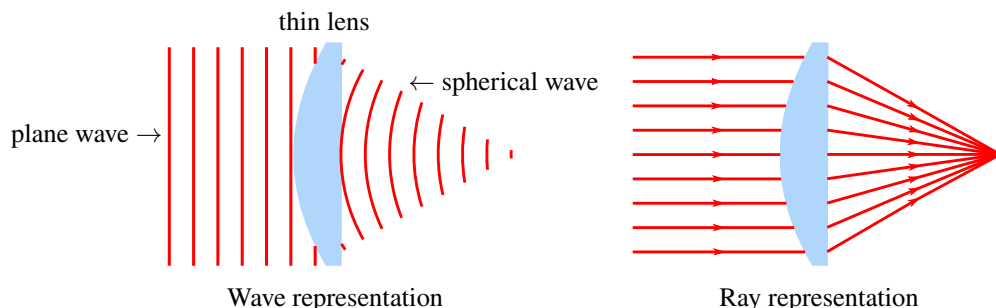


Figure 1.1: Definition of a wavefront. Wavefront are manifold curves where the wave has the same phase of the underlying electromagnetic sinusoidal field. Alternative ray representation depicts local directions that are orthogonal to the wavefront surface.

adaptive optics or computational deconvolution algorithms.

Wavefront is also useful when examining thin transparent biological samples. In this scenario, wavefront is ordinarily referred as optical phase, *i.e.*, the phase delay of the considered electromagnetic radiation. These biological samples are difficult to examine using normal bright field microscopy, because illumination light propagates directly through the transparent sample, with only slight angular shifts and almost no change of radiance, and hence special microscopes are required. Quantitative phase imaging is one of the useful specific techniques to acquire phase, *i.e.*, wavefront, to reveal sample biological structures.

The problem of characterizing wavefront is called wavefront sensing. Since imaging sensors are sensitive to irradiance but not ray directions, wavefront cannot be directly measured, and hence proper hardware revision is necessary in order to acquire wavefront. A wavefront sensor is such a specialized instrument to measure optical wavefront.

This dissertation introduces a new computational imaging approach to wavefront sensing, and proposes a new wavefront sensor called the Coded Wavefront Sensor. A unified theoretical framework is derived to understand the sensor principle, as well as for classical wavefront sensors. Several practical applications are demonstrated using the proposed sensor. These works comprise the majority of this dissertation.

In spite of wavefront measurement, wavefront engineering is also considered in this dissertation. Modern machine learning techniques are leveraged to this purpose, and a general differentiable ray tracing framework is proposed for both lens design and metrology.

1.1 Overview

This dissertation focuses on wavefront sensing and relevant applications.

Coded wavefront sensor [1] is a novel single-shot, high spatial wavefront resolution sensor that we proposed. The sensor itself, like Shack-Hartmann, consists of a coding optic and a bare image sensor. In [1], we chose the fabrication-friendly binary amplitude mask as the coding optics, which was placed in a close proximity to the sensor, at a distance z

approximately equals 1.5 mm. The binary mask serves as a wavefront modulator, in that the perceived images under plane wave illumination are quasi-random speckles, denoted as $I_0(\mathbf{x})$, with \mathbf{x} being the pixel coordinate. When input is a distorted wavefront $\phi(\mathbf{x})$ (in the unit of optical path differences), the speckle pattern image distorts, denoted as $I(\mathbf{x})$. The distortion displacements from $I_0(\mathbf{x})$ to $I(\mathbf{x})$ are proportional to both mask-to-sensor distance z and wavefront slopes $\nabla\phi$, mathematically written as:

$$I(\mathbf{x} + z\nabla\phi) = I_0(\mathbf{x}). \quad (1.1)$$

We developed a curl-free optical flow algorithm to solve $\phi(\mathbf{x})$ out of $I_0(\mathbf{x})$ and $I(\mathbf{x})$. In theory, if the algorithm is smart-enough to distinguish all displacements, $\phi(\mathbf{x})$ is at sensor resolution. The algorithm is highly parallelizable, and a CUDA implementation runs in real-time for megapixel image resolution at 30 Hz on a gaming laptop.

Megapixel adaptive optics [2] is an Adaptive Optics (AO) application of [1]. Since $\phi(\mathbf{x})$ is of megapixel, together with a megapixel Spatial Light Modulator (SLM), we built a closed-loop megapixel AO system to correct for large-scale wavefronts, on top of a vision camera system. All computations (wavefront solver, SLM control, AO loop) were implemented on a single Graphics Processing Unit (GPU), in either native CUDA code or based on OpenGL APIs (for display controls). Due to the slow response of the SLM liquid crystal, the AO prototype worked at 10 Hz. To improve light efficiency, we changed the amplitude mask in [1] to a binary phase mask of random patterns. We also revised the wavefront solver with a pyramid scheme to accelerate convergence for large-scale wavefronts, whose peak-to-valley values were usually at tens of wavelengths, and are usually beyond detection range of opponent sensors, *e.g.*, Shack-Hartmann wavefront sensor of a similar spatial resolution.

Quantitative phase and intensity microscopy [3] is a phase microscopy application of Coded Wavefront Sensor [1]. We switched the bare sensor with our wavefront sensor to complete this application. To tackle the varying amplitudes of biological samples, we re-

vised Eq. (1.1) to include an unknown sample amplitude $|A(\mathbf{x})|$:

$$I(\mathbf{x} + z\nabla\phi) = |A(\mathbf{x})|^2 I_0(\mathbf{x}). \quad (1.2)$$

Solving simultaneously the amplitude $|A(\mathbf{x})|$ and wavefront $\phi(\mathbf{x})$ leads to results of intensity and phase maps. Since new variables need to be solved, the new GPU solver ran at 10 Hz per megapixel frame.

Modeling classical wavefront sensors [4] analyzes the diffraction effect behind Eq. (1.2). We established a general theoretical framework for all classical wavefront sensors. Given the framework, we analyzed the modeling accuracy of Eq. (1.2) and gave an upper bound for spatial lateral wavefront resolution regarding z .

Differentiable ray tracer [5] proposes and builds a differentiable lens system using automatic differentiation, via which custom optimizer and data-driven machine learning techniques are employed for a board number of applications, including classical applications such as design optimization and sensitivity analysis, and advanced applications such as caustic engineering, end-to-end wavefront coding, and misalignment calibration.

Self-calibrated differentiable refractive deflectometry [6] takes one more step beyond [5]. We reversed the purpose of the differentiable ray tracer and employed it for lens metrology, using phase-shifting deflectometry in the refractive mode. The framework is self-calibrated, and we were able to estimate lens curvatures and asphere/freeform surfaces.

1.2 Dissertation structure

In the remainder of this dissertation, Chapter 2 gives a brief background for wavefront sensing techniques, optimization, and related work. Next, Chapter 3 represents a theoretical analysis for general wavefront sensors, aiming to understand and unify the performance characteristics of different wavefront sensors types, along with the introduction of a new type of wavefront sensor that maximizes the previously analyzed criteria, and practical us-

age is demonstrated for the proposed sensor. Two applications are later described using the proposed sensor. In Chapter 4, a megapixel adaptive optics system is built for computational cameras to do hardware deblurring. In Chapter 5, a quantitative phase microscopy application is demonstrated. These chapters establish a knowledge structure of the proposed wavefront sensor, from theory to practice, and to applications.

Starting from Chapter 6 and Chapter 7, we step out of the comfort zone of the current wavefront sensing technique, and focus on wavefront engineering and lens metrology, which are classical problems that could be formulated in a parametric way. We propose the concept of a differentiable lens, where a differentiable ray tracing system is built based on automatic differentiation and a differentiable renderer, via which data-driven machine learning techniques are employed for: (i) Differentiable lens design for task-specific applications in Chapter 6, and (ii) Optical element metrology in Chapter 7.

Finally, we conclude this dissertation with future research points in Chapter 8.

Chapter 2

Background and Related Work

2.1 General wavefront sensing techniques

In this section, we briefly review techniques that enable wavefront information acquisition. To be general, these techniques are not necessarily limited to wavefront sensors.

A general non-interferometric wavefront sensing system consists of three parts: a (partially coherent) light source, sensing optics, and an image sensor. To encode wavefronts into image measurements, one may opt for either illumination-side or sensor-side coding, as the duality reflects.

2.1.1 Background-oriented Schlieren

Illumination-side coding techniques include differential phase contrast and variants [7, 8, 9], Fourier ptychography [10], background illumination [11], and many others, including Schlieren imaging.

Schlieren imaging is a qualitative technique for flow visualization. Background Oriented Schlieren (BOS) [12] is an improved variant of Schlieren imaging, with the goal of reducing unnecessary optical components as well as acquiring quantitative information. In BOS, a textured background is placed at the back of the testing subject, with a vision camera measuring the background pattern. When there is flow motion, a computer algorithm tracks the spatial distortion of the background pattern as a result of the motion. This spatial distortion indicates local flow movement compared to the static state, and hence encodes the optical path difference information. Technical variants of BOS have been successfully

applied, to detect tomography gas flows [13] or to visualize refractive indexes [14]. The proposed Coded Shack-Hartmann wavefront sensor in this dissertation, shares similarity with the BOS technique, in that the background pattern is now placed from the object side to the sensor side, as a foreground instead.

2.1.2 Wavefront sensors

Sensor-side coding, on the other hand, employs a point light source (so-called guide star) or annular illumination [15], in company with custom optics or moving elements to encode wavefronts onto the image sensor, including Shack-Hartmann [16] or Hartmann masks [17], pyramid sensors [18], lateral shearing interferometry gratings [19, 20], curvature sensors [21, 22, 23], speckle-enhanced sensing based on Transport of Intensity Equation (TIE) [24, 25] and speckle-tracking sensors [26, 27, 28, 29, 1, 30, 3].

Wavefront sensing using speckle tracking technique was first proposed in X-ray phase imaging [26, 31, 28, 27, 32], and then for optical wavefront retrieval [1, 30], adaptive optics [2], and trial lens metrology [33]. Simultaneous reconstruction for absorption, phase, and dark field images from one single speckle-pattern measurement image have also been shown [29, 34, 35]. This speckle tracking technique can be regarded as a generalization of Shack-Hartmann [16] or Hartmann masks [36]. Closely related special cases are the shearing interferometers [37, 38] and variants [19, 20, 39, 40, 41] that enable closed-form solutions in Fourier domain for wavefront retrieval.

The classical Shack-Hartmann wavefront sensor [16] tracks the 2D motion of focus spots generated by a microlens array to recover the unknown wavefront slopes. It offers high frame rates, but the spatial wavefront resolution is limited to the number of lenslets. High spatial resolution (*e.g.* 2×2 pixels per lenslet in Altair [42]) can be achieved by increasing the number of lenslets, but proportionally at the cost of decreased ability to measure large wavefront slopes. Similar tradeoffs exist for other slope-tracing wavefront sensors, for example the pyramid wavefront sensors [18] and the quadriwave lateral shearing interfero-

metric wavefront sensors [43, 17].

On the other hand, curvature wavefront sensors [22], based on TIE [21], offer full sensor spatial wavefront resolution at high frame rates. Typical curvature sensors require coherent illumination and mechanical scanning to obtain multiple images for later computational phase reconstruction [44]. There has been work on curvature wavefront sensing using a single color sensor [45], exploiting the lens chromatic aberration, and thus avoiding the mechanical scanning. Interferometric wavefront sensors also require coherent illumination and a complicated setup with highly sensitive alignment.

2.1.3 Light field cameras

The light field is a function that describes the amount of light flowing from one point in each direction [46, 47]. As such, light fields are normally employed in an incoherent light setting, in the framework of ray optics, and at most first-order wave optics [48]. Intrinsically speaking, the trajectory of a wavefront is an angular-spatial slice of a light field.

Light field cameras are devices to capture light fields, and they are closely related to wavefront sensors. One of the core benefits of light field cameras is the ability to refocus images post-capture [49]. Light field cameras typically consist of multiple lenses, either camera lenses or microlens arrays, *e.g.*, [50, 51]. This layout is similar to the design spirit of a Shack-Hartmann sensor [16]. Recent works on light field cameras replace the microlens array with specifically designed modulators, for example using amplitude masks [52, 53, 54], a single diffuser [55], or from a partially wetted window with water drops [56].

2.2 Proximal algorithms

In this dissertation, most of the time we are trying to solve an optimization problem. This turns to the question of finding appropriate solvers. We rely on proximal algorithms and variants [57, 58, 59]. Proximal algorithms can be used to solve complex optimization problems by splitting different regularization terms into several smaller yet easier sub-problems

that are independently solved, and then combined to find a solution to the original problem.

2.2.1 Proximal operator

These sub-problems are oftentimes formulated in the form of proximal operator [59]:

$$\mathbf{prox}_{\mu f}(\mathbf{u}) \triangleq \arg \min_{\mathbf{x}} f(\mathbf{x}) + \frac{1}{2\mu} \|\mathbf{x} - \mathbf{u}\|^2. \quad (2.1)$$

Proximal operators are of importance for proximal algorithms. Fortunately, many functions (even for non-smooth functions, *e.g.* ℓ_1 -norm) have a closed form proximal operator. This offers great advantage for implementation of proximal algorithms.

2.2.2 Alternating Direction Method of Multipliers (ADMM)

Consider the following unconstrained optimization problem:

$$\underset{\mathbf{x}}{\text{minimize}} \quad f(\mathbf{x}) + g(\mathbf{Kx}), \quad (2.2)$$

where $f(\mathbf{x}) : \mathbb{R}^N \rightarrow \mathbb{R}$, linear operator $\mathbf{K} \in \mathbb{R}^{M \times N}$, and $g : \mathbb{R}^M \rightarrow \mathbb{R}$ is proxiable function (*i.e.* $\mathbf{prox}_{\lambda g}(\cdot)$ exists and is easy to evaluate). Eq. (2.2) can be solved by proper splitting, such as:

$$\begin{aligned} & \underset{\mathbf{x}, \mathbf{z}}{\text{minimize}} \quad f(\mathbf{x}) + g(\mathbf{z}), \\ & \text{subject to} \quad \mathbf{z} = \mathbf{Kx}. \end{aligned} \quad (2.3)$$

Using Alternating Direction Method of Multipliers (ADMM) [57], Eq. (2.3) can be solved using Algorithm 1.

For convex problems in the form of Eq. (2.2), the convergence of Algorithm 1 can be shown under some easily satisfied assumptions [57]. Throughout this dissertation, we will assume our model automatically satisfies such assumptions for convergence.

The importance of Algorithm 1 is that the original optimization problem is split into two relatively easier sub-problems, and each of them is solved in alternation. For each sub-

Algorithm 1: ADMM for solving Eq. (2.3).

```

1 Initialize  $\mathbf{x}^0$  and  $\mathbf{u}^0$ , set  $\lambda > 0$  and  $K$ 
2 for  $k = 0, 1, \dots, K - 1$  do
3   x-update:  $\mathbf{x}^{k+1} = \arg \min_{\mathbf{x}} f(\mathbf{x}) + \frac{1}{2\lambda} \|\mathbf{Kx} - \mathbf{z}^k + \mathbf{u}^k\|_2^2$ 
4   z-update:  $\mathbf{z}^{k+1} = \text{prox}_{\lambda g}(\mathbf{Kx}^{k+1} + \mathbf{u}^k)$ 
5   u-update:  $\mathbf{u}^{k+1} = \mathbf{u}^k + \mathbf{Kx}^{k+1} - \mathbf{z}^{k+1}$ 
6 end

```

problem, usually there exist fast direct solvers (for example, circular structure linear systems can be efficiently solved by Fourier methods), or have closed form solutions (for example, evaluation of ℓ_1 -norm proximal operator).

One great benefit of splitting is parallelization. When speed is an important issue, distributed computation blocks (*e.g.* GPU) heavily accelerate specific applications, however this requires separability of the applied algorithm. Algorithm 1 fulfills separability, as long as the two sub-problems are parallelizable.

It is worth noting that there exists other also important optimization frameworks besides ADMM, *e.g.* proximal point algorithm [60], forward-backward splitting [61], the Pock-Chambolle algorithm [58], the split Bregman [62], ISTA [63] and FISTA [64], and half-quadratic splitting [65]. For other types of primal-dual optimization techniques, please refer to a review paper by Komodakis and Pesquet [66].

Chapter 3

Theory and Practice

This chapter initializes a general theory for classical wavefront sensors, aiming to provide a theoretical formulation for wavefront sensors. Based on the theoretical criteria, a prototype masked sensor is demonstrated to maximize wavefront sensing capability.

We present an image formation model for deterministic phase retrieval in propagation-based wavefront sensing, unifying analysis for classical wavefront sensors such as Shack-Hartmann (slopes tracking) and curvature sensors (based on TIE). We show how this model generalizes commonly seen formulas, including TIE, from small distances and beyond. Using this model, we analyze theoretically achievable lateral wavefront resolution in propagation-based deterministic wavefront sensing. Finally, via a prototype masked wavefront sensor, we show realistic wavefront measurements.

3.1 Introduction

We refer to classical wavefront sensors as deterministic, sensor-side coded wavefront sensors under collimated illumination. These wavefront sensors are considered as deterministic for phase retrieval, since their image formation models are simple and numerically easy to invert. However, deterministic models are usually considered separately for different wavefront sensors, for example using centroid tracking (slope tracking) for modeling Shack-Hartmann sensors, or using the TIE for modeling curvature sensors.

In this work, we model classical wavefront sensors in a unified framework, extending our conference paper [67] with extended analysis and results. We consider wavefront sensors

working under collimated white light illumination with sensor-side coding using custom optics. Figure 3.1 shows such a general modeling of single-shot or dual-plane wavefront sensors, where an optical element (*e.g.*, a microlens array, or a phase mask, see Table 3.1 for examples) is placed distance z in front of a bare image sensor. Two images are captured, one without the sample (reference image $I_0(\mathbf{r})$), another with the sample (measurement image $I(\mathbf{r})$). A numerical solver recovers the unknown wavefront $\phi(\mathbf{r})$ from image pair $I_0(\mathbf{r})$ and $I(\mathbf{r})$. In Section 3.2, we derive a formula relating $I_0(\mathbf{r})$ and $I(\mathbf{r})$.

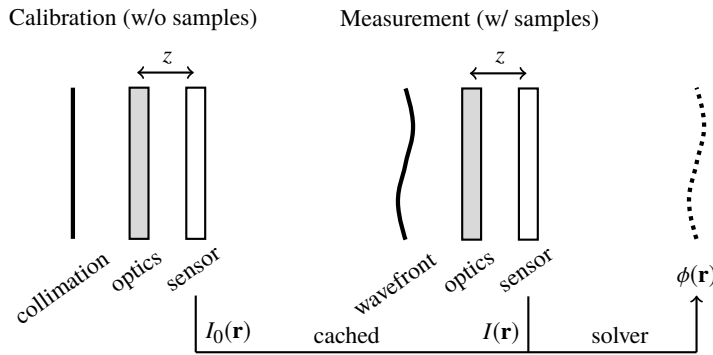


Figure 3.1: General single-shot wavefront sensor model. The unknown wavefront $\phi(\mathbf{r})$ is numerically solved from cached $I_0(\mathbf{r})$ and single-shot measurement $I(\mathbf{r})$.

Table 3.1: Optics and corresponding reference image of different wavefront sensors. $\delta_p(x)$ is the Dirac comb function with period p (the lenslet or pinhole pitch). $\mathbf{r} = (x, y)$.

Name	Optics	Reference image $I_0(\mathbf{r})$
Shack-Hartmann [16] / Hartmann mask	micro-lens arrays / pinhole arrays	$\delta_p(x)\delta_p(y)$
Lateral shearing [20]	sinusoidal gratings (freq. ω)	$\cos^2(\omega x)\cos^2(\omega y)$
Curvature sensor [22]	none	1
Coded wavefront sensor [1, 30]	random gratings or diffusers	random speckles

3.2 Theory

In this section we derive a new image formation model for general wavefront sensors in Figure 3.1, and discuss its relationship with previous models.

3.2.1 Ray optics derivations

Damberg and Heidrich [68] proposed a warping based phase optimization image formation model for computational lens design, in which the core idea is that the energy conservation law is valid in each local differentiable area, and consequently a ray optics based formula is derived relating caustic images and the freeform lens. Similar approach has been proposed in [69] to yield the same result as in [68], including higher order terms. Here, we revisit these approaches to further account for sample absorption $A(\mathbf{r})$ and general custom optics (*i.e.*, different $I_0(\mathbf{r})$) as in Table 3.1, resulting in a ray optics model for general classical wavefront sensors. See Appendix A.2 for more details from a wave optics perspective.

In the following, we assume ray optics, in that the optical field of interest is fully incoherent. Specifically, we consider plane wave illumination onto the wavefront sensor, and denote the reference image as $I_0(\mathbf{r})$. This reference image is different from sensor-to-sensor, is design-dependent, and is only relevant to the coding optics placed in front of the image sensor, as discussed in Table 3.1. Consider a sample impinges the wavefront sensor, with a non-uniform intensity $|A(\mathbf{r})|^2$ and a distortion wavefront $d(\mathbf{r})$ quantified in terms of Optical Path Difference (OPD). Here, the ray optics assumption forces the considered wavefront to be an “average” phase, and hence local ray deflection angles can be written as $\nabla d(\mathbf{r})$ where ∇ is the spatial gradient operator. Consider free space light propagation in Figure 3.2, for a paraxial single ray of interest ($\nabla d(\mathbf{r}) \ll 1$), we have:

$$\begin{aligned} \mathbf{r}' &= \mathbf{r} + z\nabla d(\mathbf{r}) & I(\mathbf{r}') \, d\mathbf{r}' &= |A(\mathbf{r})|^2 I_0(\mathbf{r}) \, d\mathbf{r}, \\ (\text{geometry relationship}) & & (\text{energy conservation}) & \end{aligned} \tag{3.1}$$

Rearranging yields

$$I(\mathbf{r} + z\nabla d(\mathbf{r})) = \frac{|A(\mathbf{r})|^2 I_0(\mathbf{r})}{1 + z\nabla^2 d(\mathbf{r})} \approx (1 - z\nabla^2 d(\mathbf{r})) |A(\mathbf{r})|^2 I_0(\mathbf{r}), \tag{3.2}$$

where the approximation is a consequence of the small local curvature assumption that

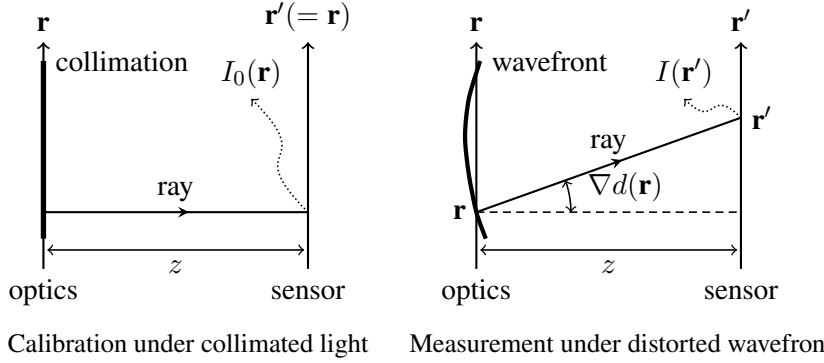


Figure 3.2: Image formation model for deterministic wavefront sensors (single-shot).

$z|\nabla^2 d(\mathbf{r})| \ll 1$, as required for near-field diffraction to hold (see Eq. (A.20) derived from Eq. (A.5) in Appendix A.2). When consider monochromatic illumination with a wavelength of λ , we may rewrite OPD $d(\mathbf{r}) = \lambda\phi(\mathbf{r})/(2\pi)$ where $\phi(\mathbf{r})$ is the wavefront, therefore

$$I\left(\mathbf{r} + \frac{\lambda z}{2\pi} \nabla \phi\right) = |A(\mathbf{r})|^2 \left(1 - \frac{\lambda z}{2\pi} \nabla^2 \phi\right) I_0(\mathbf{r}). \quad (3.3)$$

To convert OPD back to wavefront or phase, a nominal wavelength (*e.g.*, $\lambda = 500\text{ nm}$) can be used, as normally seen in other white light wavefront sensing techniques such as Shack-Hartmann. Equation (3.3) is the main model of this dissertation, and is a natural consequence of [68, 69]. Notice the derivation here is based on ray optics, and thus this formula works under broadband illumination, as been experimentally verified [3]. Our formula here could be thought as a variant of the generalized eikonal equation for partially coherent beams [70]. We made no specific assumptions about optics, thus Eq. (3.3) presumably works for all wavefront sensors in a similar configuration of Figure 3.1. Some examples are in Table 3.1.

3.2.2 Connection to previous formulas

We now see how Eq. (3.3) is connected to previous formulas for single-shot or dual-plane wavefront sensing. Table 3.2 summarizes these formulas, as will be discussed below.

Table 3.2: Theoretical models used in classical wavefront sensing research.

Model	Formula	Articles
Curvature sensing	$\nabla I \cdot \nabla \phi + I \nabla^2 \phi = -k \frac{\partial I}{\partial z}$	[21, 22, 23, 71, 72, 44, 73, 74]
Flow tracking	$I(\mathbf{r} + \frac{\lambda z}{2\pi} \nabla \phi) = I_0(\mathbf{r})$	[16, 27, 28, 32, 1, 30, 19, 40]
Amplitude-combined flow tracking	or $I(\mathbf{r}) = A(\mathbf{r}) ^2 I_0(\mathbf{r} - \frac{\lambda z}{2\pi} \nabla \phi)$	[20, 29, 39]
Zanette <i>et al.</i> 's model	$I(\mathbf{r}) = A(\mathbf{r}) ^2 [\bar{I}_0 + D(\mathbf{r}) \Delta I_0(\mathbf{r} - \frac{\lambda z}{2\pi} \nabla \phi)]$	[34]
Eq. (3.3) (this work)	$I(\mathbf{r} + \frac{\lambda z}{2\pi} \nabla \phi) = A(\mathbf{r}) ^2 (1 - \frac{\lambda z}{2\pi} \nabla^2 \phi) I_0(\mathbf{r})$	[68, 69, 3]

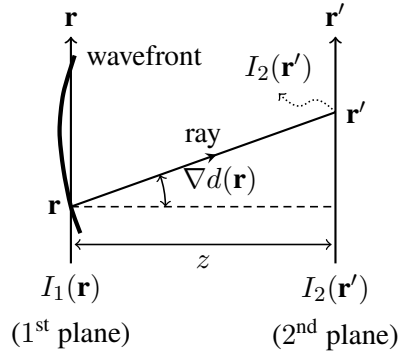


Figure 3.3: Image formation model revised from Figure 3.2 for deriving TIE (dual-plane).

Transport-of-Intensity Equation (TIE)

The well-known TIE, also known as the irradiance transport equation [21], serves as the basic principle for curvature wavefront sensors and variants [22, 23, 71, 72, 44, 73, 74]. We may revise the previous derivations carefully, by depicting a dual-plane TIE setup in Figure 3.3. The sensor measurements $I_1(\mathbf{r})$, $I_2(\mathbf{r})$ at the two planes can thus be formulated similarly by Eq. (3.1):

$$\mathbf{r}' = \mathbf{r} + z \nabla d(\mathbf{r}), \quad I_1(\mathbf{r}) = |A(\mathbf{r})|^2, \quad I_2(\mathbf{r}') \, d\mathbf{r}' = |A(\mathbf{r})|^2 \, d\mathbf{r}. \quad (3.4)$$

Simplifying above, and let the optical field be monochromatic of wavelength λ , with $d(\mathbf{r}) = \phi(\mathbf{r})/k$ where phase $\phi(\mathbf{r})$ is defined at wave number $k = \lambda/(2\pi)$, yields a variant of Eq. (3.3):

$$I_2 \left(\mathbf{r} + \frac{z}{k} \nabla \phi \right) \approx \left(1 - \frac{z}{k} \nabla^2 \phi(\mathbf{r}) \right) I_1(\mathbf{r}). \quad (3.5)$$

With an additional approximation, by 1st-order Taylor expanding $I_2(\mathbf{r} + \frac{z}{k}\nabla\phi)$ around \mathbf{r} , yields:

$$I_2\left(\mathbf{r} + \frac{z}{k}\nabla\phi\right) \approx I_2(\mathbf{r}) + \frac{z}{k}\nabla I_2 \cdot \nabla\phi. \quad (3.6)$$

With Eq. (3.5) and Eq. (3.6), we have:

$$\frac{I_2(\mathbf{r}) - I_1(\mathbf{r})}{z} = -\frac{1}{k} (\nabla I_2 \cdot \nabla\phi + \nabla^2\phi). \quad (3.7)$$

Notice the left hand side is a finite difference approximation when z is small. Let $z \rightarrow 0$, denote mean sample intensity as \bar{I} that $\bar{I} = |A(\mathbf{r})|^2 = I_1 \approx I_2$, we arrive at the standard TIE form:

$$\frac{\partial \bar{I}}{\partial z} = -\frac{1}{k} \nabla(\bar{I} \cdot \nabla\phi). \quad (3.8)$$

We just witnessed how the finite difference form of TIE can be derived from Eq. (3.3). As a result, we believe that Eq. (3.3) generalizes TIE to larger distances z , *i.e.*, to regions beyond the convergence radius of the 1st-order Taylor expansion, and hence beyond the finite difference range. It has been shown [44] that larger propagation distance z prevents high frequency information to be included in the finite form of TIE due to ignored diffraction in the derivation. This effect and limitation of the proposed model will be discussed in Section 3.2.3.

Flow tracking

By dropping the sample amplitude and wavefront curvature, Eq. (3.3) reduces to:

$$I\left(\mathbf{r} + \frac{\lambda z}{2\pi}\nabla\phi\right) = I_0(\mathbf{r}), \quad (3.9)$$

which we recognize as the famous optical flow formulation in computer vision [75], or the classical centroid tracking model for Shack-Hartmann, as well as the underlining model for previous speckle-pattern tracking phase imaging techniques [26, 27, 28, 32, 1, 30].

Amplitude-combined flow tracking

If dropping out only the wavefront curvature term, Eq. (3.3) reduces to

$$I \left(\mathbf{r} + \frac{\lambda z}{2\pi} \nabla \phi \right) = |A(\mathbf{r})|^2 I_0(\mathbf{r}), \quad (3.10)$$

which we recognize as models typically employed in X-ray phase imaging applications [29].

Another commonly seen formulation is

$$I(\mathbf{r}) = |A(\mathbf{r})|^2 I_0 \left(\mathbf{r} - \frac{\lambda z}{2\pi} \nabla \phi \right), \quad (3.11)$$

which can be derived by assuming $A(\mathbf{r} - \lambda z \nabla \phi / (2\pi)) \approx A(\mathbf{r})$ as in Eq. (A.24) of Appendix A.2.

Dark field model

It is worth noting that Eq. (3.3) only considers refraction and absorption effects, excluding scattering contributions, *i.e.*, the dark fields. Yet, we provide a connection to Zanette *et al.*'s dark field model [34], illustrating the feasibility of future development on Eq. (3.3). Zanette *et al.* [34] modified Eq. (3.11) by incorporating a dark field term $D(\mathbf{r})$ that represents a scattering contribution:

$$I(\mathbf{r}) = |A(\mathbf{r})|^2 \left[\bar{I}_0 + D(\mathbf{r}) \Delta I_0 \left(\mathbf{r} - \frac{\lambda z}{2\pi} \nabla \phi \right) \right], \quad (3.12)$$

where \bar{I}_0 is the mean value of $I_0(\mathbf{r})$, and $\Delta I_0(\mathbf{r}) = I_0(\mathbf{r}) - \bar{I}_0$. With Eq. (3.3), we know part of $D(\mathbf{r})$ originates from the caustic term $1 - \lambda z \nabla^2 \phi / (2\pi)$ that contains wavefront curvature $\nabla^2 \phi$, representing sample refraction under a distorted wavefront along z . Therefore, the dark field term $D(\mathbf{r})$ in Eq. (3.12) can be further refined to contain only scattering terms. As such, Eq. (3.3) provides new insights for incorporating dark field term into the image formation model.

3.2.3 Lateral wavefront resolution and numerical conditioning analysis

Based on Eq. (3.2), we would like to gauge the maximal lateral wavefront resolution that a wavefront sensor (*e.g.*, the ones in Table 3.1) can achieve, and under what condition would it be possible. In this section, we analyze what the roles of distance z and coding optics (as in Figure 3.1) are for a wavefront sensor. For a given optical system (fixed relay lens and pixel size), it turns out that distance z decides the theoretically achievable lateral wavefront resolution, whereas specific coding optics decide the numerical conditioning of the wavefront retrieval problem. In the remainder of this Chapter, without ambiguity, we refer to wavefront resolution as lateral wavefront resolution, *i.e.*, the spatial wavefront resolution.

Theoretical resolution bound by distance z

Recall the approximation conditions when deriving Eq. (3.3), in terms of OPD $d(\mathbf{r})$:

$$\nabla d(\mathbf{r}) \ll 1 \quad \text{and} \quad \nabla^2 d(\mathbf{r}) \ll \frac{1}{z}. \quad (3.13)$$

Using Eq. (3.13) as constraints, one can derive a wavefront (or OPD) transfer function $D(\boldsymbol{\rho})$ in terms of Fourier harmonics of frequency $\boldsymbol{\rho}$. Let $d(\mathbf{r}) = D(\boldsymbol{\rho}) \cos(2\pi \boldsymbol{\rho} \cdot \mathbf{r})$, and:

$$D(\boldsymbol{\rho}) \ll \frac{1}{2\pi|\boldsymbol{\rho}|} \min \left(1, \frac{1/z}{2\pi|\boldsymbol{\rho}|} \right) = \begin{cases} \frac{1}{2\pi|\boldsymbol{\rho}|} & \text{if } |\boldsymbol{\rho}| < \frac{1}{2\pi z}, \\ \frac{1}{4\pi^2 z|\boldsymbol{\rho}|^2} & \text{otherwise.} \end{cases} \quad (3.14)$$

Equation (3.14) fully characterizes the attainable wavefront resolution of classical wavefront sensors based on Eq. (3.3). From Eq. (3.14), at low frequencies, the wavefront transfer function is fixed regarding $|\boldsymbol{\rho}|$, whereas at high frequencies the transfer function depends on z . We now discuss how z affects Eq. (3.14). Let ρ_{\max} be the maximum frequency that a diffraction-limited broadband optical system can achieve. Thus, ρ_{\max} depends on the Numerical Aperture (NA) and the image sensor pixel size, and is not considered related to

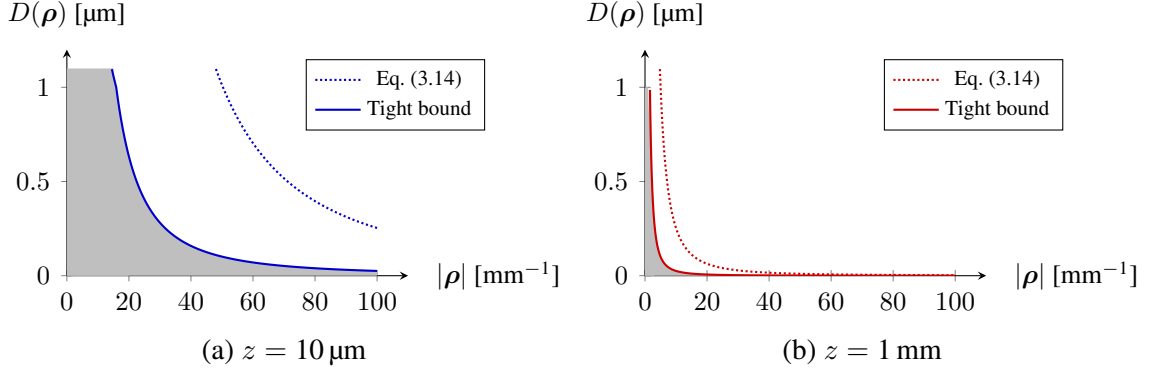


Figure 3.4: Wavefront transfer function for different optics-sensor distance z configurations. Area of valid regions (shaded) for Eq. (3.3) to hold decreases with an increase of z . This z - $|\rho|$ resolution trade-off applies to all classical wavefront sensors based on Eq. (3.3), especially for slope tracking sensors whose coding optics are usually mm away.

the coding optics employed by the wavefront sensor. As an example, for an image sensors of pixel pitch $\epsilon = 5 \mu\text{m}$, by Nyquist Theorem, $\rho_{\max} = 100 \text{ mm}^{-1}$. It thus requires $z \approx 0.628 \mu\text{m}$ such that $1/z > 2\pi\rho_{\max}$. This distance, however, is too small for practical slope tracking sensors, but explains typical μm level defocusing distances in previous studies of curvature sensing [45]. Finally, notice a similar bound was derived in [30] assuming non-overlapping speckles, which turns out to be a loose assumption that $\nabla^2 d(\mathbf{r}) \leq 1/z$.

To visualize Eq. (3.14), we draw $D(\rho)$ in Figure 3.4 for two different z configurations. To obtain a tight bound from Eq. (3.14), let equality be attained at 10 %, *i.e.*, $\nabla^2 d(\mathbf{r}) \leq 0.1/z$, denoted by the shaded regions in Figure 3.4. In other words, for Fourier harmonic OPD $d(\mathbf{r})$ within the shaded regions, Eq. (3.3) holds. Small z ($\approx 10 \mu\text{m}$, as in curvature sensing) achieves wavefront resolution at pixel sampling rate of 100 mm^{-1} , whereas larger z ($\approx 1 \text{ mm}$, as for most slope tracking sensors) achieves approximately $1/5$ pixel resolution in this case. Similar results have previously been obtained in experiments for speckle-tracking wavefront sensors [30, 3]. As a short conclusion, Eq. (3.14) defines the maximum theoretical resolution for classical deterministic phase retrieval wavefront sensors based on Eq. (3.3).

Numerical conditioning by coding optics

Previously we analyzed the theoretically achievable wavefront resolution for Eq. (3.3) to hold at a fixed distance z . We now discuss how coding optics (hence reference image $I_0(\mathbf{r})$) affects wavefront resolution in terms of numerical stability.

Recall we would like to solve $\phi(\mathbf{r})$ from Eq. (3.3) (or $d(\mathbf{r})$ from Eq. (3.2) equivalently), given $I_0(\mathbf{r})$ and $I(\mathbf{r})$. Unfortunately, sample intensity $|A(\mathbf{r})|^2$ and local wavefront curvature $\nabla^2\phi(\mathbf{r})$ are coupled (hence correlated), meaning we can only rely on estimating $\nabla\phi(\mathbf{r})$ for lateral recovery of $\phi(\mathbf{r})$. This property defines the basic principle for slope tracking wavefront sensors. As a result, one may reduce Eq. (3.3) to Eq. (3.10) or (3.11), either would provide the same analysis. For simplicity in terms of Eq. (3.11), by expanding the nonlinear term up to higher order terms (H.O.T.):

$$I_0(\mathbf{r}) - \frac{\lambda z}{2\pi} \nabla I_0(\mathbf{r}) \cdot \nabla\phi(\mathbf{r}) + \text{H.O.T.} \approx I(\mathbf{r})/|A(\mathbf{r})|^2. \quad (3.15)$$

To solve $\nabla\phi(\mathbf{r})$, for non-singular samples that $A(\mathbf{r}) \neq 0$, we identify a purely coding optics dependent diagonal linear system with diagonals as $\nabla I_0(\mathbf{r})$. Consider the condition number:

$$\kappa = \frac{\max |\nabla I_0(\mathbf{r})|}{\min |\nabla I_0(\mathbf{r})|}. \quad (3.16)$$

In terms of numerical stability, κ can be used as a figure of merit for the performance of the optics in Figure (3.1): the smaller κ , the better the optics chosen for slope tracking wavefront sensing. As such, the “best” optics would produce uniform gradients and $\kappa = 1$. However, this design is not practical due to limited dynamic range of image sensors (usually of 8 to 10 bits). The other extreme is the classical Shack-Hartmann sensor, for which the microlens array produces an array of bright with black background, and $\kappa \rightarrow \infty$. In this case, the effective wavefront resolution is limited to the number of microlenses, instead of the number of pixels.

3.2.4 Simulation

To verify the proposed formula Eq. (3.3), we simulate a curvature sensor propagating through varies distance z , assuming no optics in Figure 3.1. In other words, $I_0(\mathbf{r}) = 1$ in Eq. (3.3). In this way, we eliminate the influence of coding optics and evaluate only the physical correctness. In Figure 3.5, we simulate a Gaussian wavefront (peak-valley $\approx 24\lambda$) propagating through different z using the angular spectrum method [76, 77] at wavelength $\lambda = 550$ nm, pixel size $\epsilon = 5 \mu\text{m}$, under a sampling rate of $0.5 \mu\text{m} < \lambda$. With oversampling, numerical propagation error is small compared to model errors of interest here. Given $\phi(\mathbf{r})$ and the obtained $I(\mathbf{r})$ at different z , we numerically evaluate the absolute fitting errors of different formulas (TIE: Eq. (3.7); Flow: Eq. (3.10); Ours: Eq. (3.3)), with ℓ_1 -norm of the error maps shown in Figure 4(b). Image warpings are implemented using cubic spline interpolation with piece-wise spline coefficients computed from $I_0(\mathbf{r})$. As revealed by Figure 3.5, our formula maintains a low error throughout z range, whereas TIE fails for large z and flow-tracking formula fails for small z . This superior performance is the consequence of combining both TIE and flow-tracking as discussed previously. Notice all formulas start to fail for very large z because of diffraction, as a consequence of violating $\nabla^2 d(\mathbf{r}) \ll 1/z$ in Eq. (3.13).

Similarly in Figure 3.6, we simulate a real-captured cheek cell wavefront (dataset from [78]) propagated through different distance z , and evaluate the absolute fitting errors of different formulas. TIE and our formula produce almost the same error curves due to small wavefront slopes, and displacement is smaller than one pixel, $z |\nabla d(\mathbf{r})| < \epsilon$, justifying the linear Taylor approximation from Eq. (3.3) to TIE. As in Figure 3.5, both TIE and our formula fit well for small $z \leq 2$ mm. However, at large z , the assumption that $\nabla^2 d(\mathbf{r}) \ll 1/z$ does not hold anymore, and $I(\mathbf{r})$ appears blurry. As a result, both TIE and our formula produce large errors because the caustic term $1 - z\nabla^2 d(\mathbf{r})$ is not small and amplifies the defocusing error. From Figure 3.5 and Fig 3.6, we conclude our formula combines the advantage of both approaches for short distance z when Eq. (3.13) holds.

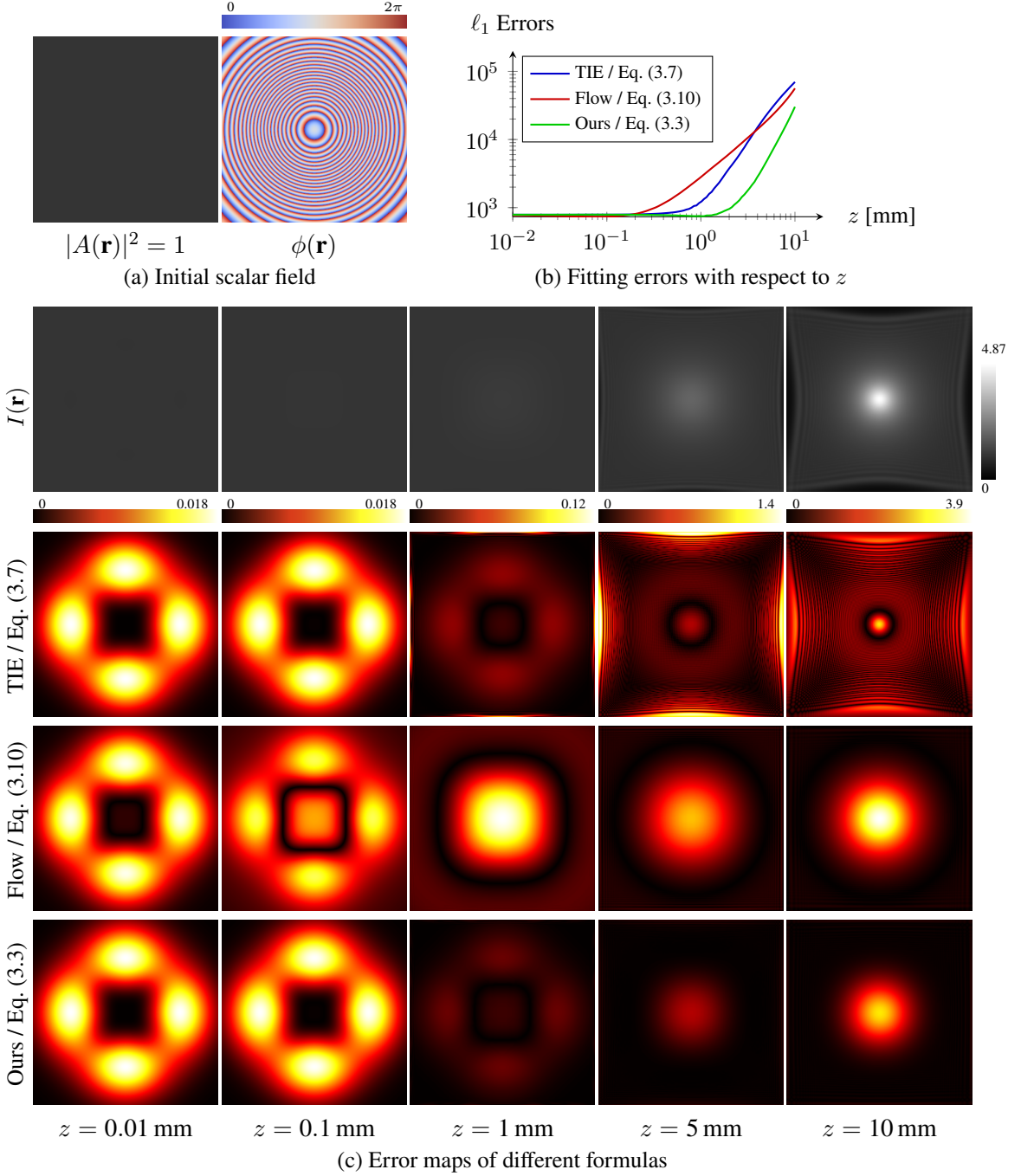


Figure 3.5: Errors of different formulas for a Gaussian wavefront propagating through z . As a mixed approach, our formula Eq. (3.3) outperforms alternative formulations in terms of ℓ_1 -fitting errors. With a gradual violation of ray optics and near field assumption (increasing z , and hence breaking of $\nabla^2 d(\mathbf{r}) \ll 1/z$), all formulas start to fail.

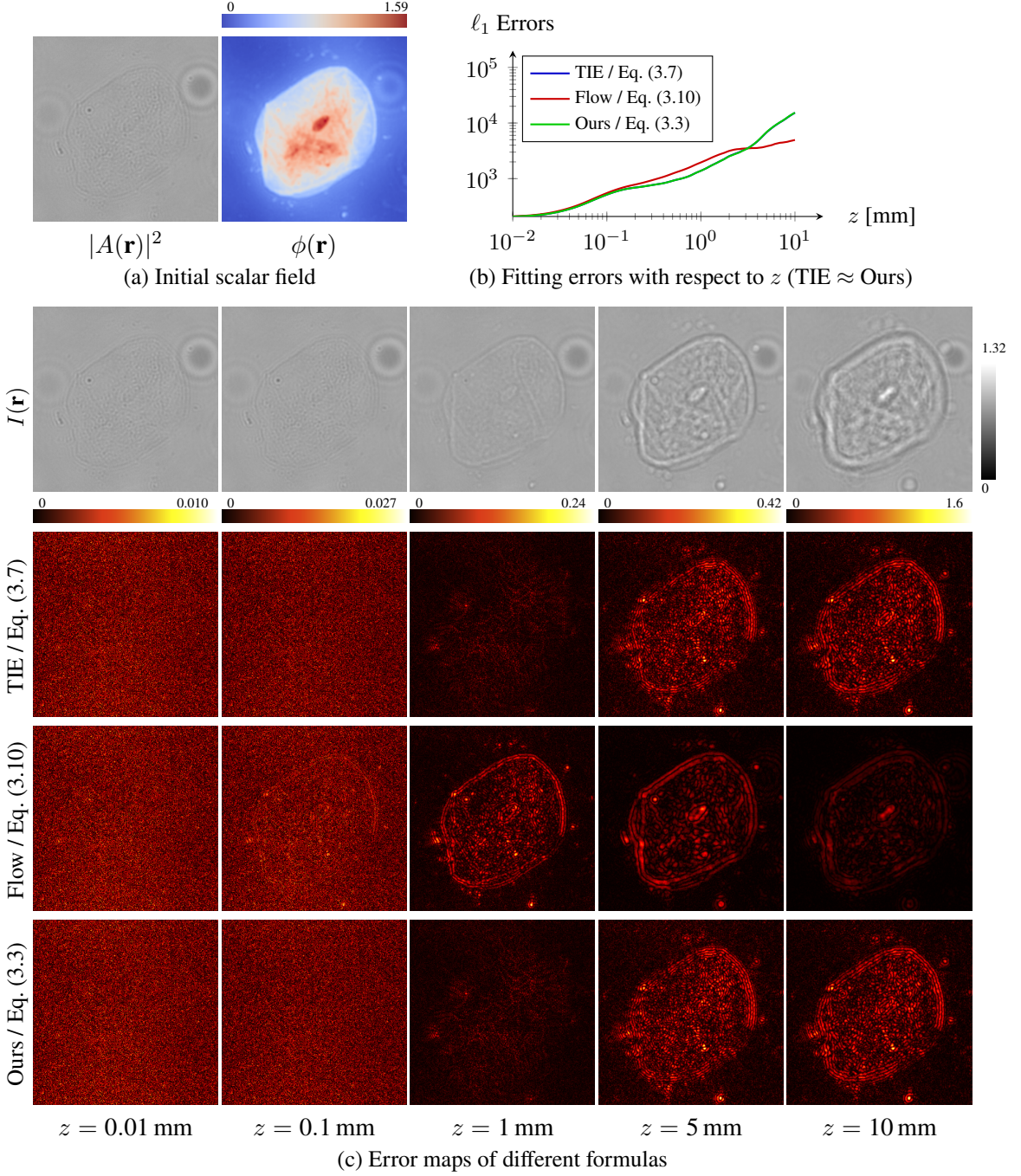


Figure 3.6: Errors of different formulas for a real-captured cheek cell wavefront propagating through z . For small wavefront slopes, the advantage of our formula Eq. (3.3) is not obvious compared to TIE, but still maintain its advantage comparing to flow-tracking formula Eq. (3.10). However, once the assumption $\nabla^2 d(\mathbf{r}) \ll 1/z$ is violated, both TIE and our formula amplify the defocusing error, showing $I(\mathbf{r})$ as a blurry image.

3.2.5 Discussion

The derived Eq. (3.3) in Section 3.2.1 fully characterizes deterministic image formation in classical wavefront sensors such as Shack-Hartmann and curvature sensors. Using its ray optics nature as constraints, achievable wavefront resolution follows Eq. (3.14) in Section 3.2.3, revealing a z - $|\rho|$ trade-off curve, offering a theoretical bound for future wavefront sensor designs. For slope tracking sensors, due to mm level distance z , wavefront resolution is fundamentally limited as in Figure 3.4, and hence we suggest classical slope tracking sensors be applicable to large-scale smooth aberrations, *e.g.*, large-scale adaptive optics [2] and autorefraction metrology [33]. If higher resolution is desired, possible workarounds are scanning optics [79, 35] for ptychography, combining spatial light modulators for computational sensing [80] beyond simple optics, or using numerical propagation based inversion [81, 82].

We may further extend Eq. (3.3) to include minor effects, *e.g.*, dark fields from indirect scattering. This will yield straightforward extension to existing scattering models in propagation-based wavefront sensing, for example the Fokker–Planck equation in paraxial X-ray imaging [83, 84]. Another direction is to impose stronger assumptions on samples, *e.g.*, weak phase that $\phi \ll 1$. We expect to achieve similar results of contrast [85] and mixed transfer function [86].

We may also take into account the higher-order infinitesimals in Appendix A.2 ignored when deriving Eq. (3.3). These higher orders are also related to the higher-order TIE formulation in [44]. These small amounts render the diffraction effects, could be helpful to forward modeling in freeform lens designs for caustic imaging [87, 68, 88] to reduce blurring artifacts.

3.3 Practice

Given the promising theoretical formulation Eq. (3.3), we prototype a masked sensor aiming to measure wavefronts. In this section, We focus on pure phase measurements.

3.3.1 Hardware prototype

We implemented a speckle-tracking wavefront sensor (the Coded Wavefront Sensor) [1] using a binary amplitude mask. The mask was placed $z \approx 1.5$ mm in front of a bare image sensor (PointGrey GS3-U3-15S5M-C, pixel size $\epsilon = 6.45 \mu\text{m}$). The binary mask is fabricated using photolithography in a chrome layer deposited on a 4" Fused Silica wafer, with a pixel pitch of $12.9 \mu\text{m}$. Example measurements are shown in Figure 3.7.

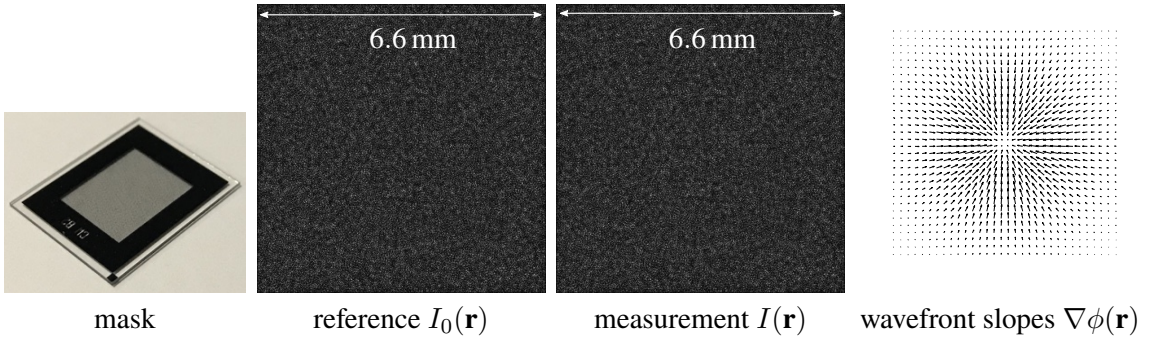


Figure 3.7: Prototype Coded Wavefront Sensor. A mask is placed in close proximity to an image sensor. Under collimated illumination, the mask produces a speckle pattern, which moves locally when spatial wavefront distortions present.

3.3.2 Decoding algorithm

Since we focus on wavefront measurements, we hence restrict the variables to be only the phase but not the radiance. Denoting the calibration (reference) image and the measurement image as $I_0(\mathbf{r})$ and $I(\mathbf{r})$, the measurement image $I(\mathbf{r})$ is shifted relative to $I_0(\mathbf{r})$ by a pointwise apparent motion proportional to the wavefront slope $\nabla\phi(\mathbf{r})$, as in Eq. (3.11):

$$I(\mathbf{r}) = I_0(\mathbf{r} - (z/k)\nabla\phi(\mathbf{r})). \quad (3.17)$$

Eq. (3.17) highlights the underlying principle of our Coded Wavefront Sensor: the distorted wavefront results in apparent motion of the diffraction pattern, assuming no scintillation. Note that the apparent motion is irrelevant to the wave number k if we consider the distorted wavefront $\phi(\mathbf{r}) = ko(\mathbf{r})$ with optical path $o(\mathbf{r})$, which means the Coded Wavefront Sensor allows for broadband illumination.

However, Eq. (3.17) is nonlinear. To retrieve $\phi(\mathbf{r})$ from $I_0(\mathbf{r})$ and $I(\mathbf{r})$, one may iteratively solve a linearized version of Eq. (3.17). At each step, the linearized version of Eq. (3.17) leads to the following formula, which is the basis for the so-called *optical flow* methods in computer vision [75]:

$$\frac{z}{k} \nabla \phi(\mathbf{r}) \cdot \nabla I_0(\mathbf{r}) + I(\mathbf{r}) - I_0(\mathbf{r}) = 0, \quad (3.18)$$

where \cdot denotes inner product. Note that the linearization is iteratively updated during the optimization, so that our model overall remains non-linear.

Denote image gradient fields as \mathbf{g}_x and \mathbf{g}_y along x and y directions, and \mathbf{g}_t as the difference between the two images, and finally define $\mathbf{G} = \begin{bmatrix} \text{diag}(\mathbf{g}_x) & \text{diag}(\mathbf{g}_y) \end{bmatrix}$ where $\text{diag}(\cdot)$ denotes a diagonal matrix formed by the corresponding vector. With these definitions, Eq. (3.18) is reduced to a least squares problem:

$$\underset{\phi_k}{\text{minimize}} \quad \|\mathbf{G}\nabla\phi_k + \mathbf{g}_t\|_2^2 + \beta \|\nabla\phi_k\|_2^2. \quad (3.19)$$

We solve this optimization problem with Neumann boundary conditions. To avoid boundary artifacts, we have introduced a spatial selection matrix \mathbf{M} to include the boundary values of ϕ_k as additional unknowns, to be determined by the optimization as that in [89].

This optimization problem bears a strong similarity to the classical Horn-Schunck optical flow problem [75]. However, in our case the flow vectors $\nabla\phi_k$ have a physical meaning as the gradients of the phase function ϕ_k , so we seek to directly solve for ϕ_k , instead of solving for the optical flow.

We solve this joint optimization problem by introducing a slack variable \mathbf{w} that physically represents the wavefront gradient $\nabla\phi_k$, and apply ADMM [57], yielding Algorithm 2. Here $\boldsymbol{\eta}$ is the dual variable, μ is a proximal parameter, \mathcal{F}_{DCT} and $\mathcal{F}_{\text{DCT}}^{-1}$ respectively denote forward and inverse Discrete Cosine Transforms (DCT). To suppress noise, median filtering is applied to the gradient estimation before a final integration to get the output wavefront solution ϕ_{estimate} , as suggested in [90].

Algorithm 2: ADMM linear solver for Eq. (3.19).

```

1 Initialize  $\phi^0$ ,  $\mathbf{w}^0$  and  $\boldsymbol{\eta}^0$  from previous frame, set  $\mu > 0$ 
2 while not converge do
3    $\phi^{k+1} \leftarrow \frac{\mu}{\beta+\mu} \mathcal{F}_{\text{DCT}}^{-1} (\mathcal{F}_{\text{DCT}}(\nabla^T(\mathbf{w}^k - \boldsymbol{\eta}^k)) / \mathcal{F}_{\text{DCT}}(\nabla^2))$ 
4    $\mathbf{w}^{k+1} \leftarrow (\mu\mathbf{I} + \mathbf{M}^T \mathbf{G}^T \mathbf{G} \mathbf{M})^{-1} (\mu(\nabla\phi^{k+1} + \boldsymbol{\eta}^k) - \mathbf{M}^T \mathbf{G}^T \mathbf{g}_t)$ 
5    $\boldsymbol{\eta}^{k+1} \leftarrow \boldsymbol{\eta}^k + \nabla\phi^{k+1} - \mathbf{w}^{k+1}$ 
6 end
7  $\hat{\mathbf{w}} = \text{median filter}(\mathbf{w}^k - \boldsymbol{\eta}^k)$ 
8 return  $\phi_{\text{estimate}} = \frac{\mu}{\beta+\mu} \mathcal{F}_{\text{DCT}}^{-1} (\mathcal{F}_{\text{DCT}}(\nabla^T \hat{\mathbf{w}}) / \mathcal{F}_{\text{DCT}}(\nabla^2))$ 

```

3.3.3 Simulation

We have conducted two simulations to investigate the sensitivity and accuracy of the Coded Wavefront Sensor. In the simulations, the illumination is monochromatic ($\lambda = 550$ nm). The overall aperture size equals 6.6 mm \times 6.6 mm with sensor and mask pixel pitch 6.45 μm and 12.9 μm , respectively. The scalar field of interest is sampled at 1.29 μm . Gaussian noise is added and the image Signal-to-Noise Ratio (SNR) equals 40 dB. The wave propagation is simulated using the angular spectrum method [76] with filtering [77] to suppress high frequency artifacts.

The first numerical experiment evaluates the dynamic range of our sensor. A planar wave (*i.e.* the reference), and sixteen different scales of spherical waves are simulated at the mask plane, respectively, for five different distances z . The reference image, and sixteen measurement images are consequently recorded at the sensor plane. Figure 3.8 shows the wavefront reconstruction error (in terms of Root Mean Square (RMS)) our sensor can attain,

providing the fixed curvature wavefronts that progressively violate Eq. (3.17). With the increase of wavefront range, the decrease of accuracy can be partially explained by the approximations made to derive Eq. (3.3).

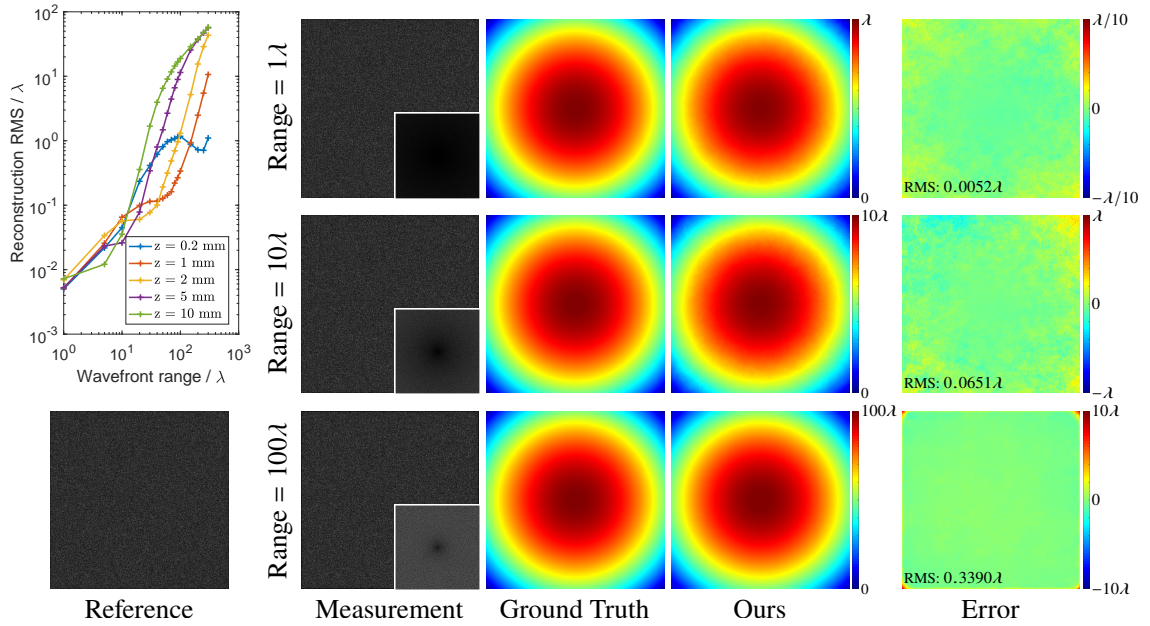


Figure 3.8: Accuracy experiments. Top left shows the reconstruction error in RMS for different wavefront range (Peak-to-Valley) for different z . Specifically, results of three wavefront range spherical waves are shown when $z = 1 \text{ mm}$. To visualize the difference between the measurement and the reference, the logarithm of their subtraction are shown as inset.

Figure 3.9 shows the second numerical experiment, where we evaluate the performance of our sensor by sensing typical atmospheric turbulence. The same turbulence is evaluated at different scales. The synthetic atmospheric turbulence respects the Kolmogorov's theory, and is implemented using the sub-harmonic method [91]. The outer scale and inner scale of the base turbulence are set to be 4 m and 1 mm respectively. The mask-to-sensor distance $z = 1.5 \text{ mm}$. The result indicates the possibility to apply our sensor for atmospheric turbulence measurement.

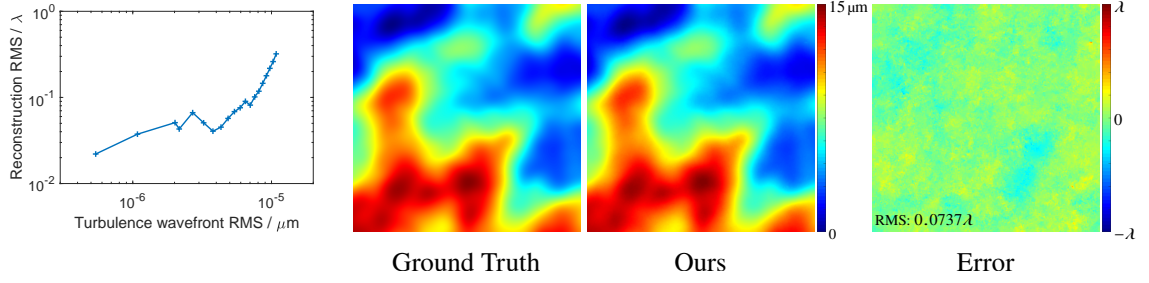


Figure 3.9: Synthetic atmospheric turbulence. Most left shows the reconstruction RMS versus the turbulence RMS. Specifically, one scale of the turbulence is shown on the right.

3.3.4 Realistic wavefront sensing

Finally, we show visualization of two realistic wavefronts, the ones created by heat flow and defocusing, using the Coded Wavefront Sensor. The heat flow is generated using a lighter, and defocus is achieved by manually moving a convex lens back and forth. To increase the field-of-view for better visualization, we employed a telescope system for wavefront magnification, with a ratio of two. All the measurement images were captured and the wavefronts were reconstructed on a GPU in real-time. Here, two frames are chosen to be shown in Figure 3.10, with their reconstructed wavefronts in interference fringes , respectively.

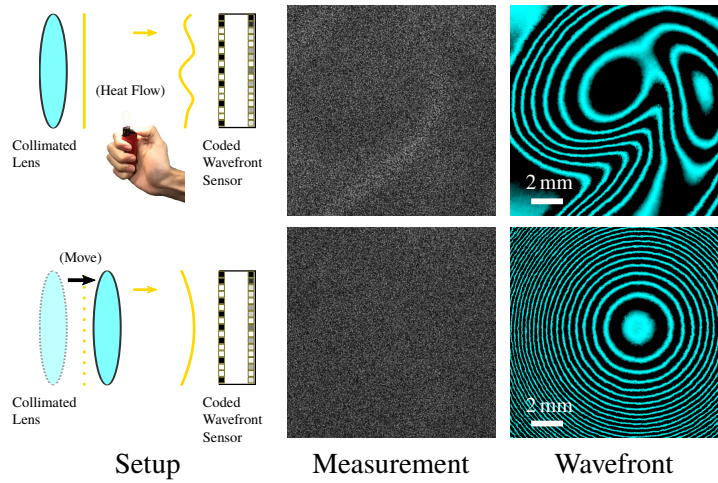


Figure 3.10: Wavefront visualization of the heat flow and the defocusing. The setup diagrams are simplified versions of the real situations.

3.3.5 Discussion

The Coded Wavefront Sensor is related to a number of other imaging systems and designs. Just like the Shack-Hartmann sensor can be interpreted as a combination of a lenslet-based light field camera [51] and 2D spot tracking software, our sensor can be seen as a combination of a mask-based light field camera [52, 54] with a more sophisticated dense 2D motion tracking method. The Coded Wavefront Sensor also bears similarity to BOS imaging [12], but with the patterned “background” moved into the camera for a compact form factor.

The design of the Coded Wavefront Sensor allows it to be used as a drop-in replacement for any optical system currently using a Shack-Hartmann sensor, with an immediate gain in spatial resolution. In addition, we believe it can also be incorporated into optical systems configured for phase retrieval problems, including in microscopy. Since there is no need for phase diversity and coherent illumination, such an adaptation should in fact be easier than many existing phase retrieval setups. We will explore these applications in Chapter 5. A similar commercial technique is the PHASICS wavefront sensor, which uses a sinusoidal grating to encode the optical fields. Compared to PHASICS, in hardware, our technique here does not require special gratings, and a random amplitude grating would be sufficient, and no careful calibration and alignment is needed. In software, our algorithm resolves phase directly, and no phase unwrapping is required.

Several other extensions in both applications and usage are also conceivable in the future. The calibration or reference image does not always need to correspond to plane wave illumination, but could be a pre-distorted wavefront. For example when characterizing freeform lenses, a known ground-truth lens can be used to form the reference image, and the Coded Wavefront Sensor can then be used to characterize the difference between the reference lens and another lens.

For the accuracy of the Coded Wavefront Sensors it is necessary that the mask produces a locally distinctive diffraction pattern on the image sensor. To facilitate this process, the mask could be custom-designed (instead of random) to produce a specific diffraction pattern

such as wavelet noise [92]. It should also be possible to use grayscale masks or even random phase gratings as an alternative to the binary masks employed in this work.

3.4 Conclusion

We derive a new image formation model Eq. (3.3) for general classical wavefront sensors consist of a simple coding optics and an image sensor as in Figure 3.1. This new model generalizes TIE to far distance regions beyond the finite difference approximation as shown in Section 3.2.2, verified by simulations in Section 3.2.4. The validity of this model depends on propagation distance z , which in turn defines achievable spatial wavefront resolution as analyzed in Section 3.2.3. We believe this more general model could be useful in propagation-based deterministic wavefront sensing applications, for those TIE is replaceable by Eq. (3.3).

We also introduce a new type of wavefront sensor called the Coded Wavefront Sensor, a novel sensor design that is physically implemented by a single binary masked sensor to encode the incoming wavefront, and is numerically implemented by an efficient optimization decoding algorithm, such that wavefront reconstruction with high spatio-temporal resolution is achieved within sub-wavelength accuracy. The theoretical principle behind Coded Wavefront Sensors offers a new approach to the wavefront sensing problem, namely the direct 2D tracking of diffraction patterns.

Chapter 4

Application: Megapixel Adaptive Optics

In the previous chapter, we have demonstrated the basic principle of general wavefront sensing, and practical usage of our proposed sensor. In this chapter, we show megapixel adaptive optics, one of the applications that leverages the advantage of the proposed technique.

Adaptive Optics (AO) has become a valuable tool for correcting minor optical aberrations in applications such as astronomy and microscopy. However, due to the limited resolution of both the wavefront sensing and the wavefront correction hardware, it has so far not been feasible to use AO for correcting large-scale waveform deformations that occur naturally in regular photography and other imaging applications.

In this work, we demonstrate an adaptive optics system for regular cameras. We achieve a significant improvement in focus for large wavefront distortions by improving upon a recently developed high resolution coded wavefront sensor, and combining it with a spatial phase modulator to create a megapixel adaptive optics system with unprecedented capability to sense and correct large distortions.

4.1 Introduction

Adaptive Optics (AO) systems are highly effective in correcting dynamic aberrations in applications such as astronomy and microscopy [93, 94]. In these settings, the aberrations are typically small (*e.g.*, atmospheric distortions in the case of telescopes), albeit significant in the case of otherwise diffraction limited optics.

Adaptive optics systems are comprised of two major components: a wavefront sensor,

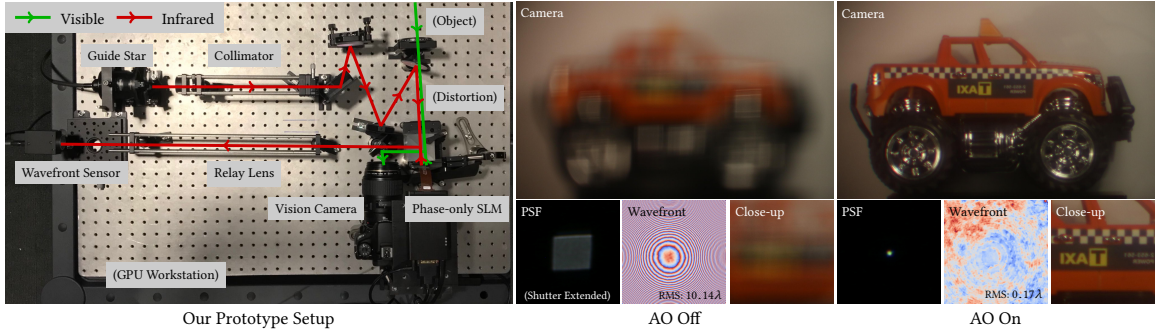


Figure 4.1: We propose a high resolution AO technique to correct for large distortions in photography and vision applications. AO relies on the combination of a wavefront sensor and a phase modulator to measure and optically correct for incoming phase distortions. Based on a previously proposed high resolution wavefront sensor, our proposed AO prototype achieves unprecedented AO sensing and correcting simultaneous high spatial resolution for large phase distortions. An example for vision deblurring is shown on the right where a defocus distortion is being well compensated.

Table 4.1: Performance characteristics of different wavefront sensing technologies.

	Resolution	Dynamic Range	Frame Rate	Pixel Usage	Calibration	Requires Coherent Light?	Light Efficiency
Shack-Hartmann sensor [16]	Low/High	Large/Small	High	Low	Easy	No	High
Curvature sensor [22]	High	Large	High	High	Hard	Yes	High
Pyramid wavefront sensor [18]	Medium	Medium	High	Medium	Medium	No	Low
Interferometry sensor	High	Small	High	High	Medium	Yes	High
Multi-lateral shearing interferometer [43]	Medium	Medium	High	High	Easy	No	Medium
Coded Wavefront Sensor [1]	High	Large	Medium [†]	High	Easy	No	High [‡]

[†]Computationally bounded and inversely proportional to wavefront resolution.

[‡]Depends on the modulation mask. For phase mask modulation the light efficiency is almost 100 %.

which measures the shape of the wavefront of light across the aperture of the optical system, and a phase modulator, which corrects the distorted wavefront to make it planar. In traditional AO systems, the wavefront sensor is usually a Shack-Hartmann [16] or pyramid sensor [18], while the phase modulation is achieved by tilting mirrors [95, 96] or deforming a reflective membrane with pistons [97]. Both the sensing and the modulation components in these systems suffer from low *spatial resolution* (e.g., at most hundreds to thousands of measurement points and actuators) as well as small *range* that limits the amplitude of the distortion. As a result, most AO systems can only correct for distortions corresponding to a few low-order Zernike polynomials and low amplitudes. Multi-conjugate AO systems [98, 99] are one possible solution to offer high resolution and large compensation amplitudes, but at the cost of additional wavefront sensors and correctors that have to be carefully aligned and calibrated to one another. This significantly increases the cost and overall system complexity compared to the single sensor / single corrector systems that we consider in our

work.

In photography and most computer vision applications, the situation is different: normal camera optics are usually not diffraction limited, and less sensitive to small distortions. However, large distortions may occur regularly. Consider, for example, the case of a computer vision system of a self-driving car operating under rainy conditions. The camera of this vision system may have to re-focus through a dynamically changing water surface, as rain flows across the cover surface of the optical system. Current AO systems cannot deal with such large wavefront distortions.

To mitigate this situation, we propose a new AO setup, which is built around an improved version of the recently introduced coded wavefront sensor [1], and an Liquid Crystal on Silicon (LCoS) spatial phase modulator (phase SLM). Both components have megapixel resolution, which allows us to detect and correct for wavefront distortions with complex shapes. Moreover, both the sensor and the modulator can also deal with distortions of significantly larger amplitude, so that much more severe defocus effects can be corrected. In particular, we can achieve Strehl ratios close to 1 even for large-scale deformation near the optical axis, although the off-axis performance is reduced.

Specifically, our technical contributions are:

- An adaptive optics system design that is capable of sensing and correcting large wavefront distortions with megapixel wavefront sensing and phase modulation.
- An improved version of the coded wavefront sensor [1] with better light efficiency and improved algorithms.

Although this initial prototype system is limited in frame rate and light efficiency (see Section 3.4 for a full discussion), we believe this work is a major step towards utilizing adaptive optics in regular cameras for both photography and machine vision applications.

4.2 Related work

The purpose of adaptive optics systems is to re-focus optical systems through (often time-varying) distortions. In the following we provide a brief review of existing means to measure and correct defocus.

4.2.1 Coded apertures and image deblurring

Coded apertures and image deblurring have been widely researched in the computational photography community. Researchers have delved into coded apertures for defocus blurring compensations in extended-depth-of-field applications [100, 101, 102, 103, 104], or in motion blur removal [105, 106]. Approaches on pure software deconvolution have also been proposed, for example non-blind deconvolution algorithms [107, 108, 109] given the blurring kernel, or the more challenging blind deconvolution case where algorithms design specifically for motion blurring [110, 111, 112], or with utilization of natural priors [113, 114, 115, 116]. These techniques either rely on specific assumptions on the scene and blurring kernels, or consume heavy computations, thus not applicable to general distortions for real time applications. Moreover, purely software-based solutions cannot deal with large aberrations as we demonstrate in Section 4.5.

4.2.2 Coded wavefront sensors

Coded wavefront sensors replace the microlens array of the Shack-Hartmann designs with a binary amplitude mask in close proximity to a bare image sensor [1], and are thus related to mask-based light field cameras, as discussed above. In the Coded Wavefront Sensor, the slope of the wavefront is tracked using numerical methods related to optical flow [1], and as such they combine a full spatial resolution with the ability to measure large distortions. Other works with similar ideas have been presented, for example using a diffuser for visible light [30], or high frequency phase objects for X-ray [27, 28]. In this work, we improve

the coded wavefront sensor both by introducing a phase mask instead of an amplitude mask (thereby improving light sensitivity by a factor of 2), and by improving the software algorithms for tracking the slope of the wavefront. This has been introduced in Chapter 3.

4.2.3 Adaptive optics

Adaptive optics (AO) techniques were originally developed for military and astronomical telescopes to sharpen stellar observations by measuring and compensating atmospheric turbulence. Since then, AO has found its other applications in ophthalmology [117, 118, 119], microscopy [120, 121], and optical coherent tomography [122, 123]. Classical AO systems employ a Shack-Hartmann wavefront sensor to observe the wavefront of a single point-shaped source, also known as the *guide star*. Any measured atmospheric distortion equally affects the full field of view of the main camera that observes the object of interest. However, this distortion can be corrected using a deformable mirror. In *open loop* systems, only the view of the main camera is corrected, while in *closed loop* systems the wavefront sensor also images the guide star through the deformable mirror, so that in each time step only a smaller differential deformation needs to be measured.

Due to the low resolution nature of deformable mirrors, spatial light modulators have been utilized to improve correction resolution, *e.g.*, [124, 125, 126, 127]. However, existing AO systems have not been able to demonstrate the combination of high spatial resolution and the ability to measure and correct for large distortions, which is required in many photography and computer vision applications.

The need for a guide star is a potential impediment for the use of AO approaches in regular imaging. Possible solutions include a laser-generated dot, or special application-specific setups. For example, in the above-mentioned example of a car vision system, the camera could be behind the windshield, and the guide star could be integrated in the hood of the car to compensate for distortions caused by raindrops on the wind shield.

To our knowledge, this work is the first AO system that uses a phase-only SLM and

a correspondingly high resolution wavefront sensor, to optically sharpen heavily blurred vision images.

4.3 Megapixel adaptive optics

Our AO system makes innovations on both the hardware and the software aspects. Figure 4.2(a) shows a diagram of the hardware setup. A Coded Wavefront Sensor observes an infrared guide star through the same optical system and distortions through which a regular machine vision camera observes a visible light scene. Dichroic mirrors are used to separate the IR and visible light paths while maximizing light efficiency. A phase-only SLM is used to correct for distortions. We utilize a closed loop design, *i.e.*, the SLM is in the optical path of both the camera and the wavefront sensor.

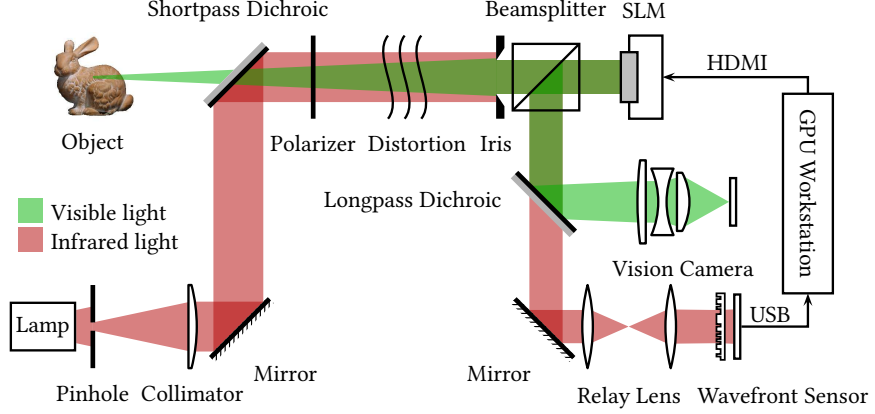
In the following, we first discuss the software aspects of our system, before returning to the hardware prototype in Section 4.4.

4.3.1 Closed loop adaptive optics

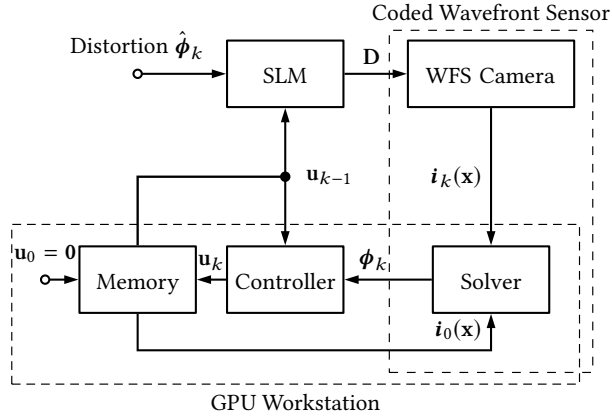
The software part of the system is the closed control loop for the adaptive optics system, which consists of a wavefront sensing component and an update pattern for the phase SLM. Figure 4.2(b) depicts a control block diagram for the closed loop system. At time step k , we denote the distorted wavefront from the guide star as $\hat{\phi}_k$. This wavefront is partially corrected by the correction phase \mathbf{u}_{k-1} computed for the phase SLM in the previous time step, resulting in a raw sensor image i_k being observed by the wavefront sensor. From this image, the Coded Wavefront Sensor measures an estimate of the residual distortion:

$$\phi_k = \hat{\phi}_k - \mathbf{D}\mathbf{u}_{k-1}, \quad (4.1)$$

where \mathbf{D} is a geometric alignment transformation that needs to be calibrated. If SLM and wavefront sensor are perfectly aligned, then \mathbf{D} is the identity. In the first iteration, the SLM



(a) High resolution AO setup for vision deblurring



(b) Closed loop AO control diagram

Figure 4.2: (a) Hardware overview. A shortpass dichroic mirror reflects the infrared (IR) light from the guide star, while transmitting the visible light from the object, merging the two into a single beam that undergoes a distortion before entering the AO system. Inside the AO system, a linear polarizer ensures the SLM operates in phase modulation mode. After being modulated by a phase-only SLM, the joint light cone is split back into IR and visible components, with the visible light being directed to the camera, while the IR light is directed to the wavefront sensor. The dichroic mirrors have the same cutoff wavelength so that the visible and IR light paths do not interfere with each other. Relay lenses ensure the SLM and the Coded Wavefront Sensor are in conjugate. For easy visualization only the IR light is drawn for the broadband white lamp. (b) At k^{th} AO iteration, the GPU workstation takes in the captured image i_k from the wavefront sensor, computes the reconstructed phase y_k , and renders the SLM with a new correction phase \mathbf{u}_k .

is initialized with a flat phase, *i.e.*, $\mathbf{u}_0 = \mathbf{0}$.

One goal in closed loop AO is to stabilize the loop, *i.e.*, to design a control strategy to update \mathbf{u}_k such that $\|\phi_k\|_2 \rightarrow 0$ with $k \rightarrow \infty$. For sufficiently fast-response AO systems, or slowly time-varying distortion wavefronts, stabilization can be achieved using a digital

integrator as a controller:

$$\mathbf{u}_k = \mathbf{u}_{k-1} + \alpha \mathbf{D}^{-1} \phi_k, \quad (4.2)$$

where α is a loop gain parameter. Ideally for $\alpha = 1$ the loop converges in one iteration and $\mathbf{u}_k = \mathbf{D}^{-1} \hat{\phi}_k$.

4.3.2 Wavefront solver

We now review the Coded Wavefront Sensor and its associated numerical solver for computing the observed wavefront ϕ_k from a captured image i_k , at the k^{th} AO iteration.

Sensing model

Figure 4.3 depicts the working principle, which is briefly reviewed in the following. The Coded Wavefront Sensor consists of a bare image sensor with a diffraction mask placed in closed proximity. The original Coded Wavefront Sensor [1], used a binary amplitude mask, which absorbs 50% of the incident light, while we utilize a binary phase mask, where the absorption is negligible. Irrespective of the type of mask used, an incident plane wave creates a characteristic diffraction pattern on the image sensor, which is measured and saved as image $i_0(\mathbf{r})$, $\mathbf{r} = (x, y)^T$ in a calibration phase.

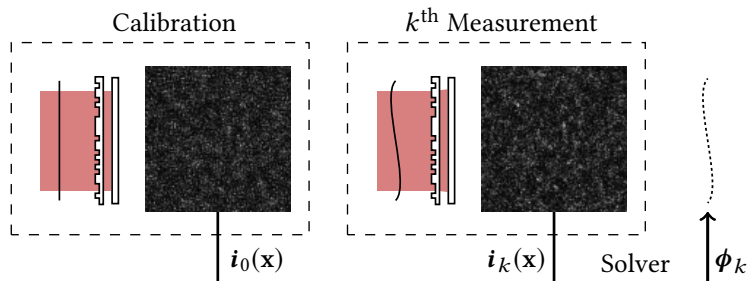


Figure 4.3: Principle of the Coded Wavefront Sensor.

Wang *et al.* [1] were able to show that, if a distorted wavefront ϕ_k is incident on the same configuration, it results in an image i_k that is a locally warped version of i_0 according

to the following relationship:

$$\mathbf{i}_k(\mathbf{r}) \approx \mathbf{i}_0 \left(\mathbf{r} - \frac{\lambda z}{2\pi} \nabla \phi_k \right), \quad (4.3)$$

where z is the spacing between the mask and the image sensor, and λ is the wavelength of light. That is, the local shift of the pattern is proportional to the gradient of the wavefront. Intuitively, since the pattern has a high spatial frequency content, the 2D distortion can be tracked with optical flow-style methods, and the shape of the wavefront ϕ_k can be recovered from the pair of images $\mathbf{i}_0, \mathbf{i}_k$.

We note that, although Eq. (4.3) contains the wavelength λ , this principle actually does not assume coherent light and works well for broadband illumination.

Optimization

To simplify the notation, we will in the following absorb the constant $\lambda z / 2\pi$ into the ϕ_k variable. The process of recovering ϕ_k can be expressed as a least-squares optimization problem with an additional smoothness regularizer:

$$\underset{\phi_k}{\text{minimize}} \quad \|\mathbf{i}_k(\mathbf{r}) - \mathbf{i}_0(\mathbf{r} - \nabla \phi_k)\|_2^2 + \beta \|\nabla \phi_k\|_2^2, \quad (4.4)$$

where $\beta > 0$ is a weighting factor.

To solve this problem, we take inspiration from the optical flow literature [75, 128], and linearize $\mathbf{i}_0(\mathbf{r} - \nabla \phi_k)$ around \mathbf{r} in Eq. (4.3). This yields the following approximation:

$$\nabla \mathbf{i}_0(\mathbf{r}) \cdot \nabla \phi_k + \mathbf{i}_k(\mathbf{r}) - \mathbf{i}_0(\mathbf{r}) \approx 0, \quad (4.5)$$

where \cdot denotes the inner product. This discretized version optimization has been formulated as Eq. (3.19) in Chapter 3, and solved using Algorithm 2.

The superiority of our ADMM solver over the usual conjugate gradient method is illus-

trated in Figure 4.4, where a 10λ Gaussian wavefront is simulated. The conjugate gradient method is initialized with a rough wavefront estimation ϕ^0 , which is the Poisson integration from a one-step flow estimation $\nabla\phi_k$ in Eq. (3.19). Our ADMM solver converges efficiently with low error, whereas the conjugate gradient method requires a large number of iterations. In real experiments, the ADMM solver only runs for 10 iterations, which provides a good compromise between accuracy and speed.

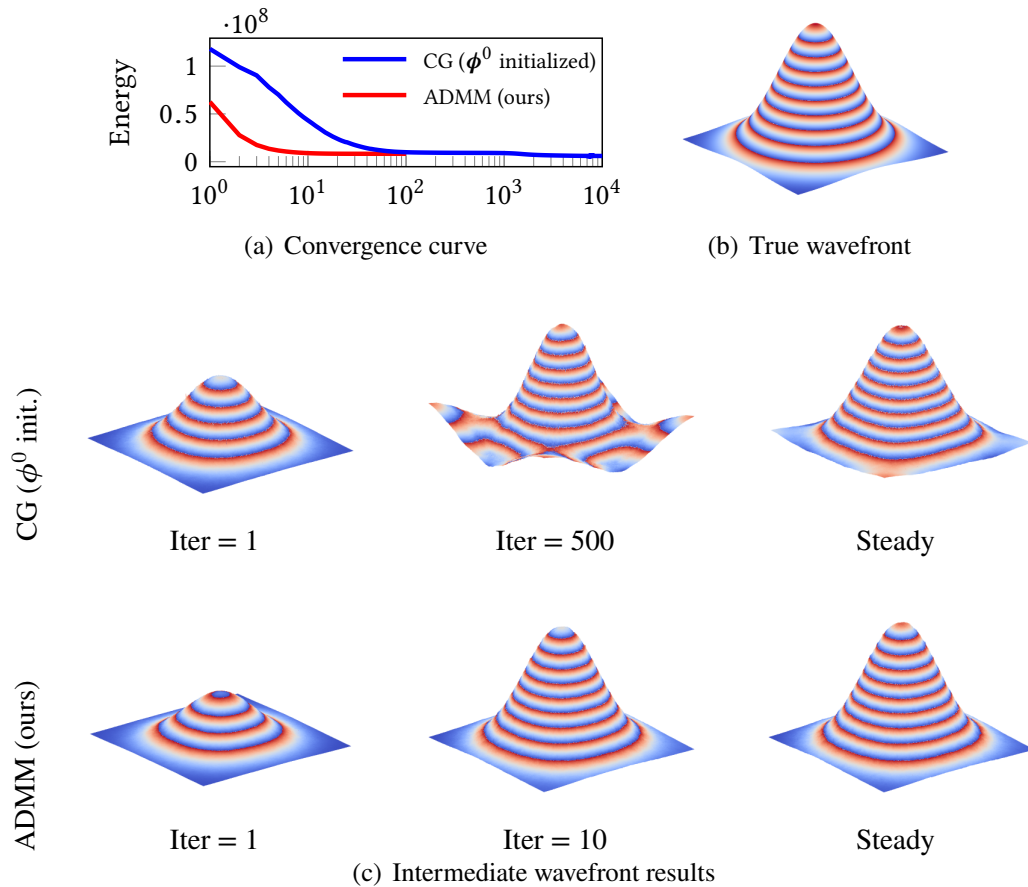


Figure 4.4: Our ADMM solver efficiently converges to the minimum with a good visual plausibility, whereas conjugate gradient method takes much more iterations even when the energy decreasing is barely perceptible.

Nonlinear warping scheme

This linear solver can be improved by including non-linear warping [128]. We first use a linear approximation according to Eq. (4.5) to obtain a preliminary wavefront estimation, then warp the reference image $i_0(\mathbf{r})$ towards the gradients of the preliminary estimation, and then re-linearize the system to obtain an improved estimate in the next round.

Algorithm 3 shows this non-linear variant of Algorithm 2. This scheme contains a coarse-to-fine strategy and an in-level nonlinear warping at each pyramid level. The pyramid level s increases from 0 to a given pyramid level number, namely from the smallest down-sampled image size to the original size. At each warping step j , the pyramid level image $i_0^s(\mathbf{r})$ is warped to a new image $i_0^s(\mathbf{r} - \nabla\phi^j)$ according to current wavefront estimation ϕ^j , then the linearized problem Eq. (3.19) is solved with the new gradient estimations \mathbf{g}_x^s , \mathbf{g}_y^s and \mathbf{g}_t^s . The unknown wavefront ϕ_k is iteratively updated in this way until convergence.

The improvement of the warping strategy is illustrated in Figure 4.5, where a turbulence phase screen is simulated using the sub-harmonic method [91]. Algorithms 3 and 2 (with and without warping, respectively) are compared for different pyramid levels. The warping strategy greatly improves large wavefront sensing to a fine accuracy.

Algorithm 3: A warping scheme for Algorithm 2.

```

1 Initialize  $\phi^0$  with zeros
2 for pyramid level  $s$  do
3    $i_0^s(\mathbf{r}) \leftarrow i_0(\mathbf{r}) \downarrow$  //  $\downarrow$ : Down-sampling
4    $i_k^s(\mathbf{r}) \leftarrow i_k(\mathbf{r}) \downarrow$ 
5   while  $\|\Delta\phi^j\|_2^2 > \epsilon$  do // In-level warping,  $\phi^j \leftarrow \phi^s$ 
6     Compute  $\mathbf{g}_x^s, \mathbf{g}_y^s, \mathbf{g}_t^s$  from  $i_0^s(\mathbf{r} - \nabla\phi^j)$  and  $i_k^s(\mathbf{r})$ 
7      $\Delta\phi^j \leftarrow \text{Reconstruct Wavefront}(\mathbf{g}_x^s, \mathbf{g}_y^s, \mathbf{g}_t^s)$  // Algorithm 2
8      $\phi^{j+1} \leftarrow \phi^j + \Delta\phi^j$ 
9   end //  $\phi^s \leftarrow \phi^j$ 
10  if  $s$  is not the final level then
11    |  $\phi^{s+1} \leftarrow \phi^s \uparrow$  //  $\uparrow$ : Up-sampling
12  end
13 end

```

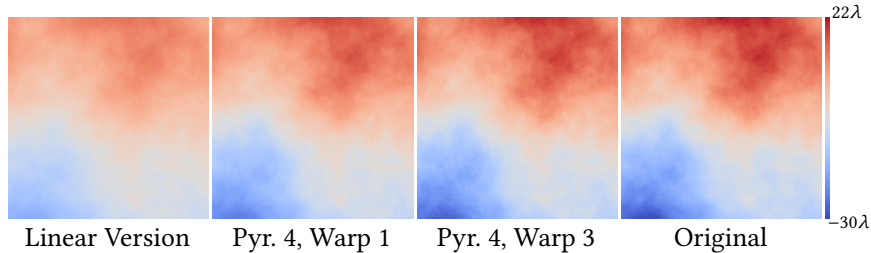


Figure 4.5: For large phase distortions, the proposed warping scheme wavefront solver enables an improved estimation accuracy. Simulated wavelength $\lambda = 550\text{ nm}$.

4.4 Prototype

In the following, we describe our prototype in terms of both hardware components and software implementation details.

4.4.1 Hardware

Mask fabrication and assembly

In our experiments, the Coded Wavefront Sensor is built around a monochromatic $2/3''$ Charge-Coupled Device (CCD) camera (PointGrey GS3-U3-15S5M-C), with a sensor resolution of 1384×1032 and a pixel pitch of $6.45\text{ }\mu\text{m}$. This camera was operated without a lens, and the IR filter was removed. Instead, the mask was mounted onto the sensor at a distance of approximately 1.5 mm from the light sensitive surface.

The binary phase mask itself is a random, binary height field fabricated on a 0.5 mm thick $4''$ fused silica wafer via photolithography followed by Reactive Ion Etching. Each mask pixel is $12.9\text{ }\mu\text{m} \times 12.9\text{ }\mu\text{m}$, and the etching depth is chosen such that the corresponding phase delay of the pixels is either 0 or π . The dimension of the mask is adjusted to 20 mm \times 17 mm to match the cover glass on the sensor. A profile of the fabricated binary phase mask is measured on Zygo NewView 7300 in Figure 4.6.

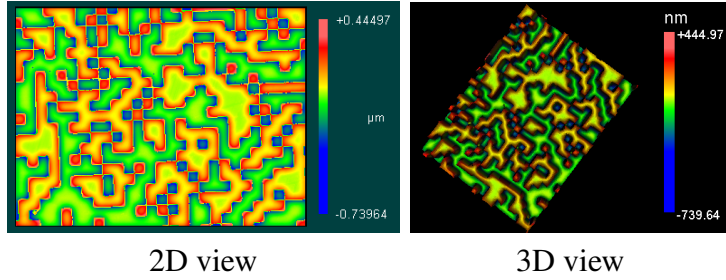


Figure 4.6: 2D and 3D profile of the central area on the fabricated binary phase mask taken with Zygo NewView 7300.

Optical setup

Figure 4.7 shows the experimental setup. Our prototype employs largely off-the-shelf optical and mechanical components from Thorlabs, with a few customized 3D-printed components. We use a HOLOEYE PLUTO phase-only SLM (PLUTO-2-VIS-014), with a pixel pitch of $8.0\text{ }\mu\text{m}$ and a maximum 3π phase retardation for wavelength $\lambda = 532.8\text{ nm}$, and the refresh rate is 60 Hz (same as V-Sync). The frame rate of the wavefront sensor is set to be its maximum of 45 Hz, with streaming mode enabled. To match sizes between SLM and the wavefront sensor, a relay lens system scales down the SLM plane by a factor of 4/3 onto the wavefront sensor plane. Due to the limited wavefront sensor size, not all SLM pixels are covered (see also Figure 4.10), so a 3D-printed square aperture is designed to prevent extra light from impinging onto the unobservable areas of the SLM. Black flocked paper is used for blocking stray light. All lenses are achromatic doublets.

To prevent the guide star from being seen by the vision camera, the two dichroic mirrors have been selected to operate at the same cutoff wavelength of 650 nm. However in practice, it is still needed to have a longpass filter in front of the broadband white light to further suppress the visible spectrum from the lamp. Figure 4.8 illustrates the effect. The USB output of the PointGrey sensor and the HDMI input for the phase-only SLM, are both connected to a host workstation running Ubuntu 16.04.3 LTS, with a NVIDIA GTX Titan X (Pascal) graphics card, 2.70 GHz Intel Xeon E5-2680 processors ($\times 32$) and 64 GB RAM.

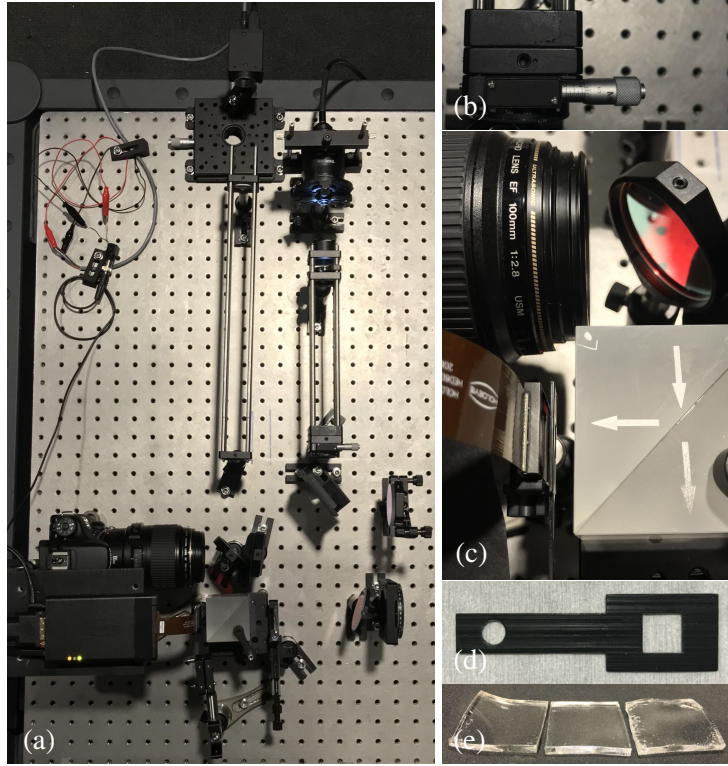


Figure 4.7: Our high resolution AO prototype setup. (a) shows the setup overview. Closeup (b) and (c) respectively shows how we obtain collimated, polarized infrared light, and how iris (d) is attached close to the SLM. Some distortion candidates are in (e). Note the phase-only SLM and wavefront sensor are mirror dual to each other.

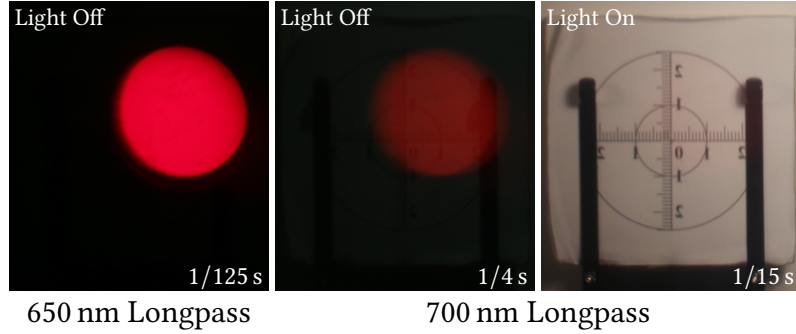


Figure 4.8: Adding a longpass filter in front of the guide star to suppress it from being visible to the vision camera.

4.4.2 Software

All control code and processing algorithms are implemented using C++ and CUDA. To avoid unnecessary CPU-GPU data transfer, the output phase image is rendered directly to the SLM through CUDA-OpenGL interoperability. All textures are operated with replicate

boundary conditions. To synchronize the camera and SLM so the camera shutter will not start to integrate when the SLM is updating, we use the workstation output V-sync signal (60 Hz) as a hardware trigger. For maximum speed, all unknown sizes are set to be power of two (*e.g.*, 1024, 512, \dots) to make use of the radix-2 Fast Fourier Transforms (FFT) algorithm.

Interpolation

Interpolations are needed when doing warps. Empirically for best performance, we use cubic spline interpolation for in-level warping, and bilinear interpolation (with anti-aliasing pre-filtering) for pyramid-level warping. To avoid expensive linear system solvers for cubic coefficient calculations each time, all image warping operations are performed on the reference image $i_0(\mathbf{r})$. For optimum performance, before running the GPU solver Algorithm 3 online, the reference image $i_0(\mathbf{r})$ is first decomposed in-place with its cubic coefficients, thus the subsequent online warping operations become trivially fast convolutions.

Denoising

To reduce wavefront sensing noise and the unavoidable phase wrapping artifacts produced by the phase-only SLM, bilateral filtering is applied to both the reconstructed wavefront ϕ_k before updating \mathbf{u}_k , and the accumulated phase image \mathbf{u}_k before final rendering onto the SLM. Figure 4.9 shows an experimentally obtained performance comparison between an original and a denoised version, where the latter one produces smoother phase profile with more continuous wrapping rings, and stably converges to a much smaller residual in terms of wavefront RMS.

Calibration

AO systems are designed to detect and correct for very small wavefront distortions, and as such they are extremely sensitive to misalignment and mis-calibration. For a successful

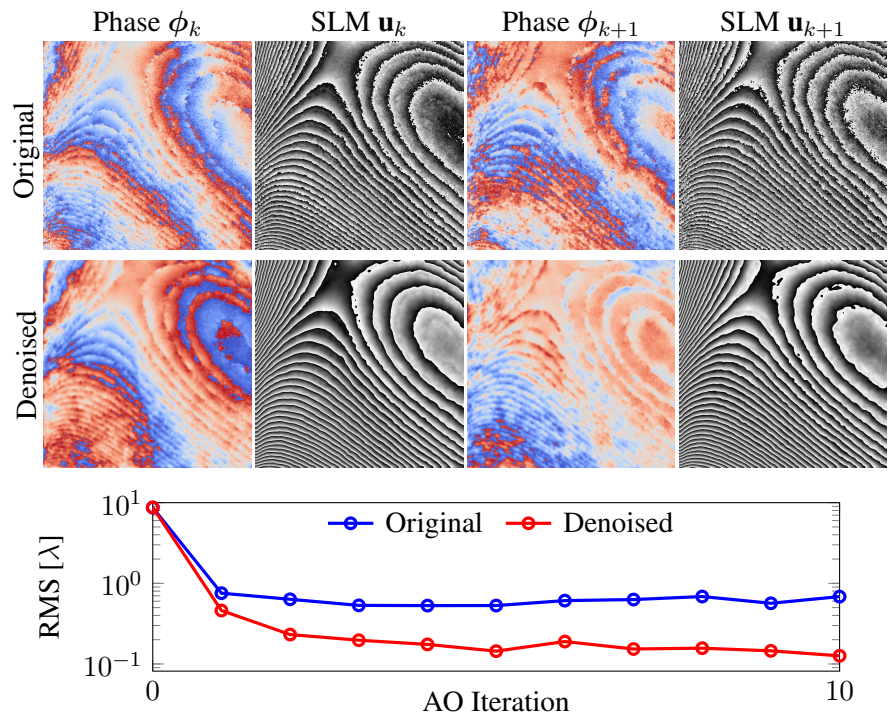


Figure 4.9: Bilateral filtering of detected wavefront ϕ_k and the accumulated SLM phase u_k . Smoother phase reduces undesired higher-order SLM diffraction and hence stabilizing the closed loop. Bilateral filter spatial and intensity window sizes are both 15×15 . Phases are visualized by 2π wrapping.

AO system, one has to perform careful calibration to ensure the wavefront sensor and the corrector are in good alignment. To measure the wanted inverse alignment transform \mathbf{D}^{-1} in Eq. (4.2), a microlens array phase image is shown on the SLM, and is then measured by the Coded Wavefront Sensor. By comparing the original and detected center points, assuming a 2D homography, \mathbf{D}^{-1} can be fitted by an over-determined system. Figure 4.10 depicts this calibration pipeline, as an improved variant to that in [129]. To reduce noise and system uncertainty, one thousand repeatedly captured measurement images are averaged as one single measurement image for the wavefront solver. Before starting the AO correction, under collimated illumination, a reference image $i_0(\mathbf{r})$ is captured by showing a “black” screen (zero phase) on the SLM.

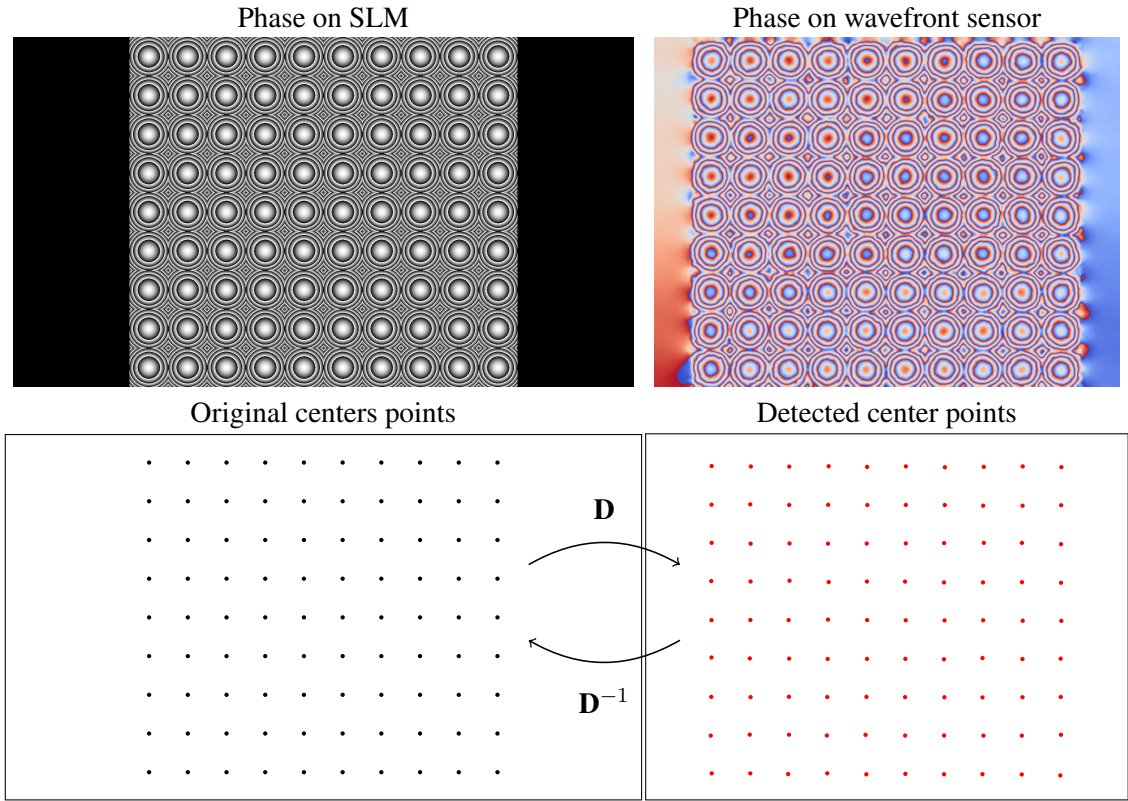


Figure 4.10: Calibration of inverse misalignment transform \mathbf{D}^{-1} . To obtain \mathbf{D}^{-1} , a 2D perspective matrix is calculated by fitting from the detected center points (Coded Wavefront Sensor) to the original ones (phase-only SLM). Detected center points are generated by circular Hough transforms.

Table 4.2: Software performance of our algorithm (1024×1024 unknowns).

Forward/Inverse DCTs	21.24 ms	Bilateral Filters	2.75 ms
Convolutions	2.61 ms	Elementwise	6.19 ms
CPU-GPU Data Transfer	2.88 ms	Warping	0.12 ms
Others	5.01 ms	Overall	40.80 ms

Algorithm parameters

For pyramid up-sampling and down-sampling, a factor of 2 along each coordinate direction is used. In practice for the linear solver $\beta = 5$, $\mu = 100$ or $\mu = 10$ depends on the specific pyramid level, with an ADMM iteration of 10. For the nonlinear warping scheme two pyramid levels and two in-level warping operations are used. The AO loop gain is set as $\alpha = 1$. The bilateral filter window size is 15×15 .

Performance

To avoid tearing artifacts on the phase SLM, the phase-only SLM is set to be V-Sync double buffered. Our controller writes and renders directly to the back buffer, which swaps itself with the front one at V-Sync rate. The wavefront sensor is externally triggered by V-Sync as well, and the wavefront solver runs freely. The SLM, however, suffers from a relatively slow response time and in practice one can see the phase lagging in the measurements made by the wavefront sensor. In other words, phase measurement in our prototype is much faster than the phase correction. To avoid wrong iterations, our total frame rate has to drop down and meet with SLM's update speed, and hence the overall AO performance is limited. Despite hardware latency, Table 4.2 shows the overall benchmark performance for software solely.

4.5 Results

In the following, we present experiments with both simulated as well as real-world distortions. In addition to visual presentation of results, we also use the *Strehl ratio* as a quantitative metric. The Strehl ratio is commonly used to evaluate AO systems, and is defined

as the ratio of the peak brightness of the *actual* Point Spread Function (PSF) of the system to the peak brightness of the *ideal* PSF. The value is therefore between 0 and 1, with 1 being the best. In diffraction limited systems, the ideal PSF is usually the diffraction limited Airy disk. However, since our main camera is not diffraction limited, we instead use the measured PSF of the camera without optical distortions as the reference “ideal” PSF.

4.5.1 Simulation

To have a performance comparison among our proposed high resolution AO system and others, we present here a numerical simulation where large phase distortions are introduced, hence only the Shack-Hartmann and curvature sensors are simulated and compared. For a fair comparison, the free parameters of each wavefront sensor are tuned to best match the incoming phase distortion. For example, we maximize the lenslet number of the Shack-Hartmann wavefront sensor while keeping the maximum target phase distortion slope resolvable. Note that no such parameter tuning is necessary for our own system. All simulated AO systems are equipped with the same high resolution phase-only SLM, the only difference is the wavefront sensors in use.

Figure 4.11 shows a comparison for two different wavefronts, a smooth wavefront (cubic phase) and a turbulent wavefront. The Shack-Hartmann AO system corrects well for smooth wavefronts, but is slow in convergence because it mainly corrects for low frequency terms due to its low spatial wavefront resolution nature, and requires a large number of iterations for final convergence. The Curvature AO system, is not capable of correcting for offset wavefronts, is noise-sensitive and hence not able to maintain stable performance. Our proposed high-resolution AO system outperforms the other two existing AO opponents in terms of both correction (by Strehl ratio) and speed (by number of AO iterations). We also show experiments with lower resolution wavefront correction. As can be expected, the low-resolution actuators are not capable of correcting for highly detailed aberrations, resulting in a large residual error. This demonstrated that both the sensor and the actuator should have

a high spatial resolution in order to apply AO to regular photography and machine vision applications.

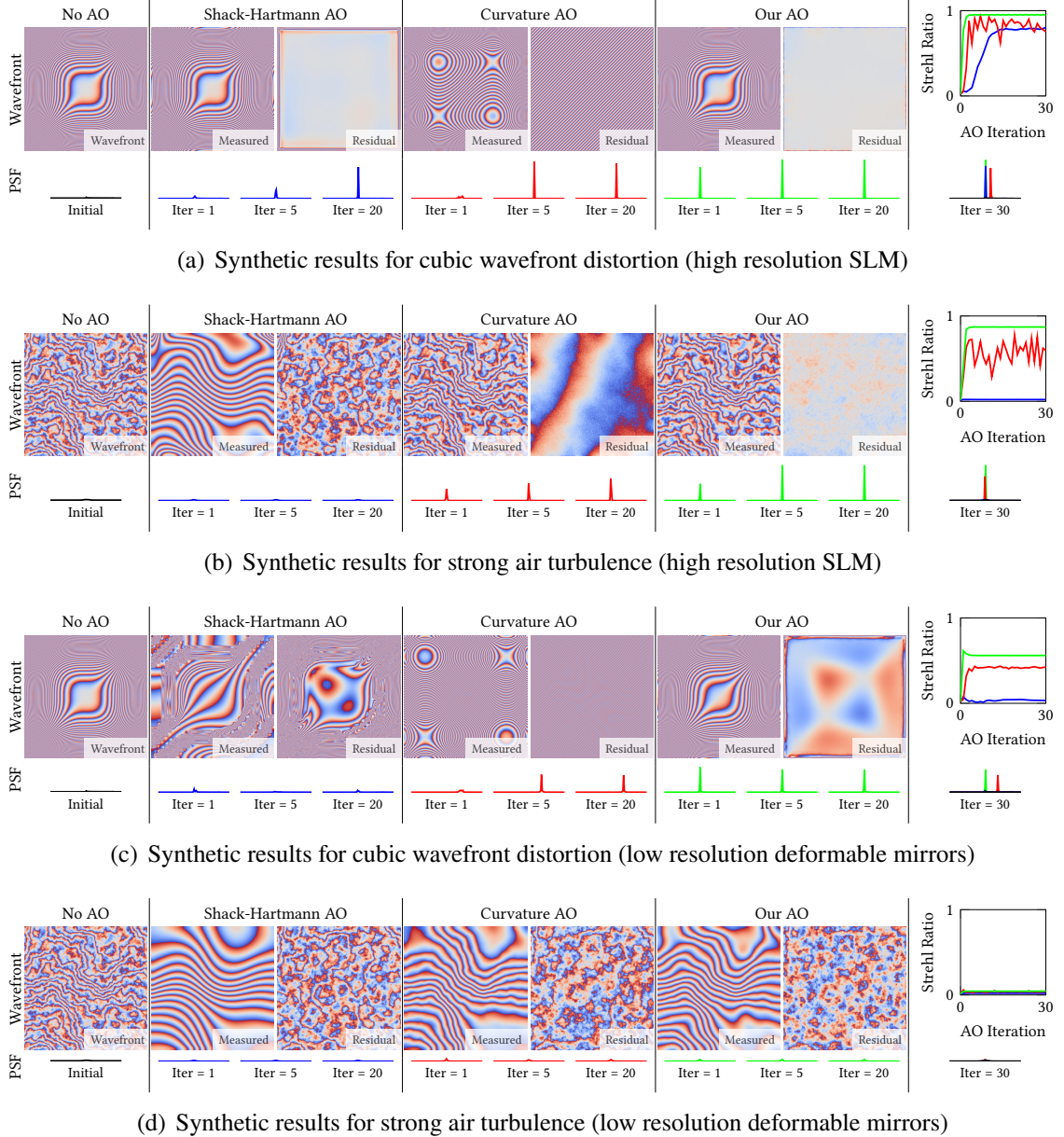


Figure 4.11: Synthetic comparison of large wavefront distortions corrected by AO systems with different wavefront sensors and correctors.

4.5.2 Real experiments

Experimental results are presented, with a nominal wavelength of 532.8 nm being used to quantify wavefront errors.

Point spread function evaluation

To test the performance of our prototype AO system and evaluate the Strehl ratio, a point light source is placed at the object plane. Artificial wrapped phase images are generated on the SLM as initial phase distortions for the AO system to correct with. Figure 4.12 shows the evolution of the AO system, quantified by wavefront RMS and image quality Strehl ratio.

Our AO system performs fast convergence to the null state.

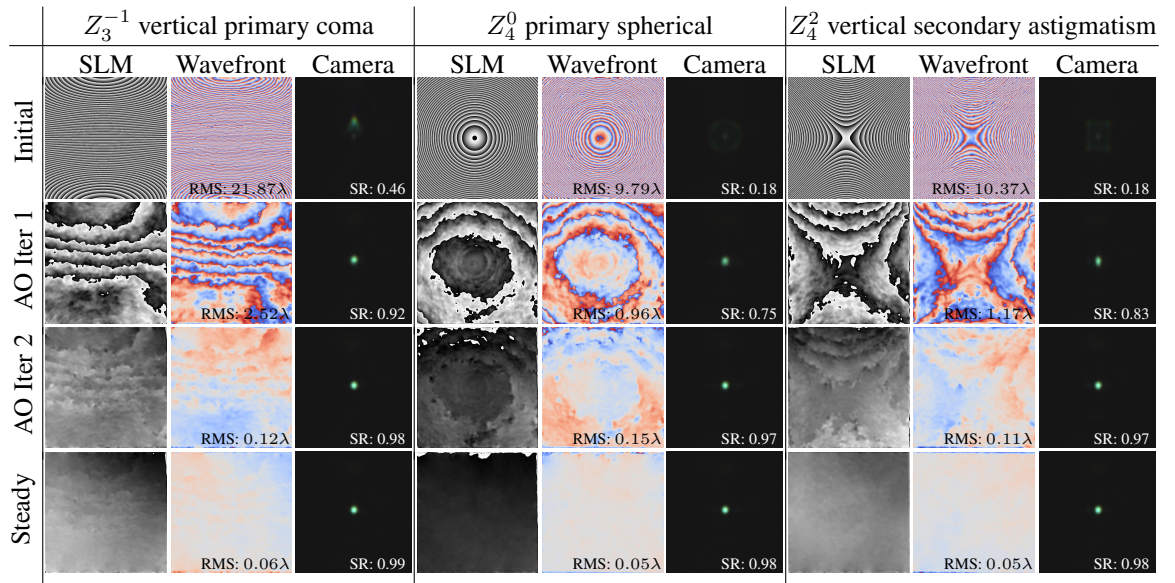


Figure 4.12: PSF experiment with test phase generated on the SLM. Our high resolution AO system is capable to correct distortion and converges in a few iterations. For more visual demonstrations please refer to the Video.

Static deblurring

In order to demonstrate the deblurring capability of our AO system, we introduce phase distortions in the optical path, as shown in Figure 4.7. The arbitrary irregular phase distortions were generated by warping transparent polycarbonate plates when being heated up.

After cooling down to room temperature, local phase distortions are accumulated owing to the thermally introduced curvatures (see Figure 4.7 (e)). This allows us to repeat measurements with and without AO correction. Results are shown in Figure 4.13 where the target objects show significant improvement in focus when the AO system is switched on.

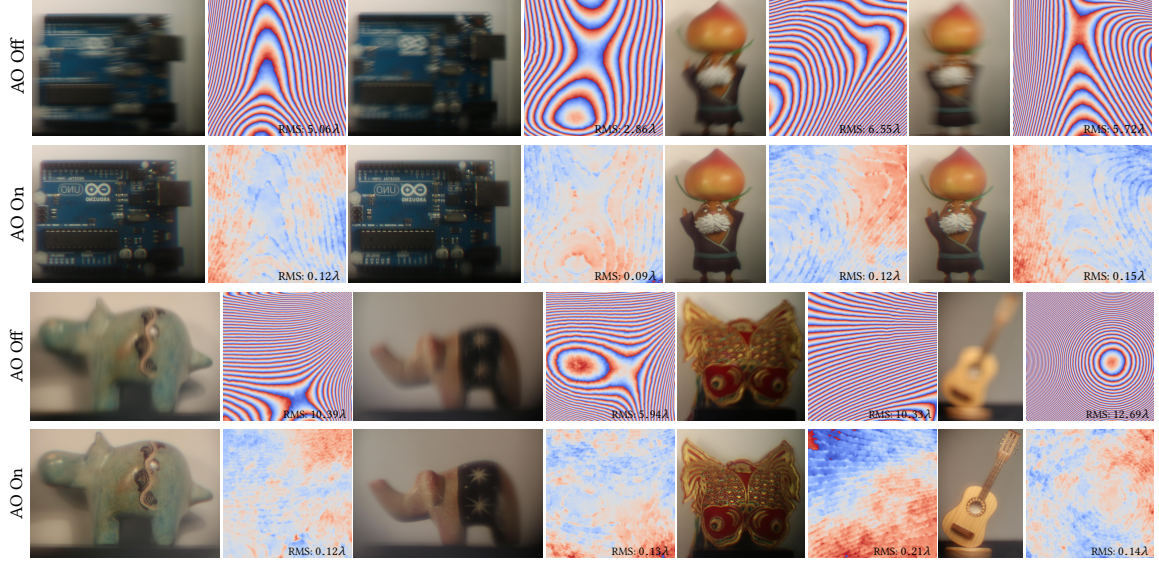


Figure 4.13: Static deblurring for large distortions.

Comparison with software deblurring

We also compare our AO deblurring results with software-only deconvolution algorithms (blind and non-blind) for real data. For blind deconvolution (Figure 4.14, top), the methods are directly applied to the blurred, uncorrected image seen by the camera. For non-blind deconvolution (Figure 4.14, bottom), we assume that a wavefront sensor is available to measure the distortion, but that no actuator is available to correct it. From the measured distortion, and calibrated propagation distances and aperture sizes, it is possible to analytically derive the PSF for the non-blind deconvolution. Due to the prototype nature of our setup, instead of calibrating propagation distance and aperture size, we sampled this parameter space to produce a family of PSFs, and show results for the PSF that produces the best deconvolved result. The results show that being able to measure the PSF with a wavefront

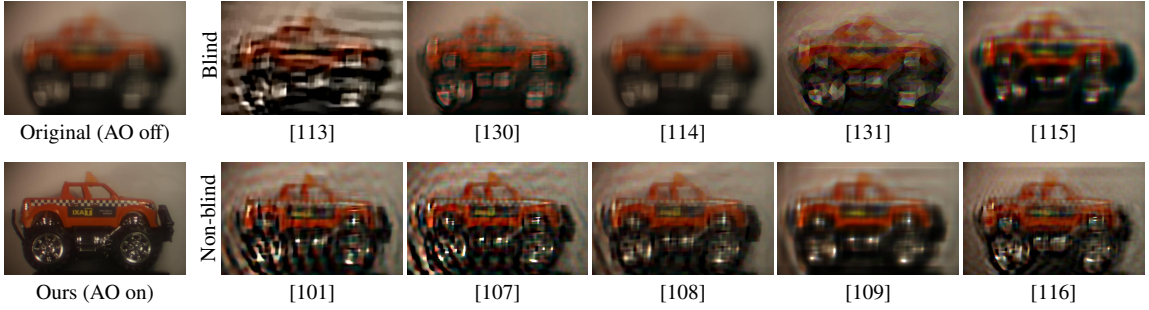


Figure 4.14: Comparison of our AO approach with software-only methods.

sensor does result in sharper reconstructions that fully blind deconvolution. However, the blur is so strong that even the non-blind deconvolution problem is severely ill-posed. As a result, AO as a hardware solution outperforms both blind and non-blind deconvolution by a large margin.

4.6 Discussion and conclusion

In this work, we have demonstrated an adaptive optics system that can sense and correct optical distortions with megapixel spatial resolution and a large magnitude. This system is based on the combination of an improved custom Coded Wavefront Sensor and a readily available phase SLM. With this combination we have for the first time demonstrated the ability to correct for large-scale distortions relevant to machine vision and photography applications using adaptive optics. However, our prototype system does suffer from several limitations, which would be interesting to address in the future.

One limitation of our prototype is that the Field of View (FOV) over which our system is able to compensate is limited. This is known as anisoplanatism in astronomy AO research. The wavefront we sense is only correct for points near the optical axis, and as such the AO performance will degrade with distance from the optical axis. Figure 4.15 demonstrates this effect, as two different phase distortions are imposed in front of the system. If the distortion has a simple structure, for example by introducing a spherical lens or defocusing the main lens, the measured on-axis distortion is a good approximation for a relatively wide FOV.

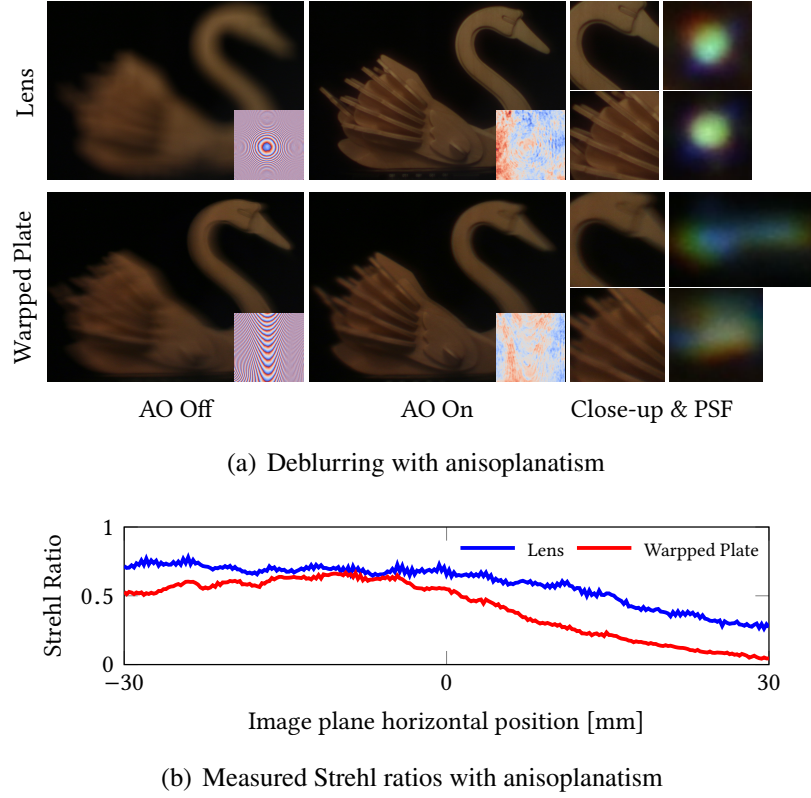


Figure 4.15: Anisoplanatism. (a) A limitation of AO systems like ours is that they only estimate the distorted waveform for one viewing direction. Depending on the complexity of the distortion, this measurement may not accurately represent off-axis distortions, which can therefore not be compensated exactly. In this experiment, center region (the wing) is well-compensated whereas surrounding regions (the head) suffer from incomplete compensation. (b) Strehl ratios decay with increased FOV, and the deblurring performance decreases. The Strehl ratios for the uncorrected wavefronts were so small that they could not be measured accurately with the method from Section 4.5.

However, for a more complex distortion such as warped glass, the wavefront shape and thus the PSF is different for different points on the image plane. While the AO system generally still improves the PSF, it is then not capable of achieving perfect focus. One remedy is multi-conjugate AO [132], where multiple optically conjugated wavefront sensor-corrector pairs are separately grouped and then recombined to correct for volumetric phase distortions. This approach, however, has higher computational cost, and we leave a study of its feasibility in our setting to future work.

Other limitations of the prototype are related to the specific phase SLM that we use. The first limitation is the size – at only $8.6\text{ mm} \times 8.6\text{ mm}$, which limits the total aperture size

of the system, and leads to a long and bulky prototype. We chose the Holoeye phase SLM in part for its large range of phase modulation – up to 3π . However, this large range comes at the expense of reduced phase stability and switching speed; the frame rate of the SLM is the limiting factor for the frame rate of our prototype. However, other phase SLMs with quite different performance tradeoffs are commercially available, and we intend to explore these options in the future.

For the future, we believe it will be exciting to bring adaptive optics systems to photography and machine vision. These are applications where cameras are typically not being operated in a diffraction limited setting, but where optical distortions can be much more severe than in traditional applications of AO. Our work shows that AO is promising in these scenarios, and believe that it presents a major step towards a more widespread adaptation of AO.

Chapter 5

Application: Intensity and Phase Microscopy

In this chapter, we show the second application of the proposed wavefront sensor, a simultaneous intensity & phase microscopy.

Phase imaging techniques are an invaluable tool in microscopy for quickly examining thin transparent specimens. Existing methods are limited to either simple and inexpensive methods that produce only qualitative phase information (*e.g.*, phase contrast microscopy, Differential Interference Contrast (DIC)), or alternative significantly more elaborate and expensive quantitative methods. Here we demonstrate a sensor-side coded, single-shot, low-cost, easy to implement microscopy static setup for quantitative imaging of phase and bright field amplitude using collimated white light illumination.

5.1 Introduction

Due to negligible absorption in the visible spectrum, most living cells exhibit low contrast under bright field microscopy, which prevents detailed examination. In comparison, phase imaging detects minute changes in phase when light propagates through the cell morphology, and has become the prevalent approach for fine cell structure distinction without employing higher radiation powers.

Two classical methods for phase imaging are phase-contrast microscopy [133] and DIC microscopy [134]. These methods utilize additional simple imaging modules (*e.g.*, annulus rings or Nomarski prisms) to convert the phase shifts into brightness changes. However, the conversion is not linear and the recorded image on the detector only indicates qualitative

pseudo phase information, and is often substantially different from the real phase shift.

Several quantitative phase imaging techniques have been proposed [135]. One notable technique is the defocused-based phase imaging [136, 72, 73, 137, 15] based on TIE [21], where two or more intensity images are recorded at several closely spaced planes (usually 10 μm to 100 μm apart). From these images the phase shifts are numerically reconstructed, for example by sequentially solving two Poisson equations [21]. However obtaining the defocused images, may require additional mechanical translations or specifically-designed wavefront-separation components. Digital holographic microscopy [138, 139] records multiple interferograms under different reference beams (via phase shifts or frequency shifts), then post-processing via Fourier analysis [140] interprets the interferograms to recover the sample intensity and phase, and suffers from the challenging ill-posed 2D phase unwrapping problem for fringe pattern analysis due to the periodic nature of interference. Variants of this technique include off-axis digital holography [141], τ interferometers [142, 143], Lloyd's mirror [144], and many others. Digital holography requires additional optical components to realize the different reference beams. One variant is spatial light interference microscopy [145], which minimizes optical path light coherent sensitivity. Other interference-based methods include diffraction phase microscopy [146], similar to Mach-Zehnder interferometry, but overlays the reference and phase-shift beams in the same optical path, by preserving the 1st and 0th order diffraction from a grating using a customized aperture at the Fourier plane. Dynamic interference microscopy [147] employs a micro-polarizer array and phase-shifts are encoded into polarization intensity changes. Apart from above deterministic phase methods (*i.e.*, closed-form formulas for phase-shifts), undetermined or iterative phase solving methods are emerging that rely on phase-retrieval algorithms, for example coded aperture phase imaging [81, 148], which employs a random aperture for phase encoding and an inverse problem is solved via a customized phase retrieval algorithm, or the structured light illumination techniques [11] that captures diffraction holograms under different background illuminations for subsequent numerical phase-retrieval. Ptychogra-

phy [149, 150] and Fourier ptychographic microscopy [10, 151] show the great potential for super-resolution intensity and phase measurement beyond diffraction-limit via multiple angle illumination and a joint phase-retrieval algorithm. Last, the near-field speckle pattern X-ray imaging [152, 153, 154] that utilizes the phase-stepping method is able to obtain phase and scattering field measurements via numerical deconvolution [155, 28]. More recently programmable wavefront sensing techniques have been proposed using programmable spatial light modulators for wavefront encoding [80, 82], and for megapixel adaptive optics [2] combined with a coded wavefront sensor [1].

These approaches measure the actual optical path length differences in the specimen and convert them into thickness, enabling quantitative visualization of sample optical density via the measured phase shift, and some even offer super-resolution or even dark field image reconstructions. However, these approaches require specialized, expensive and complicated setups, coherent illumination, or a long acquisition time prohibited for real time applications. And the flexibility is loss to quickly obtain normal irradiance image and phase image on an ordinary commercially available microscopy.

In this work we demonstrate quantitative phase and intensity imaging based on improvements of our previous work on high-resolution wavefront sensing based on speckle-pattern tracking [1]. Our method only requires minor modifications to a conventional microscope and works under white light illumination. We will further explore the formula Eq. (3.3) in Chapter 3 for simultaneous intensity and phase imaging using the proposed sensor. Using this model combined with modern numerical optimization frameworks, customized algorithms are proposed for simultaneous recovery of amplitude and phase. Superiority of the proposed over classical speckle-pattern tracking algorithm is verified using both synthetic and laboratory data.

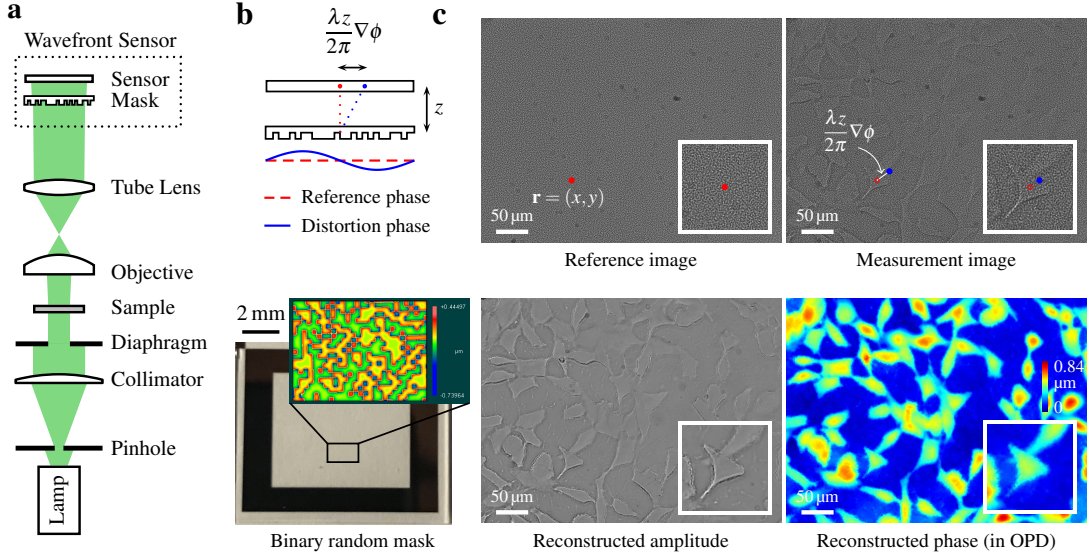


Figure 5.1: Quantitative phase imaging with a coded wavefront sensor. (a) Optical setup for our prototype quantitative phase microscope. Intensity sensor and sample are at conjugate planes, white light incoherent collimated light is configured for sample illumination. (b) Principle of the coded wavefront sensor. A normal intensity sensor is overlaid by a binary phase mask whose Zygo interference map is shown as inset image. (c) The diffraction pattern moves in proportion to local wavefront slopes, as indicated by the red and blue dots. Raw captured images reveal a diffraction pattern movement caused by distortion phase. Inset images are magnified close-ups for regions of interest. Given the image pair, intensity and phase images can be altogether numerically reconstructed for unstained thin transparent cells. The sample contains HeLa cells taken under a $\times 20$ Mitutoyo plan apochromat objective, 0.42 NA.

5.2 Masked sensor for intensity and phase microscopy

5.2.1 Sensor principle

The setup for the proposed quantitative phase imaging microscope requires two modifications to a conventional digital research microscope: 1) replacing the camera with a high resolution coded wavefront sensor [1], and 2) modifying the trans-illumination module for collimated but temporally incoherent light, *i.e.*, broadband spectrum illumination. Figure 5.1(a) shows the optical setup, as well as the coded wavefront sensor, which consists of a random phase mask and a normal intensity sensor. The phase mask is placed close to the sensor at a distance of $z \approx 1.5$ mm. See Methods for z distance calibration details.

Under collimated illumination (and thus spatially coherent), the observed *reference image* $I_0(\mathbf{r})$ is a diffraction pattern of the high frequency mask, as shown in Figure 5.1(b). When a sample is introduced into the optical path, the wavefront is distorted, and the diffraction pattern changes accordingly. Crucially, the wavefront impinging on the sensor is encoded into the movement of the speckle pattern in a *measurement image* $I(\mathbf{r})$. We have previously shown [1] that the wavefront slopes $\nabla\phi$ is optically encoded in image displacements, also known as the “optical flow” in computer vision, written as:

$$I(\mathbf{r}) = I_0 \left(\mathbf{r} - \frac{\lambda z}{2\pi} \nabla\phi \right), \quad (5.1)$$

where z is the distance between mask and sensor, λ is wavelength, and ∇ is the gradient operator. When dispersion is negligible, this coded wavefront sensor works well under temporally incoherent broadband illumination, and hence the retrieved wavefront can be directly mapped to optical path differences (OPD, defined as $\text{OPD} = \frac{\lambda z}{2\pi}\phi$), in the sense that the refractive index n is constant with respect to different wavelengths (weak dispersion assumption) and hence $\text{OPD} = (n - 1) \times d$ is only a variable of sample thickness d . As in other white light wavefront sensing techniques such as Shack-Hartmann, a nominal wavelength (*e.g.*, 532.8 nm) is needed for conversion between OPD and wavefront/phase. The reference image $I_0(\mathbf{r})$ only needs to be captured once prior to any sample measurements, thus this method enables snapshot phase measurement at video rates.

5.2.2 Simultaneous intensity and phase reconstruction

While the observed measurement image $I(\mathbf{r})$ is modulated with the speckle pattern, this pattern can be computationally removed to recover an intensity image free from speckle. To this end, we re-visit the underlining principle of Wang *et al.* [1]. Given that the biological sample is weak in absorption, resulting in a relatively flat intensity profile, simultaneous amplitude and phase estimation can be achieved by modifying the original data term with

additional considerations on sample amplitude and diffraction. We generalize Eq. (5.1) and previous speckle-pattern tracking models [27, 35, 1, 30], via our analysis, as:

$$I \left(\mathbf{r} + \frac{\lambda z}{2\pi} \nabla \phi \right) = \underbrace{|A(\mathbf{r})|^2}_{|\tilde{A}|^2} \left(1 - \frac{\lambda z}{2\pi} \nabla^2 \phi \right) I_0(\mathbf{r}), \quad (5.2)$$

where $A(\mathbf{r})$ is the unknown sample amplitude that we would also like to recover. See Chapter 3 for a short derivation from ray optics, and the relationship between TIE and Eq. (5.2). Given a reference image $I_0(\mathbf{r})$ and measurement image $I(\mathbf{r})$, we simultaneously recover intensity $|A(\mathbf{r})|^2$ and phase $\phi(\mathbf{r})$ from Eq. (5.2). This is a numerically difficult task, that can be made more robust by incorporating prior information on the phase and on the intensity, respectively denoted as $\Gamma_{\text{phase}}(\phi)$ and $\Gamma_{\text{intensity}}(|\tilde{A}|^2)$. The phase and intensity reconstruction process can then be phrased as an optimization problem:

$$\underset{\tilde{A}, \phi}{\text{minimize}} \quad \left\| I \left(\mathbf{r} + \frac{\lambda z}{2\pi} \nabla \phi \right) - |\tilde{A}|^2 I_0(\mathbf{r}) \right\|_2^2 + \Gamma_{\text{phase}}(\phi) + \Gamma_{\text{intensity}}(|\tilde{A}|^2), \quad (5.3)$$

where $\Gamma_{\text{phase}}(\phi)$ and $\Gamma_{\text{intensity}}(|\tilde{A}|^2)$ represent terms for gradient and Hessian sparsity and smoothness, for phase and irradiance respectively (see Section 5.2.3 for details). We optimize each unknown term in an alternating fashion (see Section 5.2.3 for details). This process converges quickly in a few (≈ 3) alternating steps. After obtaining \tilde{A} and ϕ , pure sample amplitude can afterwards be computed by subtracting intensity changes from refocusing (*i.e.*, caustics) due to local wavefront curvature, which, however is a small effect ($\lambda z \nabla^2 \phi \ll 2\pi$):

$$A = \tilde{A} \sqrt{1 + \frac{\lambda z}{2\pi} \nabla^2 \phi}. \quad (5.4)$$

Thanks to modern optimization schemes, the algorithm can be efficiently parallel implemented, enabling GPU acceleration. Our method improves prior speckle-pattern tracking techniques both by accounting for local wavefront curvature (the caustic effect) and amplitude in the model which is crucial for absorption-refraction tangled scenarios in typical

microscopy imaging, and by jointly estimating A and ϕ directly from the raw speckle data. Previous approaches, on the other hand, either fail to consider amplitude [27, 1, 30] and the local curvature term, or apply sequential calculations for estimating A , $\nabla\phi$, and ϕ in separate stages [27, 29, 35, 30], which limits the total reconstruction performance.

For normalized grayscale images valued between 0 and 255, typical tradeoff parameters are $\alpha = 0.1$, $\beta = 0.1$, $\gamma = 100$, and $\tau = 5$. A post-processing on final phase image is necessary in order to remove unwanted tilting artifacts. The ultimate goal of quantitative phase imaging is to find relative phase changes over time within a sample, so it is necessary to isolate the object relative to the background and prevent influence of the variations in the thickness of the coverslip or alignment of the sample relative to the microscope. To achieve this, a least-squares fitted affine plane to the recovered phase is subtracted from the phase estimation to remove undesired tilting artifacts. The whole algorithm was implemented in C++ and CUDA 10.0, and was run on a Ubuntu 18.04 workstation, equipped with Intel(R) Xeon(R) CPU E5-2680 @2.70 GHz (2 \times 16 cores), 62.9 GB memory, and a NVIDIA GPU TITAN X (Pascal). Due to the iterative nature of the solver, we can trade off processing time vs. reconstruction quality. For an 1000×1000 pixel size raw image, with proper pre-caching of constant data (*e.g.*, the reference image), the solver requires in ≈ 97 ms for 3 alternating iterations, and a full run of 10 alternating iterations takes ≈ 317 ms.

5.2.3 Computation

Compared to the general wavefront sensing situations where the target phase is smooth, microscopy phase images contain more detail and many sharp edges. To better formulate and regularize accordingly, we incorporate additional gradient and Hessian priors into the original problem [1] to regularize Eq. (5.2). Introducing tradeoff parameters α , β , γ and τ ,

the phase and intensity regularization terms can be written as:

$$\begin{aligned}\Gamma_{\text{phase}}(\phi) &= \alpha \|\nabla \phi\|_1 + \beta (\|\nabla \phi\|_2^2 + \|\nabla^2 \phi\|_2^2), \\ \Gamma_{\text{intensity}}(|\tilde{A}|^2) &= \gamma \left(\|\nabla |\tilde{A}|^2\|_1 + \|\nabla^2 |\tilde{A}|^2\|_1 \right) + \tau \left(\|\nabla |\tilde{A}|^2\|_2^2 + \|\nabla^2 |\tilde{A}|^2\|_2^2 \right).\end{aligned}\quad (5.5)$$

$\Gamma_{\text{phase}}(\phi)$ and $\Gamma_{\text{intensity}}(|\tilde{A}|^2)$ contain only convolution operators or proxiable functions [59], and hence Eq. (5.3) can be efficiently solved using primal-dual splitting methods such as a customized ADMM [57] solver.

We now discuss how to discretize and solve Eq. (5.3) in a numerical manner, which involves solving an optimization problem in terms of linear algebra. In the following vectors and matrices are denoted as bold small and capital letters, respectively. Absorbing $\lambda z/(2\pi)$ into phase and discretize Eq. (5.3) yields ($|\tilde{A}|^2 \rightarrow \mathbf{a}$ and $\phi \rightarrow \boldsymbol{\phi}$):

$$\underset{\mathbf{a}, \boldsymbol{\phi}}{\text{minimize}} \quad \|\mathbf{i}(\mathbf{r} + \nabla \boldsymbol{\phi}) - \mathbf{a} \odot \mathbf{i}_0(\mathbf{r})\|_2^2 + \underbrace{\alpha \|\nabla \boldsymbol{\phi}\|_1 + \beta \|\mathbf{K}\boldsymbol{\phi}\|_2^2}_{\Gamma_{\text{phase}}(\boldsymbol{\phi})} + \underbrace{\gamma \|\mathbf{Ka}\|_1 + \tau \|\mathbf{Ka}\|_2^2}_{\Gamma_{\text{intensity}}(\mathbf{a})}, \quad (5.6)$$

where \odot denotes Hadamard product, $\mathbf{K} = \begin{bmatrix} \nabla \\ \nabla^2 \end{bmatrix}$ is a concatenated matrix of gradient and Laplacian operators, \mathbf{a} and $\boldsymbol{\phi}$ are the intensity (including the caustic effect) and phase information that we would like to recover. Equation (5.6) is a non-convex problem and is highly ill-posed. To see this, let total pixel numbers be N , note we have $2N$ unknowns (intensity and phase) to estimate whereas only given N equations from Eq. (5.2). The two regularizers, phase prior $\Gamma_{\text{phase}}(\boldsymbol{\phi})$ and intensity prior $\Gamma_{\text{intensity}}(\mathbf{a})$ are hence introduced here to help reducing the ill-posed, but the estimation will still be hard.

To tackle this problem, we devise an alternating algorithm to alternatively solve for intensity and phase, *i.e.*, solve for one when given the other is fixed. Algorithm 4 shows this procedure. In practice we found just a few alternating iterations (< 5) are sufficient for a satisfactory convergence. We now discuss each updating step in more details.

Algorithm 4: Alternating intensity and phase estimation for Eq. (5.6).

```

1 Initialize  $\mathbf{a}^0 = \mathbf{1}$  and  $\phi^0 = \mathbf{0}$ 
2 while not converge do
3   // Intensity update: solve  $\mathbf{a}$  given  $\phi$ 
3    $\mathbf{a}^{K+1} = \arg \min_{\mathbf{a}} \|\mathbf{i}(\mathbf{r} + \nabla \phi^K) - \mathbf{a} \odot \mathbf{i}_0(\mathbf{r})\|_2^2 + \Gamma_{\text{intensity}}(\mathbf{a})$ 
4   // Phase update: solve  $\phi$  given  $\mathbf{a}$ 
4    $\phi^{K+1} = \arg \min_{\phi} \|\mathbf{i}(\mathbf{r} + \nabla \phi) - \mathbf{a}^{K+1} \odot \mathbf{i}_0(\mathbf{r})\|_2^2 + \Gamma_{\text{phase}}(\phi)$ 
5 end

```

Intensity update

We recognize the intensity update step as a variant of the classical ROF denoising problem [156]:

$$\underset{\mathbf{a}}{\text{minimize}} \quad \|\mathbf{a} \odot \mathbf{i}_0(\mathbf{r}) - \mathbf{i}(\mathbf{r} + \nabla \phi^K)\|_2^2 + \gamma \|\nabla \mathbf{a}\|_1 + \tau \|\mathbf{K}\mathbf{a}\|_2^2. \quad (5.7)$$

Equation (5.7) is convex but non-differentiable. By introducing a slack variable $\mathbf{b} = \nabla \mathbf{a}$ that represents image gradient, via de-coupling diagonalization (though not strictly equivalent, in practice we found in this formation it is easier to formulate the solver and to converge), denoting $\mathbf{i}_{\text{warp}}^K = \mathbf{i}(\mathbf{r} + \nabla \phi^K)/\mathbf{i}_0(\mathbf{r})$, the original objective function in Eq. (5.7) can be split and approximated as:

$$\underset{\mathbf{a}, \mathbf{b}}{\text{minimize}} \quad \underbrace{\|\mathbf{a} - \mathbf{i}_{\text{warp}}^K\|_2^2 + \tau_{\text{new}} \|\mathbf{K}\mathbf{a}\|_2^2}_{f(\mathbf{a})} + \underbrace{\gamma_{\text{new}} \|\mathbf{b}\|_1}_{g(\mathbf{b})}, \quad (5.8)$$

subject to $\mathbf{b} = \nabla \mathbf{a}$,

where $\tau_{\text{new}} = \tau / (\overline{(\mathbf{i}_{\text{warp}}^K)^2})$ and $\gamma_{\text{new}} = \gamma / (\overline{(\mathbf{i}_{\text{warp}}^K)^2})$ where over-line denotes the mean. Apply the ADMM method[57] to Eq. (5.8), we yield Algorithm 5, where $\text{prox}_{g/\mu}(\mathbf{u})$ denotes the proximal operator[59] of function g with parameter μ , given the input vector \mathbf{u} . And $\boldsymbol{\eta}$ is the dual variable. Now we briefly discuss each updating step.

a-update This step implements a straightforward Poisson solver, and we solve it in the

Algorithm 5: ADMM for solving Eq. (5.8).

```

1 Initialize  $\mathbf{a}^0, \mathbf{b}^0$  and  $\boldsymbol{\eta}^0$ , set  $\mu > 0$ 
2 while not converge do
3   a-update:  $\mathbf{a}^{k+1} \leftarrow \arg \min_{\mathbf{a}} f(\mathbf{a}) + \mu \|\nabla \mathbf{a} - \mathbf{b}^k + \boldsymbol{\eta}^k\|_2^2$ 
4   b-update:  $\mathbf{b}^{k+1} \leftarrow \text{prox}_{g/\mu}(\nabla \mathbf{a}^{k+1} + \boldsymbol{\eta}^k)$ 
5   η-update:  $\boldsymbol{\eta}^{k+1} \leftarrow \boldsymbol{\eta}^k + \nabla \mathbf{a}^{k+1} - \mathbf{b}^{k+1}$ 
6 end

```

spectral domain assuming symmetric boundary conditions. Exploiting the DCT, denoted as \mathcal{F}_{DCT} , then:

$$\begin{aligned}
\mathbf{a}^{k+1} &= \arg \min_{\mathbf{a}} \|\mathbf{a} - \mathbf{i}_{\text{warp}}^K\|_2^2 + \tau_{\text{new}} \|\mathbf{K}\mathbf{a}\|_2^2 + \mu \|\nabla \mathbf{a} - \mathbf{b}^k + \boldsymbol{\zeta}^k\|_2^2 \\
&= (\mathbf{I} + \tau_{\text{new}} \mathbf{K}^T \mathbf{K} + \mu \nabla^2)^{-1} (\mathbf{i}_{\text{warp}}^K + \mu \nabla^T (\mathbf{b}^k - \boldsymbol{\zeta}^k)) \\
&= \mathcal{F}_{\text{DCT}}^{-1} \left(\frac{\mathbf{i}_{\text{warp}}^K + \mu \mathcal{F}_{\text{DCT}}(\nabla^T (\mathbf{b}^k - \boldsymbol{\zeta}^k))}{1 + (\mu + \tau_{\text{new}}) \mathcal{F}_{\text{DCT}}(\nabla^2) + \tau_{\text{new}} \mathcal{F}_{\text{DCT}}(\nabla^4)} \right). \tag{5.9}
\end{aligned}$$

Exploiting the FFT algorithms for all the DCT operations, the **a**-update can be efficiently done in parallel.

b-update This step is an element-wise estimation and the solution is readily obtained by the so-called shrinkage operator that is embarrassingly parallel, where $\text{sign}(\cdot)$ denotes the element-wise signum function:

$$\begin{aligned}
\mathbf{b}^{k+1} &= \text{prox}_{g/\mu}(\nabla \mathbf{a}^{k+1} + \boldsymbol{\eta}^k) \\
&= \arg \min_{\mathbf{b}} \gamma_{\text{new}} \|\mathbf{b}\|_1 + \mu \|\mathbf{b} - (\nabla \mathbf{a}^{k+1} + \boldsymbol{\eta}^k)\|_2^2 \\
&= \text{sign}(\nabla \mathbf{a}^{k+1} + \boldsymbol{\eta}^k) \cdot \max \left(|\nabla \mathbf{a}^{k+1} + \boldsymbol{\eta}^k| - \frac{\gamma_{\text{new}}}{2\mu}, \mathbf{0} \right). \tag{5.10}
\end{aligned}$$

After obtaining \mathbf{a}^K , a median filter (window of 3×3) is imposed to further suppress speckle noise. In practice we found the median filtering is significant for better performance.

Phase update

For phase update, people usually do the digital image correlation method [157], which however in computer vision is known as a variant of the famous Lucas–Kanade method [158] for optical flow computation. Here we modify and improve our previously proposed wavefront solver to fit the assumption for normal microscopy samples. Consequently the wavefront solver presented here is a variant of Wang et al. [1] Recall the following optimization problem to update phase:

$$\underset{\phi}{\text{minimize}} \quad \| \mathbf{i}(\mathbf{r} + \nabla \phi) - \mathbf{a}^{K+1} \odot \mathbf{i}_0(\mathbf{r}) \|_2^2 + \alpha \| \nabla \phi \|_1 + \beta \| \mathbf{K} \phi \|_2^2, \quad (5.11)$$

where $\alpha > 0$ and $\beta > 0$ are weighting parameters. Note the data fitting term (ℓ_2 -norm) is non-convex and one of the data prior term (ℓ_1 -norm) is convex but non-smooth and non-differentiable. Since the phase shifts are usually small, we linearize $\mathbf{i}(\mathbf{r} + \nabla \phi)$ around \mathbf{r} . It yields:

$$\underset{\phi}{\text{minimize}} \quad \| \nabla \mathbf{i} \cdot \nabla \phi + \mathbf{i}(\mathbf{r}) - \mathbf{a}^{K+1} \odot \mathbf{i}_0(\mathbf{r}) \|_2^2 + \alpha \| \nabla \phi \|_1 + \beta \| \mathbf{K} \phi \|_2^2. \quad (5.12)$$

To handle the boundary condition (which may introduce reconstruction artifacts in conventional phase-from-slope techniques), we add a selection matrix \mathbf{M} to include the unknown boundary values as additional variables to be optimized. [89] In linear algebra, denote $\mathbf{g}_t = \mathbf{i}(\mathbf{r}) - \mathbf{a}^{K+1} \odot \mathbf{i}_0(\mathbf{r})$, Eq. (5.12) reads as:

$$\underset{\phi}{\text{minimize}} \quad \| \nabla \mathbf{i} \cdot \mathbf{M} \nabla \phi + \mathbf{g}_t \|_2^2 + \alpha \| \nabla \phi \|_1 + \beta \| \mathbf{K} \phi \|_2^2. \quad (5.13)$$

Equation (5.13) is convex but non-differentiable. By introducing a slack variable $\mathbf{w} = \nabla\phi$ that represents phase gradient, the original objective function in Eq. (5.13) can be split as:

$$\begin{aligned} & \underset{\phi, \mathbf{w}}{\text{minimize}} \quad \underbrace{\beta \|\mathbf{K}\phi\|_2^2}_{f(\phi)} + \underbrace{\|\nabla \mathbf{i} \cdot \mathbf{M}\mathbf{w} + \mathbf{g}_t\|_2^2}_{g(\mathbf{w})} + \alpha \|\mathbf{w}\|_1, \\ & \text{subject to } \mathbf{w} = \nabla\phi. \end{aligned} \quad (5.14)$$

Apply the ADMM method [57] to Eq. (5.14), we yield Algorithm 6.

Algorithm 6: ADMM for solving Eq. (5.14).

```

1 Initialize  $\phi^0, \mathbf{w}^0$  and  $\eta^0$ , set  $\mu > 0$ 
2 while not converge do
3    $\phi$ -update:  $\phi^{k+1} \leftarrow \arg \min_{\phi} f(\phi) + \mu \|\nabla\phi - \mathbf{w}^k + \eta^k\|_2^2$ 
4    $\mathbf{w}$ -update:  $\mathbf{w}^{k+1} \leftarrow \text{prox}_{g/\mu}(\nabla\phi^{k+1} + \eta^k)$ 
5    $\eta$ -update:  $\eta^{k+1} \leftarrow \eta^k + \nabla\phi^{k+1} - \mathbf{w}^{k+1}$ 
6 end

```

ϕ -update This step is a Poisson solver, and we solve it in the spectrum domain assuming symmetric boundary conditions:

$$\begin{aligned} \phi^{k+1} &= \arg \min_{\phi} \beta \|\mathbf{K}\phi\|_2^2 + \mu \|\nabla\phi - \mathbf{w}^k + \zeta^k\|_2^2 \\ &= (\beta \mathbf{K}^T \mathbf{K} + \mu \nabla^2)^{-1} \mu \nabla^T (\mathbf{w}^k - \zeta^k) \\ &= \mathcal{F}_{\text{DCT}}^{-1} \left(\frac{\mu \mathcal{F}_{\text{DCT}}(\nabla^T (\mathbf{w}^k - \zeta^k))}{\beta \mathcal{F}_{\text{DCT}}(\nabla^4) + (\beta + \mu) \mathcal{F}_{\text{DCT}}(\nabla^2)} \right). \end{aligned} \quad (5.15)$$

\mathbf{w} -update This involves evaluation of $\mathbf{w}^{k+1} = \text{prox}_{g/\mu}(\mathbf{u})$ with $\mathbf{u} = \nabla\phi^{k+1} + \eta^k$, i.e., the proximal operator [59] of $g(\mathbf{w})$ with parameter μ , which is defined as:

$$\begin{aligned} \text{prox}_{g/\mu}(\mathbf{u}) &= \arg \min_{\mathbf{w}} g(\mathbf{w}) + \mu \|\mathbf{w} - \mathbf{u}\|_2^2 \\ &= \arg \min_{\mathbf{w}} \|\nabla \mathbf{i} \cdot \mathbf{M}\mathbf{w} + \mathbf{g}_t\|_2^2 + \mu \|\mathbf{w} - \mathbf{u}\|_2^2 + \alpha \|\mathbf{w}\|_1. \end{aligned} \quad (5.16)$$

Equation (5.16) is separable in \mathbb{R}^2 as many Least Absolute Shrinkage and Selection Oper-

ator (LASSO) problems, which can be solved in the dual form in the formations of linear systems, which are 2-by-2 small matrices that have closed-form solutions for inversion. Conclusively, for \mathbf{w} -update we have closed-form solutions, which are all element-wise operations and hence the \mathbf{w} -update step is easy parallelization as well. By far, all the operations in Algorithm 6 can be parallelized, and hence the total computation can be efficiently run on distributed computing machines. *e.g.*, on a commercially affordable GPU.

After obtaining ϕ^K , we approximate the warped measurement image as $\mathbf{i}(\mathbf{r} + \nabla\phi^K) \approx \mathbf{i}(\mathbf{r}) + \nabla\mathbf{i} \cdot \nabla\phi^K$, and run next intensity update estimation in Algorithm 6. For even larger wavefronts, pyramid schemes can be adopted, as in Wang et al. [2] The spirit behind is a similar manner of the nonlinear warping scheme in optical flow [128].

5.3 Results

5.3.1 Characterization of a microlens array

To demonstrate the accuracy of our quantitative phase imaging microscope, a square grid microlens array (MLA150-7AR-M, Thorlabs) was imaged, for which each lenslet is of 150 μm apart and 6.7 mm back focal length. We compare our method to both Zygo measurements and a classical baseline speckle-pattern tracking algorithm [35] in Figure 5.2. The measured optical path differences are converted to physical thickness using a refractive index of 1.46 at 532.8 nm (fused silica). Figure 5.2(c) shows cross-sectional thickness profiles for one of the microlenses. Our reconstructed height matches Zygo measured data, which is also indicated by the RMS error computed for each cross-section microlens phase profile, whereas the baseline algorithm is 0.20 μm . This laboratory result validates that, for visible light optical microscopy phase imaging, our proposed numerical algorithm outperforms classical speckle-tracking algorithms, which suffer from phase reconstruction error because of their sequential nature. Our previous algorithm curl-free optical flow [1] is overall in good agreement with both the Zygo measurements and our proposed method, however

there exists high-frequency noise.

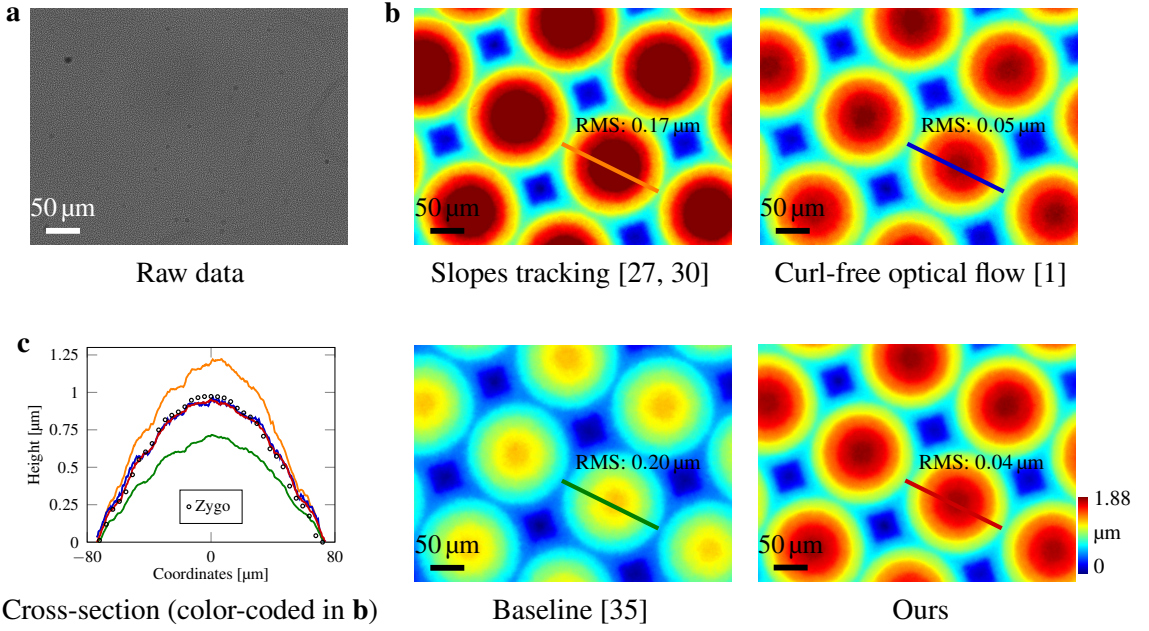


Figure 5.2: Accuracy validation measurement using a microlens array. Image was taken under a $\times 20$ Mitutoyo plan apochromat objective, 0.42 NA. (a) Raw data. (b) In comparison with the manufacturer's specification, both curl-free optical flow [1] and our proposed algorithm estimate the height with high accuracy. By comparison, classical slope tracking [27, 30] overestimates, and the baseline method [35] underestimates the phase shifts. (c) For cross-section comparison all heights have been normalized to start from 0 μm.

5.3.2 Influence of irradiance-varying samples

Figure 5.3 demonstrates the advantage of Eq. (5.2) over Eq. (5.1) on an air-dried human blood cell smear. Phase-only reconstruction results are shown to compare different methods. In such an irradiance-varying situation, previous pure flow-tracking algorithms [27, 30, 1] are vulnerable to the amplitude changes. Classical baseline methods for speckle-pattern tracking [35] based on local window intensity estimation and windowed correlation, however, tend to underestimate the phase shifts, as also shown previously in the validation experiment Figure 5.2.

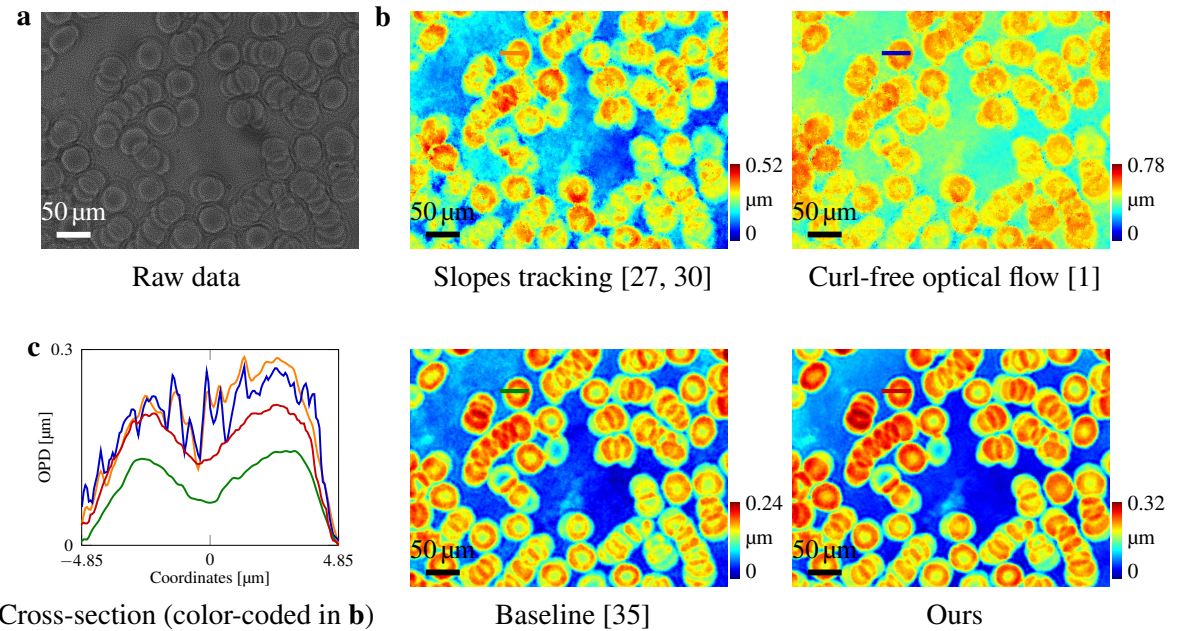


Figure 5.3: Phase reconstruction comparison for an air-dried human red blood cell smear using different methods. Image was taken under a $\times 100$ Mitutoyo plan apochromat objective, 0.70 NA. **(a)** Raw data. **(b)** Reconstruction phase shifts from different methods. **(c)** Cross-section profile of a single cell, phases are normalized to start from height 0 μm . The two pure-tracking methods based on Eq. (5.1), *i.e.*, slopes tracking [27, 30] and curl-free optical flow [1], are vulnerable to amplitude changes and fail to reconstruct the bowl-like indentations because their model neglects sample amplitude. Though based on Eq. (5.2), traditional baseline method [35] underestimates the phase shifts (as well in Figure 5.2), whereas our reconstruction height maps match the metrology statistics [159].

5.3.3 Imaging of transparent cells

We also show the capability of imaging unstained thin transparent cells using the proposed quantitative phase microscopy. From one single raw speckle data, simultaneous amplitude and phase images are numerically reconstructed as shown in Figure 5.4 for different cells. The phase images are shown as the measured OPD, and the actual height of the samples can be calculated when true refractive indexes are known. Noticeably, the torus structures of the red blood cells have been plausibly reconstructed. For the human cheek cell sample, the phase map indicates its biological structure with height informational details (compared to bright field imaging). For the HeLa cells sample, the humongous phase changes of the dying cells reveal the bio-activity, providing informative contrast details beyond original bright field microscopy or even qualitative phase microscopy methods *e.g.*, phase-contrast or DIC. For the MCF-7 cells, note how our method enables fine phase reconstruction at the boundaries while preserving the original bright field image. Since the quantitative phase information is obtained, all other phase microscopy such as phase-contrast and DIC can be numerically simulated.

5.3.4 Digital refocusing

Finally, we demonstrate the digital refocusing capability of the proposed technique. Since the full complex field is acquired, similar to digital holography, we are able to perform digital refocusing on the recovered intensity and wavefront. However unlike digital holography, our approach employs broadband illumination (multiple wavelengths), and the concept of phase is ill-defined. Hence, we define a nominal wavelength $\lambda = 532.8 \text{ nm}$, and convert the obtained wavefront (OPD-based [μm]) into phase (unitless [rad]). Two examples are shown in Figure 5.5. In Figure 5.5(a), the previously obtained microlens is digitally propagated through different defocus distance Δf . The best focus distance matches the back focal length provided by manufacturer. Cross-section phase profiles also demonstrate evolution of the propagating wavefront, from converging to almost flat, and finally to diverging. In

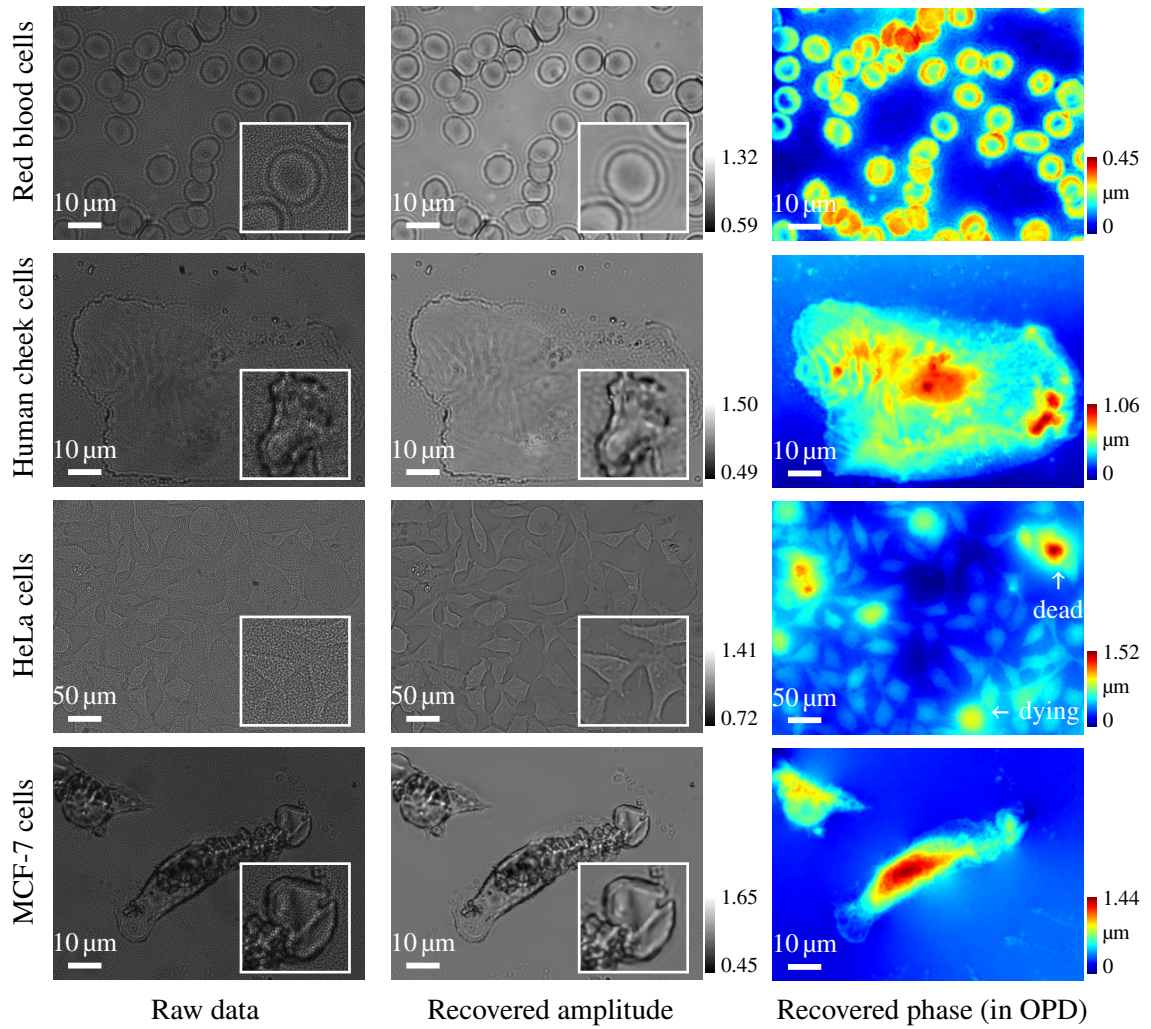


Figure 5.4: Experimental results with unstained thin transparent cells with the proposed quantitative phase imaging pipeline. Images were taken under $\times 20$ (0.42 NA) and $\times 100$ (0.70 NA) Mitutoyo plan apochromat objectives. Phase images are shown in terms of OPD, where optically thick structures reveal informative details regarding the samples. Inset close-up images (normalized for better visualization) show local areas of interest, note in the recovered amplitude images the speckle patterns have been fully removed. Cell live/dead viability can be quickly examined via phase measurements.

Figure 5.5(b), digital refocusing of blood cells to the correct focus plane sharpens the edges of the originally blurry intensity image, and the bowl-like indentation is more obvious and plausible for the central cell, as shown in the cross-section.

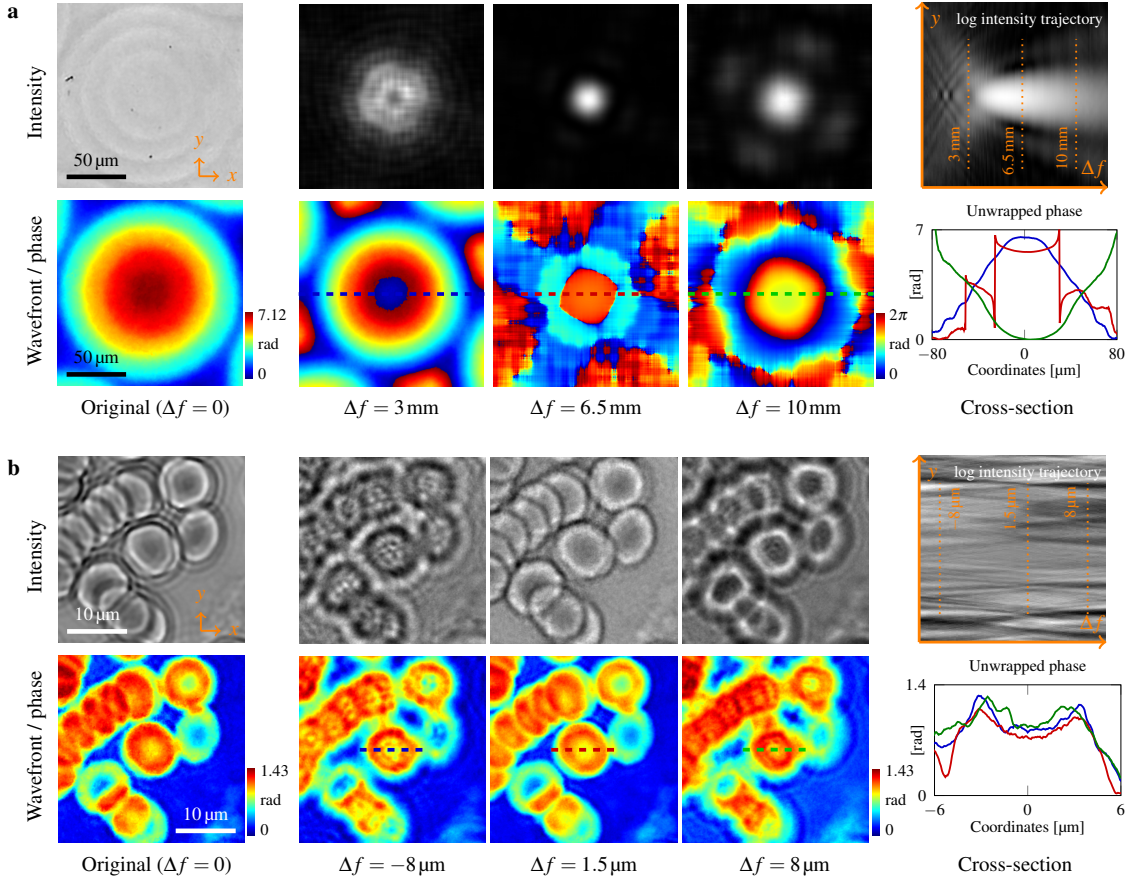


Figure 5.5: Post-capture refocusing by digitally propagating defocus distance Δf with the acquired complex field. **(a)** Digital refocusing of a microlens scalar field in Figure 5.2 is made possible once its intensity and wavefront are obtained via our approach. For different Δf , the defocusing evolution of a diffraction-limited spot can be emulated. **(b)** Digital refocusing can also be performed to remove the original ringing artifacts due to defocusing. Refocusing blood cells in Figure 5.4 sharpens the intensity images, and provides a more plausible phase profile for originally out-of-focus samples.

5.4 Analysis and calibration

5.4.1 Wavefront resolution analysis

Derivation for Eq. (5.2) (see in Chapter 3) requires small curvature assumption that

$$\frac{\lambda z}{2\pi} |\nabla^2 \phi(\mathbf{r})| = |\nabla^2 \text{OPD}| \ll 1/z. \quad (5.17)$$

This condition determines the wavefront resolution of our technique: the incoming wavefront local curvature must be small enough, indicated by upper bound $1/z$. This upper bound could be interpret in terms of Fourier harmonics, to derive the phase transfer function for our sensor. Let $\text{OPD} = H \cos \omega x$, then:

$$|\nabla^2 \text{OPD}| \ll 1/z \Rightarrow H\omega^2 |\cos \omega| \leq H\omega^2 \ll 1/z \Rightarrow H \ll H_{\text{upper_bound}} = \frac{1}{z\omega^2}. \quad (5.18)$$

However, this theoretical upper bound $1/z$ is not tight, and the actual performance needs to be measured experimentally. Results are shown in Figure 5.6, where we measured groups of gradually increasing curvature phase maps, using setup in Figure 5.7(a). We notice our sensor starts to fail at wavefront curvature of 75 m^{-1} , whereas the upper bound indicates $1/z \approx 700 \text{ m}^{-1}$. It agrees with the general rule of thumb that \ll indicates an order of magnitude relationship. Given this number, we are able to compute the phase transfer function $H_{\text{measured}}(\omega)$, *i.e.*, the practical wavefront resolution.

However, the actual resolution also depends on the microscopy objective, since current image sensor technology makes it easy to choose sensor resolutions that exceed the optical resolution of the microscope, especially in high magnification microscopy. Most of our experiments were conduct with a $100\times$ objective (0.70 NA), at nominal wavelength $\lambda = 532.8 \text{ nm}$, corresponding to Rayleigh resolution of $100 \times 0.61\lambda/\text{NA} = 46.4 \mu\text{m}$ (*i.e.*, $\omega_{\text{objective}} = 0.07 \text{ rad}/\mu\text{m}$), which is 7.2 times larger than our prototype sensor pixel size $6.45 \mu\text{m}$ (*i.e.*, $\omega_{\text{pixel}} = 0.49 \text{ rad}/\mu\text{m}$). Given the measured limit $\omega_{\text{limit}} = 0.14 \text{ rad}/\mu\text{m}$ in Figure 5.6, we have $\omega_{\text{objective}} < \omega_{\text{limit}} < \omega_{\text{pixel}}$, hence the wavefront resolution is limited by $\omega_{\text{objective}}$, *i.e.*, the full system is limited by the optical performance of the microscope objective. Note that $\omega_{\text{objective}}$ could be improved by using objectives with higher NA, and ω_{limit} could also be improved by adjusting the distance z between mask and sensor, to which the theoretical upper bound is inversely proportional. This provides a rich design space for performance optimized systems based on our approach.

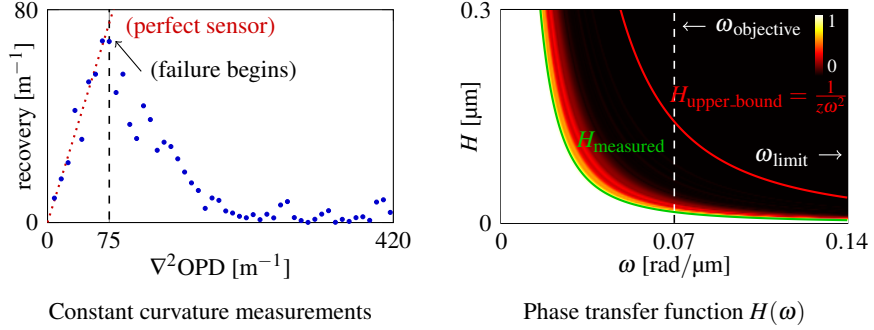


Figure 5.6: Wavefront resolution analysis and the phase transfer function. Our recovered wavefront curvatures are plotted for groups of gradually increasing constant phase curvature $\nabla^2\text{OPD}$. For $\nabla^2\text{OPD} > 75 \text{ m}^{-1}$, our sensor begins to fail for recovery. Based on this measured failure starting curvature, we are able to compute the valid area (valued from 0 to 1) for phase transfer function based on the recovery error (larger the error, smaller the value). According to Eq. (5.18), our measured tight bound H_{measured} and the upper bound $H_{\text{upper_bound}}$ are shown. However our prototype resolution is limited by the optical resolution of the microscope objective $\omega_{\text{objective}} = 0.07 \text{ rad}/\mu\text{m}$ instead of the measured limit $\omega_{\text{limit}} = 0.14 \text{ rad}/\mu\text{m}$.

5.4.2 Calibration

According to Eq. (5.2), to correctly map from the numerically reconstructed surface to the original wavefront, an accurate calibration of the distance z is important and necessary. The exact distance is calibrated and characterized in another separate experiment as described in Figure 5.7. This is accomplished by comparison between our numerical reconstruction wavefronts and the ground truth wavefronts. Figure 5.7(a) shows the optical setup, where a plasma broadband white light source (HPLS245, Thorlabs) is used for illumination. A pre-calibrated reflective phase-only spatial light modulator (SLM) (PLUTO-2-VIS-016, Holoeye) is configured to interpret grayscale images as 2π phase wrapping, for generating ground truth wavefronts. Some examples are shown in Figure 5.7(b). A linear polarizer ensures the SLM operates in the pure phase modulation mode. The relay lenses (two $f = 125 \text{ mm}$ cemented achromatic doublets, AC254-125-A, Thorlabs) conjugate the SLM to the wavefront sensor plane at $\times 1$ magnification ratio. By comparing the algorithm output wavefronts with the ground truth in Figure 5.7(b), and with the known sensor pixel size $6.45 \mu\text{m}$ and SLM pixel size $8 \mu\text{m}$, for each slope the calibrated distances are computed as in Figure 5.7(c),

where their mean is $z = 1.43$ mm.

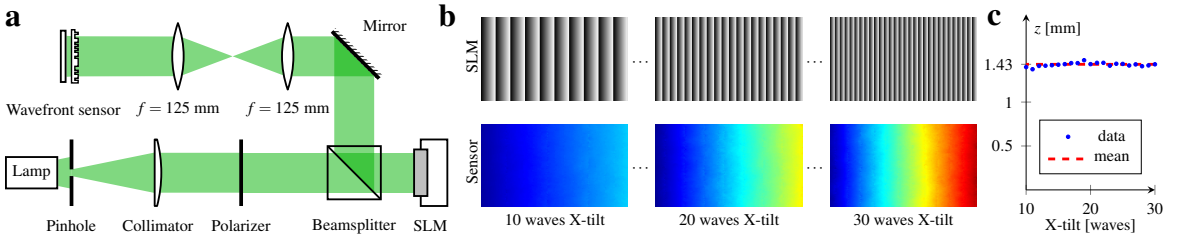


Figure 5.7: Calibration of wavefront sensor scaling factor. (a) Optical setup for wavefront sensor calibration. The sensor plane and the SLM plane are in conjugate. (b) Input grayscale phase images to the SLM and reconstructed wavefront surfaces (after image resizing). (c) Estimated mask-to-sensor distances from (b) over different ground-truth slopes, and the mean.

5.5 Discussion and conclusion

5.5.1 Discussion

All data required to determine the phase shift are gathered in a single snapshot utilizing a coded wavefront sensor, so there is no need for scanning, which however is one potential future research direction to obtain scattering images [160, 161, 35]. Specific grating (mask) designs or multi-layer designs [162, 163] are potential directions. The fast simultaneous amplitude and phase acquiring advances current tomography techniques [164, 165] beyond X-ray. Short exposure times freeze motion, allowing a capture for fast movements. From the reconstructed phase, different types of phase imaging techniques can be emulated, such as phase contrast and DIC images, are also obtained simultaneously along with the recovered optical thickness.

The proposed technique can be further extended to higher magnifications, immersion objectives, higher numerical apertures, to measure thin and transparent specimens under incoherent illumination. The avoidance of laser illumination offer a non-destructive means of observing and quantifying biological behavior and cellular dynamics over time, at a harmless lighting level.

5.5.2 Conclusion

We have demonstrated the proposed quantitative phase imaging pipeline for simultaneous amplitude and phase reconstruction via minor modifications on an ordinary optical microscopy. Our new theoretical model establishes the connection between speckle-pattern tracking and TIE-based determined phase retrieval. Powered by an efficient joint optimization numerical scheme, we show computational potentials for better performance using the same raw speckle image. Through imaging different transparent cells, amplitude and phase reconstruction results are present. We believe using the coded wavefront sensor, without additional hardware, the potential to transform an ordinary bright field microscopy to multi-functional microscopy for simultaneous quantitative phase and amplitude imaging opens up new research directions and inspiring applications.

Chapter 6

Differentiable Lens Design

Unlike previous chapters where *sensing* is the major emphasis, this chapter focuses on *design & manipulation*, *i.e.*, custom wavefront engineering via lens designs. In this chapter, we introduce the notion of differentiable lens, a ray tracing lens design engine based on automatic differentiation.

We introduce DiffLens, a gradient-assistant ray tracing engine using automatic differentiation, for complex lens group or freeform optimization, end-to-end designs, and calibration applications. The engine builds on a memory-efficient differentiable ray-surface intersection solver, with refraction and dispersion modeled. The engine can produce spot diagrams or render photo-realism images for real designs such as asphere lens or Double Gauss, despite being able to infer derivatives with respect to design parameters. Starting from an initial design, the gradient information can be employed for asphere surface optimization, sensitivity analysis, and freeform caustic engineering, demonstrated by multiple design examples. The engine can also be combined with a neural network for end-to-end optimization by back-propagating optics and network parameters, validated by a wavefront coding joint-design. Beyond design problems, we show a reverse usage of the engine as a back-engineering solver to estimate misalignment of a lens setup. Given the variety of applications, we believe the potentials of such an engine to open up a new solution approach to lens design and relevant problems.

6.1 Introduction

Lens design aims to produce an optimal lens group for specific applications, and is an old topic in applied optics. This process is challenging and computationally intensive, because (i) ray tracing and relevant techniques are required to forward model how optical elements jointly affect the passed through light, and (ii) specific algorithms are needed to inversely estimate the design parameters for optimal performance. Long before computers were prevalent, most designs were done by hand [166]. Starting in the 1950s, the notion of automatic or computer-aided designs was proposed [167, 168, 169, 170, 171] with the help of digital computers. With the continual evolution of modern computing machines, automatic lens design software, such as ZEMAX [172] and Code V [173], is nowadays a norm in the optical society. These classical design implementations are based on a computational pipeline that formulates the design problem as minimizing a merit function that is usually the sum of a set of weighted aberrations squared, which are nonlinear functions of the variable parameters. The optimization is performed using damped least squares [170, 174], *i.e.*, the Levenberg-Marquardt algorithm [175], where the aberration functions are linearized to first Taylor series, resulting in a linear system solved by diagonal regularization. The linearization requires gradient estimation to compute the Jacobian matrices, and are normally obtained by finite difference approximation.

This computational pipeline is however to be improved, to meet the new demand of domain-specific applications. For example, in freeform optics optimization [176], when the number of variables is too many to efficiently formulate such a linear system, domain-specific new design methodologies were proposed, such as ray mapping tailoring [177, 178] and variants [179, 180]. In hardware-software co-designs [181, 182], imaging optics and post-processing algorithm are jointly optimized, requiring the design model to be numerically compatible with custom optimization schemes such as back-propagation [183]. Also, a design engine could be employed in reverse in the concept of computational metrolology [184], requiring the merit function to be regularized for robustness, as demonstrated

in self-calibration deflectometry [185, 186]. Such features are not supported or computationally configurable in current design software. To partially tackle these challenges, gradient-based techniques were proposed [187] using automatic differentiation [188], which is the basic technique in machine learning for network training. This approach enables all the parameters in a physical system to be differentiable, and hence could be optimized by derivative-based methods such as gradient descent. The additional amount of information about derivatives, is much greater than methods that only consider the forward model solely, providing a searching direction in the parameter space. Combined with a deep neural network, such a differentiable ray tracer could be employed for generating lens designs [189, 190]. Similar trends also appear in other domains for solving inverse problems, such as ptychography [191, 192, 193], phase microscopy [194], and virtual reality headset calibration [195].

These prior works [187, 189], though based on automatic differentiation, are application-oriented, and some of the lens design problems are left unexplored, that require solver efficiency, configurable constraints, freeform and asphere surface parameterization, and photo-realistic product inspection. Sensitivity analysis is yet to be explored. Also, only spherical lens designs were considered. Our work here aims to provide an initial attempt to solve these issues, demonstrated by a broad number of applications, beyond the classical lens design regime.

In this work, we formulate lens design as a general optimization problem as usual, but additionally model the system with gradient information by automatic differentiation, and hence achieve a differentiable ray-tracing engine. Custom techniques are introduced to enable validity and efficiency for gradient computation and inference. Based on the obtained derivatives, advanced algorithms could be developed for specific design applications. Further, we bridge between lens design and real-world simulation by importing the differentiable engine into a graphics renderer, such that photo-realistic images can be synthesized for product inspection. Based on the proposed differentiable ray tracer, several applications are

demonstrated, ranging from classical usage such as design optimization and local sensitivity analysis, to advanced applications such as caustic engineering and real setup misalignment estimation. We believe the potentials and possible application domains shown by such a differentiable engine.

6.2 Differentiable lens design engine

We build a geometrical ray tracing engine to model lens designs. Instead of using paraxial ray tracing, we rely on first principles of ray optics and Snell’s law for strictness, aiming to reproduce reality as faithful as possible. This forward modeling is combined with automatic differentiation to enable gradient computations.

6.2.1 Lens design with automatic differentiation

Optical lens design is the process of optimizing possible design parameters to fulfill a performance expectation. Given a lens prescription, ray tracing over the optical surfaces models the design performance, producing outputs such as spot diagrams. The output of this forward process, however, is not sufficient in the optimization stage, whose purpose is the reverse: changing parameters of the lens prescription to achieve an optimal performance.

Gradient information is helpful for optimization. A lens design engine can benefit from not only ray tracing outputs (*e.g.*, spot diagrams), but also gradients of those outputs. Gradients can be approximated using finite difference, but this approach becomes inefficient when the number of variables are large, despite being inaccurate. Automatic differentiation [188] overcomes these issues, and thus is the basis technique in machine learning for training networks, where derivatives are evaluated at machine precision. In terms of lens design, this spirit is depicted in Figure 6.1. Consider the optical performance of a plano-convex lens when its curvature θ changes. Our goal is to implement a lens design engine that is able to produce spot intersections $\mathbf{p}(\theta)$ and irradiance $I(\theta)$, along with their gradients $\partial\mathbf{p}/\partial\theta$ and $\partial I/\partial\theta$, using automatic differentiation. Custom techniques are introduced

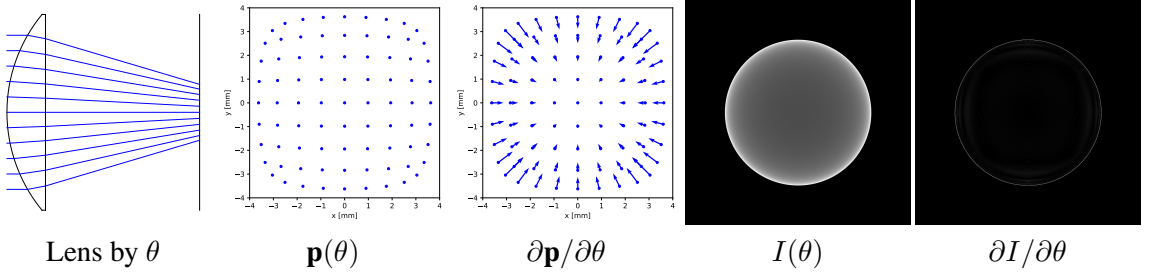


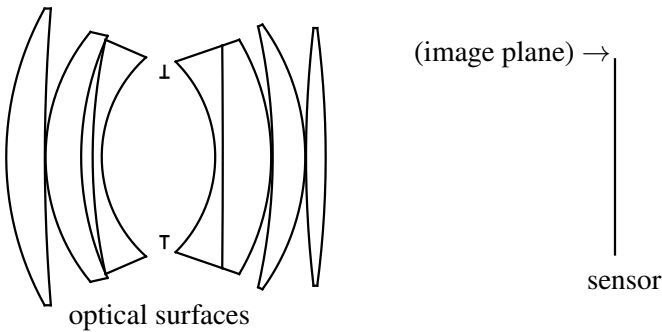
Figure 6.1: A lens parameterized by its first surface curvature θ is under investigation. Using automatic differentiation, our goal is to obtain $p(\theta)$ and $\partial p / \partial \theta$, or $I(\theta)$ and $\partial I / \partial \theta$.

to ensure differentiability and computational efficiency, as will be revealed in this section.

6.2.2 Lens system

We follow the standard lens design pipeline [196, 197] to model the lens systems. We focus on the sequential mode, where starting from one end of the lens system, rays are sequentially traced through a sequence of parameterized optical surfaces (including the image plane, *i.e.*, the sensor plane), intersecting only once for each surface, while traveling towards the other end of the lens system. This is demonstrated in Figure 6.2 with a double-Gauss lens [198]. In the sequential mode, the exact visibility ordering of the surfaces is known a priori, and thus no need for finding the closest surface intersection when performing ray tracing.

\leftarrow (object plane, usually at ∞)



type	distance	radii	diameter	material
O	20	0	100	AIR
S	5.0	78.360	76.0	1.79668/45.5
S	9.8837	469.477	76.0	AIR
S	0.1938	50.297	64.0	1.77279/49.4
S	9.1085	74.376	62.0	AIR
S	2.9457	138.143	60.0	1.6727/32.2
S	2.3256	34.326	51.0	AIR
A	16.0698	0	49.6	OCCULDER
S	13.0	-34.407	48.8	1.74/28.3
S	1.938	-2906.977	57.0	1.77279/49.4
S	12.403	-59.047	60.0	AIR
S	0.3876	-150.890	66.8	1.78797/47.5
S	8.333	-57.890	67.8	AIR
S	0.1938	284.630	66.0	1.78797/47.5
S	5.0388	-253.217	66.0	AIR
I	74.1	0	86.53	AIR

Figure 6.2: Lens system schematic and its prescription file.

Depending on needs, rays can be traced through the lens system in two different modes, *forward mode* or *backward mode*. In forward mode, rays are traced starting from the object plane towards the image plane. This is the preferable way in lens design for aberration

analysis, *e.g.*, generation of spot diagrams. In backward mode, rays are traced in reverse, starting from the image plane towards the object plane. This is a sampling efficient way for sensor image rendering, and thus is the preferable way in computer graphics to render realistic images. We will be using these two modes interchangeably depending on specific needs.

The above two ray tracing procedures are unitedly described as in Algorithm 7: The lens system can be formulated as a “black-box” operator $\mathcal{A}(\cdot)$ that is a function of all lens parameters θ . The lens system \mathcal{A} transforms input ray $\{\mathbf{o}_{\text{in}}, \mathbf{d}_{\text{in}}\}$ into output ray $\{\mathbf{o}_{\text{out}}, \mathbf{d}_{\text{out}}\}$ at wavelength λ :

$$\mathcal{A}(\{\mathbf{o}_{\text{in}}, \mathbf{d}_{\text{in}}\}, \lambda; \theta) = \{\mathbf{o}_{\text{out}}, \mathbf{d}_{\text{out}}\}. \quad (6.1)$$

Ray propagation through a lens system involves two major steps, finding the ray-surface intersection point, and refraction of the ray at material interfaces with chromatic effects, as will be discussed in Subsection 6.2.3. Only valid rays are traced in continuity, whereas invalid rays happen when the intersections are outside of the lens geometry or when total internal reflection takes place.

Algorithm 7: Ray tracing through a lens system \mathcal{A} .

- 1 Initialize and sample a ray $\{\mathbf{o}^{(0)}, \mathbf{d}^{(0)}\} \leftarrow \{\mathbf{o}_{\text{in}}, \mathbf{d}_{\text{in}}\}$ and wavelength λ
 - 2 **for** optical surface f_i ($\forall i = 1, \dots, N$) **do**
 - 3 Find intersection point $\mathbf{o}^{(i)}$
 - 4 Compute refraction direction $\mathbf{d}^{(i)}$
 - 5 **if** valid **then**
 - 6 update ray as $\{\mathbf{o}^{(i)}, \mathbf{d}^{(i)}\}$
 - 7 **end**
 - 8 **end**
 - 9 Return $\{\mathbf{o}_{\text{out}}, \mathbf{d}_{\text{out}}\} \leftarrow \{\mathbf{o}^{(N)}, \mathbf{d}^{(N)}\}$
-

Though in this work we focus on the sequential mode where optical surfaces are fixed in a known order, non-sequential mode should also be possible with proper extensions and modifications on the current ray tracing engine.

6.2.3 Ray tracing engine

Parameterized optical surfaces

We expect the optical surfaces to be model-based and can be fully represented by a small number of differentiable parameters, denoted as θ with a slight abuse of notation. Optical surfaces are described in implicit form:

$$f(x, y, z; \theta) = 0. \quad (6.2)$$

Example surface functions are aspheric surfaces, XY polynomials, and B-splines. Refer to Appendix B for their implicit forms $f(x, y, z; \theta)$ and derivatives $\nabla f(x, y, z; \theta)$.

Memory-efficient differentiable ray-surface intersection

To perform ray tracing from surface to surface, it is necessary to calculate ray-surface intersection, where the problem is to compute a intersection point (x, y, z) and a ray marching distance t for optical surface $f(x, y, z; \theta) = 0$, given a ray $\{\mathbf{o}, \mathbf{d}\}$ of origin $\mathbf{o} = (o_x, o_y, o_z)$ and direction $\mathbf{d} = (d_x, d_y, d_z)$ of unit length. Figure 6.3 illustrates this problem. We would like to find $t > 0$ such that:

$$f(x, y, z; \theta) = f(\mathbf{o} + t\mathbf{d}; \theta) = 0. \quad (6.3)$$

It can be solved using iterative root finders (*e.g.*, Newton's method), unrolling the iterations to construct the computation graph for gradient evaluations, so that the calculated t can be related through the lens parameters θ . However, this straightforward approach is memory consuming because of storing the intermediate iteration variables. We propose to avoid this issue by taking advantage of the fact that solution to Eq. (7.2) is independent on initialization of t , and hence t can be first solved *without* automatic differentiation (no need for storing

intermediate states), then followed by one-step update with automatic differentiation:

$$t \leftarrow t - \frac{f(\mathbf{o} + t\mathbf{d})}{\nabla f \cdot \mathbf{d}}. \quad (6.4)$$

Figure 6.4 shows a comparison against the naïve approach, demonstrating the memory-efficiency advantage of the proposed approach. We employ Newton’s method for obtaining t , initialized by a non-singular estimate $t^{(0)} = (z_f - o_z)/d_z$, with iteration stops when the residual is smaller than tolerance. Convergence of $t^{(k)}$ and $f(\mathbf{o} + t^{(k)}\mathbf{d}; \theta)$ is within a few iterations of k , as in Figure 6.3.

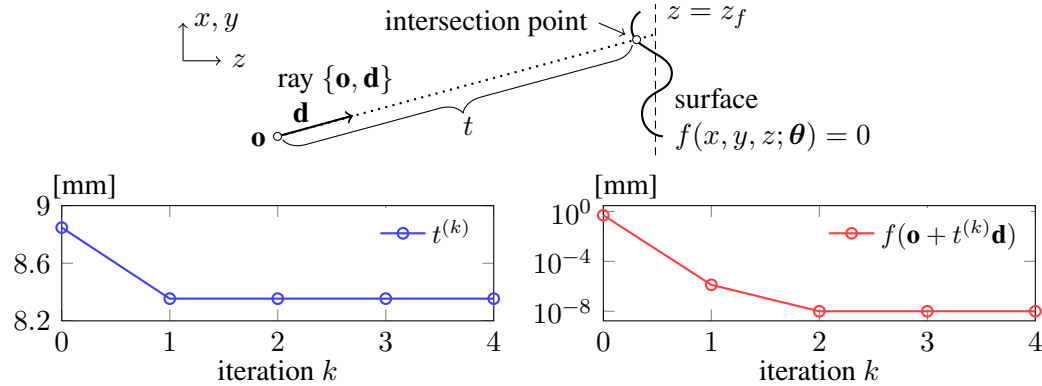


Figure 6.3: Ray-surface intersection is solved as a root-finding problem by Newton’s method. The marching distance t is quickly solved within a few iterations, up to machine precision (single floating point here), at nm scale.

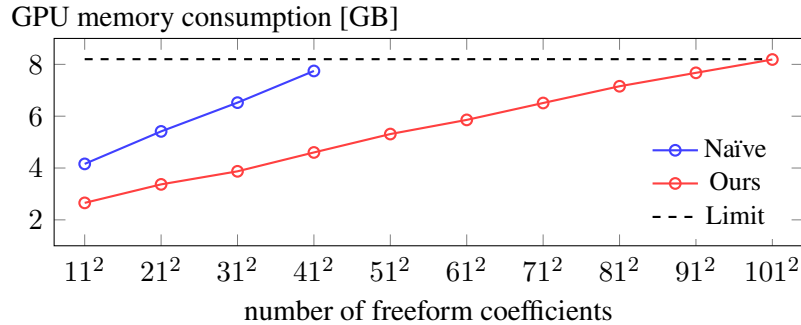


Figure 6.4: Memory consumption comparison between two gradient computation methods. Memory limitation is 8.2 GB.

Refraction and dispersion

At material interfaces, transmitted direction \mathbf{d}_t is determined from surface normal direction $\mathbf{n} = \nabla f / \|\nabla f\|$ and incident direction \mathbf{d}_i , by Snell's law [199]:

$$\mathbf{d}_t = \mathbf{n} \sqrt{1 - (1 - \cos^2 \psi_i) \eta^2} + \eta(\mathbf{d}_i - \mathbf{n} \cos \psi_i), \quad (6.5)$$

where $\cos \psi_i = \mathbf{d}_i \cdot \mathbf{n}$ and $\eta = n_i/n_t$ is the ratio of refraction indices of the two materials. Refractive index follows Cauchy's equation $n(\lambda) = A + B/\lambda^2$, with A and B determined from refractive index $n(\lambda_D)$ at $\lambda_D = 589.3$ nm and Abbe number V :

$$A = n(\lambda_D) - \frac{B}{\lambda_D^2} \quad \text{and} \quad B = \frac{n(\lambda_D) - 1}{V(\lambda_F^{-2} - \lambda_C^{-2})}, \quad (6.6)$$

where $\lambda_F = 486.1$ nm and $\lambda_C = 656.3$ nm.

6.2.4 Image rendering from intersections

Once tracing is done, a synthetic image can be generated given the intersection points (spot diagrams), given a proper integrator $\mathcal{I}(\cdot)$. This process (termed rendering) is handled differently in the two tracing modes.

Reconstruction filter in the forward mode

In the forward tracing mode, performance analysis is conducted to understand the optical property of the current design, where rays are purposely generated according to analysis-specific criteria. This process may involve gradient computations, and differentiability is desired in that the generated image pixel values are differentiable to intersection point movements. To ensure differentiability, $\mathcal{I}(\cdot)$ has to be differentiable. This is demonstrated in Figure 6.5. Though more advanced reconstruction filters could be employed, empirically we found linear filter function yields sufficiently satisfactory results in terms of gradient

computations.

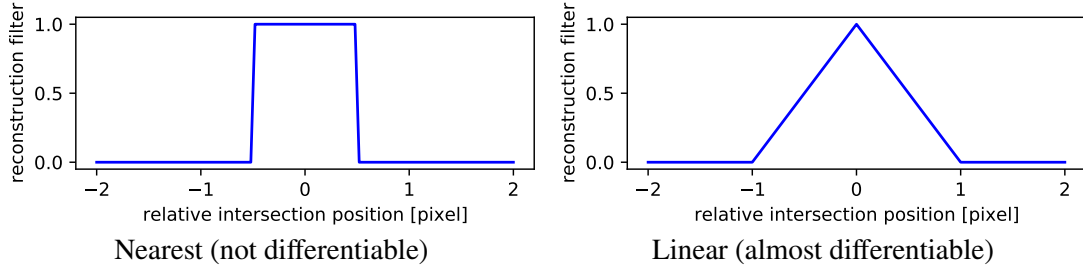


Figure 6.5: Differentiable reconstruction filter $\mathcal{I}(\cdot)$ is crucial for image rendering in the forward tracing mode.

Monte Carlo integrator in the backward mode

In the backward tracing mode, rays are being traced outwards from the sensor plane, and the major goal is to render a physically correct image for the current design given a specific scene. Consider static rendering, at each pixel location \mathbf{x} , with Eq. (6.1), the rendered image $I(\mathbf{x})$ is a continuous integral of ray origin shift $\delta\mathbf{x} \in [-0.5, 0.5]^2$, sample ray direction ω , and wavelength λ :

$$I(\mathbf{x}) = \iiint \mathcal{I}(\mathcal{A}(\{\mathbf{x} + \delta\mathbf{x}, \omega\}, \lambda; \theta)) d\delta\mathbf{x} d\omega d\lambda, \quad (6.7)$$

where $\mathcal{I}(\cdot)$ is now the integration of the rendering equation [200], and is evaluated by renderers using a Monte Carlo integrator for discrete sampling the continuous integral in Eq. (6.7). Thus, our versatile ray tracing engine can be combined with an external graphics renderer to produce photo-realistic images for design production inspection. Figure 6.6 shows an example rendering to compare a plano-convex lens (Thorlabs, AL-2550) against a doublet achromatic lens (Thorlabs, AC254-050), in that chromatic aberration is apparent. This would be helpful for end-users to render photo-realistic images to visually examine design quality.

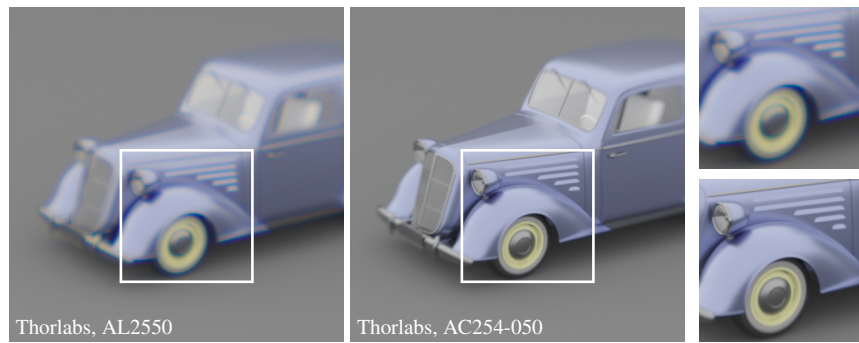


Figure 6.6: Our engine can be imported into a graphics renderer to generate photo-realistic images. A plano-convex lens (AL2550) shows drastic chromatic aberration compared to an achromatic lens (AC254-050).

6.2.5 Implementation

The differentiable engine is implemented based on PyTorch [201], with the external graphics renderer based on Mitsuba2 [202]. To perform ray tracing for a lens system, the entrance pupil has to be determined first, which is the area over the very front lens element where rays from a given viewing angle will finally reach the sensor plane. This is easily determined for paraxial angles, but not for larger angles. Figure 6.7 demonstrates this vignette effect of a double-Gauss design [203], with the calculated entrance pupils shown at different views. Our engine determines the entrance pupil by ray tracing a dense grid (1025×1025) at specific viewing angles. Entrance pupils are determined if the sampled rays propagate through all the optical elements successfully. Exit pupils can be determined in a similar manner as described in [204]. Our engine produces highly identical results to modern lens design software. A sanity check with Zemax [172], using a single wavelength of $\lambda = 587.56\text{ nm}$ at four field of views, as shown in Figure 6.8. The spot diagrams and the RMS errors are almost identical to the Zemax results despite a slight variation due to different aperture sampling strategy.

Our engine produces highly identical results to modern lens design software. To verify this, a double-Gauss design [203] is under sanity check with Zemax [172], using single wavelength $\lambda = 587.56\text{ nm}$ at four field of views, as shown in Figure 6.8. The spot diagrams

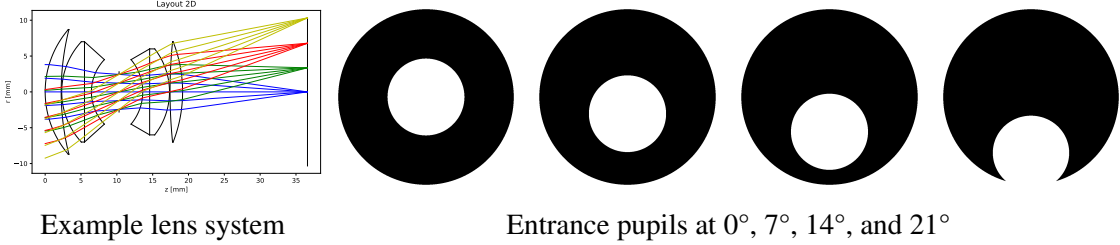


Figure 6.7: Entrance pupil calculation. By tracing a dense grid at the very first optical surface, whose aperture is the dark circle, overlaid on which we can obtain the entrance pupil area (bright region) for subsequent ray spatial sampling, at different viewing angles.

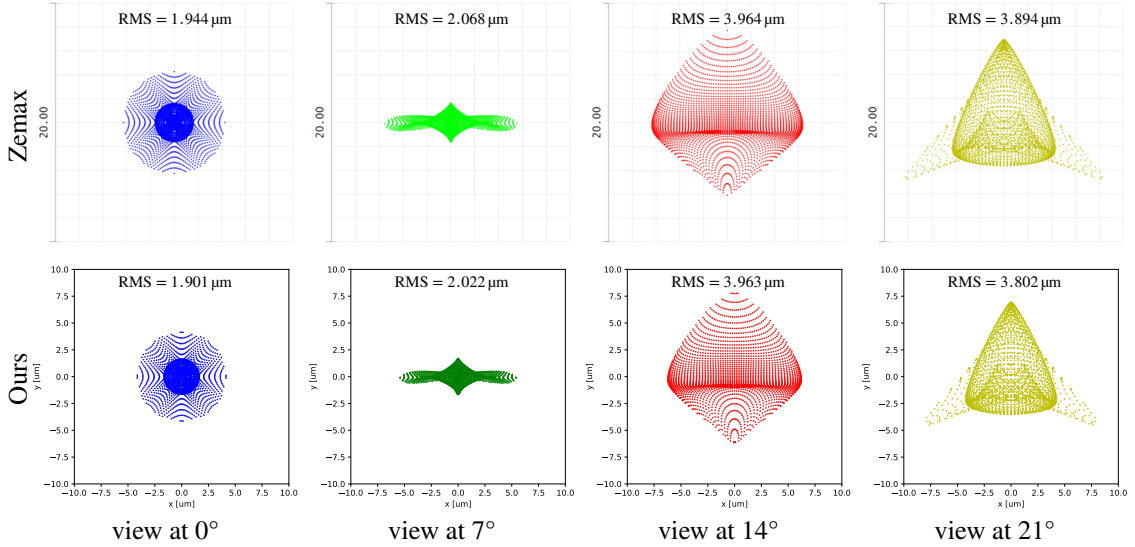


Figure 6.8: Spot diagrams and RMS spot errors that produced by our engine highly resemble those by Zemax.

and the RMS errors are almost identical to the Zemax results despite a slight variation due to different aperture sampling strategy.

6.3 Optimization

To perform design optimization, given an error metric function $g(\cdot)$ (e.g., spot RMS error), the engine finds a set of optimal parameters θ^* that minimizes $\epsilon(\theta)$:

$$\theta^* = \arg \min_{\theta} \epsilon(\theta), \quad \epsilon(\theta) = \sum_{i,j} g(\mathcal{A}(\{\mathbf{o}_i, \mathbf{d}_i\}, \lambda_j; \theta)). \quad (6.8)$$

Scalar-value error function $\epsilon(\cdot)$ is not necessarily linear and can only be evaluated numerically. When the number of variables is small (for example $\boldsymbol{\theta} \in \mathbb{R}^n$, $n < 20$), damped least squares [170] are employed to efficiently optimize Eq. (6.8). When n is large, popular gradient descent methods such as Adam [205] is employed, revealing potentials to be enhanced by machine learning techniques. This optimization flexibility is a feature that differs our engine from existing software.

6.3.1 Unconstrained optimization methods

Gradient descent and variants

Since gradient information is available from automatic differentiation, Eq. (6.8) can be easily optimized using gradient descent methods such as Adam [205], with the learning rate α_k being strategically tuned for each iteration k :

$$\boldsymbol{\theta}^{k+1} \leftarrow \boldsymbol{\theta}^k + \Delta\boldsymbol{\theta}^k, \quad \Delta\boldsymbol{\theta}^k = -\alpha_k \frac{\partial \epsilon}{\partial \boldsymbol{\theta}} \Big|_{\boldsymbol{\theta}=\boldsymbol{\theta}^k}. \quad (6.9)$$

Damped least squares

When $g(\cdot) = \|\cdot\|^2$ and the total number of variables is small, we employ the well-known damped least squares [170, 174] for optimizing Eq. (6.8), re-writing which to simply notations:

$$\boldsymbol{\theta}^* = \arg \min_{\boldsymbol{\theta}} \epsilon(\boldsymbol{\theta}), \quad \epsilon(\boldsymbol{\theta}) = \sum_i \|\mathcal{A}_i(\boldsymbol{\theta})\|^2. \quad (6.10)$$

At each iteration k , the damped least squares method solves for a least squares sub-problem with respect to a small variable change $\Delta\boldsymbol{\theta}$, which is Tikhonov regularized to enhance solution stability, with an iterative changing damping factor ρ_k :

$$\boldsymbol{\theta}^{k+1} \leftarrow \boldsymbol{\theta}^k + \Delta\boldsymbol{\theta}^k, \quad \Delta\boldsymbol{\theta}^k = \arg \min_{\Delta\boldsymbol{\theta}} \sum_i \|\mathcal{A}_i(\boldsymbol{\theta}^k + \Delta\boldsymbol{\theta})\|^2 + \rho_k \|\Delta\boldsymbol{\theta}\|^2. \quad (6.11)$$

By approximating $\mathcal{A}_i(\boldsymbol{\theta}^k + \Delta\boldsymbol{\theta})$ using first-order Taylor expansion:

$$\mathcal{A}_i(\boldsymbol{\theta}^k + \Delta\boldsymbol{\theta}) \approx \mathcal{A}_i(\boldsymbol{\theta}^k) + \mathbf{J}_i \Delta\boldsymbol{\theta}, \quad (6.12)$$

where \mathbf{J}_i is the Jacobian matrix at $\mathcal{A}_i(\boldsymbol{\theta}^k)$, Eq. (6.11) is solved by the normal equation, with \mathbf{I} denoting the identity matrix:

$$\left(\sum_i \mathbf{J}_i^T \mathbf{J}_i + \rho_k \mathbf{I} \right) \Delta\boldsymbol{\theta}^k = - \sum_i \mathbf{J}_i^T \mathcal{A}_i(\boldsymbol{\theta}^k). \quad (6.13)$$

One nice feature of using automatic differentiation is that the right hand side can be efficiently evaluated using back-propagation (the backward mode), with the left hand side being obtained using the forward mode.

6.3.2 Constraint handling

When there are constraints in the design, *e.g.*, positive air-spacing, minimum glass thickness or back focal length, maximum air-spacing overall size, Eq. (6.8) needs to be constrained, which can be re-phrased as two vectors \mathbf{b}_l and \mathbf{b}_h , *i.e.*, a bounding box constraint:

$$\boldsymbol{\theta}^* = \arg \min_{\boldsymbol{\theta}} \epsilon(\boldsymbol{\theta}), \quad \text{s.t.} \quad \mathbf{b}_l \leq \boldsymbol{\theta} \leq \mathbf{b}_h. \quad (6.14)$$

This linear constraint turns the original unconstrained problem into a constrained one, preventing $\partial\epsilon/\partial\boldsymbol{\theta}$ to be evaluated at boundaries. Consequently, the unconstrained optimization methods in the previous subsection are revised by simply projecting the variable to a feasible solution space after obtaining $\Delta\boldsymbol{\theta}^*$ from Eq. (6.9) or Eq. (6.13), at each iteration k applying an element-wise maximum-minimum operation to $\boldsymbol{\theta}^k + \Delta\boldsymbol{\theta}^k$:

$$\boldsymbol{\theta}^{k+1} \leftarrow \text{project}_{[\mathbf{b}_l, \mathbf{b}_h]}(\boldsymbol{\theta}^k + \Delta\boldsymbol{\theta}^k) = \max(\mathbf{b}_l, \min(\boldsymbol{\theta}^k + \Delta\boldsymbol{\theta}^k, \mathbf{b}_h)). \quad (6.15)$$

6.4 Classical applications

The proposed ray tracing engine can manage classical design problems, as will be demonstrated in this section. Spot RMS error at different viewing angles is chosen as the error function $g(\cdot)$ in Eq. (6.8) for design optimization.

6.4.1 Design optimization

Spherical aberration minimization

The first example is to optimize the aspherical coefficients of an asphere lens to minimize the axial spherical aberration. In Figure 6.9, parameters of a well-designed asphere lens (Thorlabs, ACL5040U) are optimized in the hope of further reducing the axial RMS spot. Compared to the initial design, our differentiable engine ends up with a nearly six times smaller RMS spot.

Table 6.1: Differentiable parameters of the aspherical surface.

	radius of curvature [mm]	conic	4^{th} asphere coefficient
Original (initial)	20.9230	-0.6405	2.0e-6
Optimized	20.9403	-0.6262	1.6405e-6

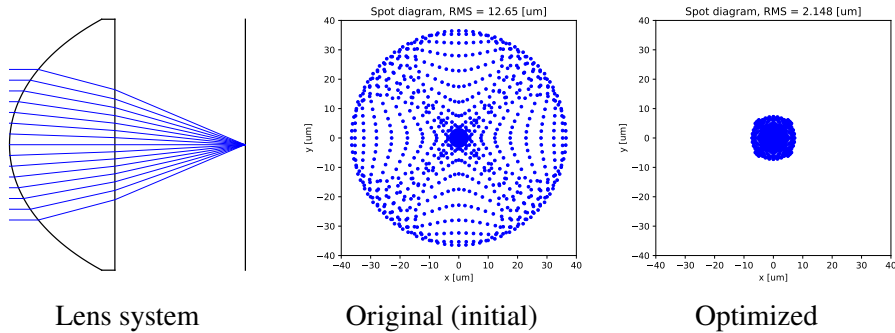


Figure 6.9: Spherical aberration minimization.

Photographic camera design optimization

The engine can also optimize complicated lens group for design optimization. Figure 6.10 shows the second example to re-parameterize curvatures and aspheric coefficients of a Nikon patent design to minimize the total RMS spot error at different field of views (0° , 10° , 20° , 32.45°), at three wavelengths (656.27 nm, 587.56 nm, 486.13 nm). The design is initialized by removing all aspheric coefficients, showing large aberrations. After optimization, our optimized design shows a comparable mean RMS error of the original design. This example demonstrates the capability of our engine to perform multi-lens and asphrehre optimization.

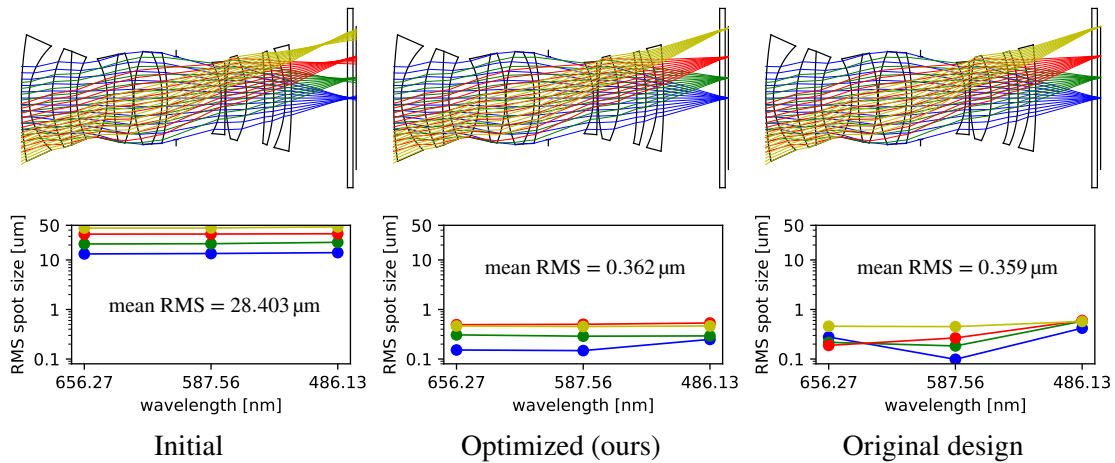


Figure 6.10: Nikon lens group total aberration minimization. Starting from an all-spherical design, with the differentiable parameters θ being all surface curvatures and aspheric coefficients of two surfaces, our optimized version achieves similar performance as the original design.

6.4.2 Tolerance analysis

In tolerancing a lens system, or known as sensitivity analysis, a presuming small, linear parameter perturbation $\Delta\theta$ is enforced, and the total effect of the perturbation, $\Delta\epsilon$, is calculated through the nominal system θ_0 to determine the potential effects. This is mathemati-

cally paraphrased by relating $\Delta\epsilon$ to $\Delta\theta$ through the derivatives:

$$\Delta\epsilon = \frac{\partial\epsilon}{\partial\theta} \cdot \Delta\theta, \quad \text{or in the vector form} \quad \Delta\epsilon = \frac{\partial\epsilon}{\partial\theta} \Delta\theta. \quad (6.16)$$

In forward analysis, $\Delta\theta$ is given to compute $\Delta\epsilon$, whereas in inverse analysis, $\Delta\epsilon$ is given to compute $\Delta\theta$, assuming proper prior probabilities or regularization on $\Delta\theta$. Despite alternative methods such as finite difference, analytical gradients [206], or the wavefront differential method [207], our differentiable engine can automatically evaluate $\partial\epsilon/\partial\theta$ intrinsically, without additional implementation efforts.

In Figure 6.11, a Cooke triplet is under sensitivity analysis, with all optical element positional misalignment parameters θ being tolerated. The proposed automatic differentiation engine can obtain the Jacobian matrix $\partial\epsilon/\partial\theta$ known as the sensitivity matrix for further analysis.

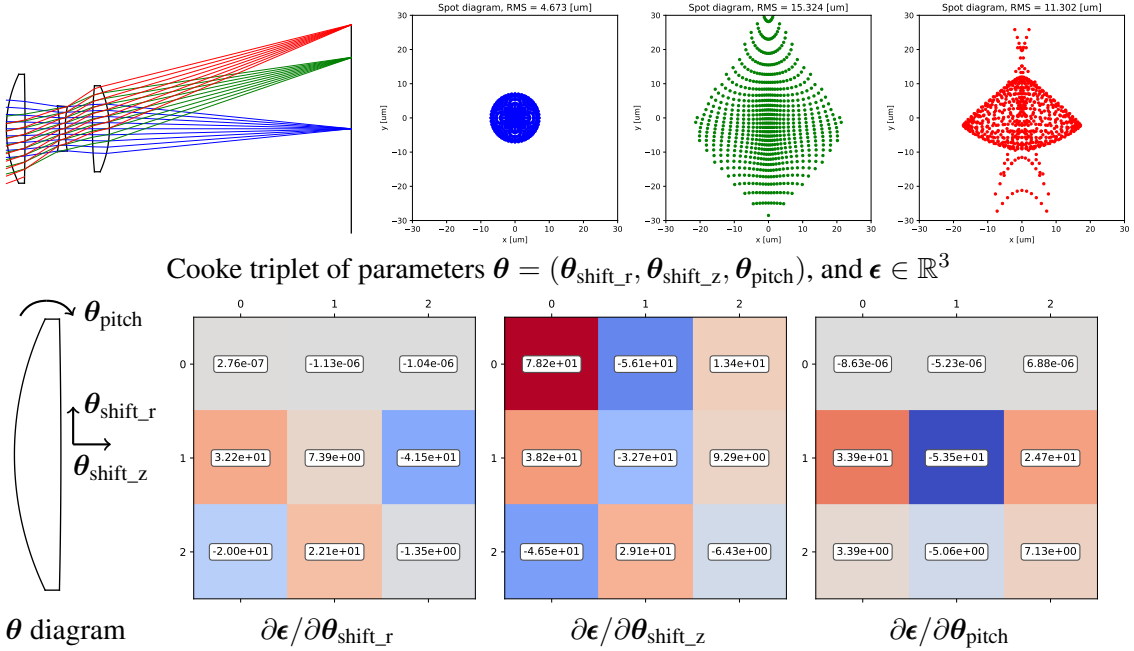


Figure 6.11: Tolerancing a nominal lens system. The sensitivity matrix is readily obtained as the Jacobian matrix.

6.5 Advanced applications

Thanks to differentiability and the versatile optimizer, our engine can be combined with advanced post-processing computational algorithms for complex designs or setup reverse-engineering, and beyond the usual application range of lens design software. Such domain-specific applications are deemed not easily configurable with existing design software, as three examples shown in Figure 6.12.

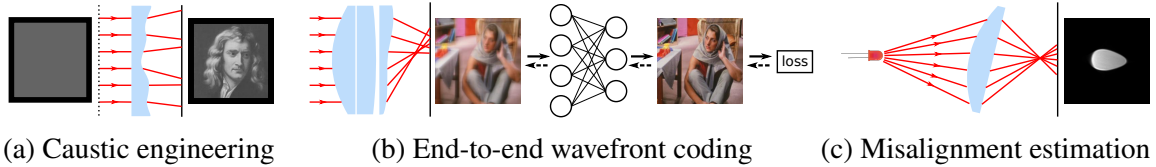


Figure 6.12: Overview of advanced applications. (a) Caustic engineering aims to design a freeform surface to produce a target irradiance pattern at certain distance (Figure 6.13). (b) End-to-end wavefront coding jointly optimizes phase plate design and deconvolution algorithm (here, a neural network) for extended-depth-of-field applications (Figure 6.14). (c) Real setup misalignment can be estimated by using the proposed differentiable engine in reverse as a black-box solver (Figure 6.15).

6.5.1 Caustic engineering

Caustic engineering aims to produce a target image by pixel-wisely changing the directions of a directional light source, by optimizing a freeform optical surface [87, 68]. Here, we demonstrate caustic engineering as one of the applications of our proposed differentiable optical design engine. We employ the forward mode to render caustic images. To enable a satisfactory reconstruction, the desired freeform surface is assumed to be smooth and hence is represented by B-splines with a large degree of freedom approximately equal to the pixel number of the target image. The error metric was the standard Mean Square Error (MSE), and we optimize the B-spline coefficients θ that characterize the freeform surface:

$$\min_{\theta} \|I(\theta) - I_{\text{target}}\|^2. \quad (6.17)$$

Equation (6.17) is optimized using Adam [205] because construction of Jacobian is computationally prohibitive due to the large number of variables in Eq. (6.17). Figure 6.13 shows the results along with intermediate optimization states, where the optimized freeform surface is shown in height maps. The reconstruction image is contrast-preserving, and the optimized freeform surface is smooth. Although in this particular example, the contrast in our result is not high compared to alternative specific solvers, *e.g.*, using optimal transportation [87] or iterative warping [68], our result shows freeform designs would be more approachable when a plug-and-play differentiable ray tracer is available.

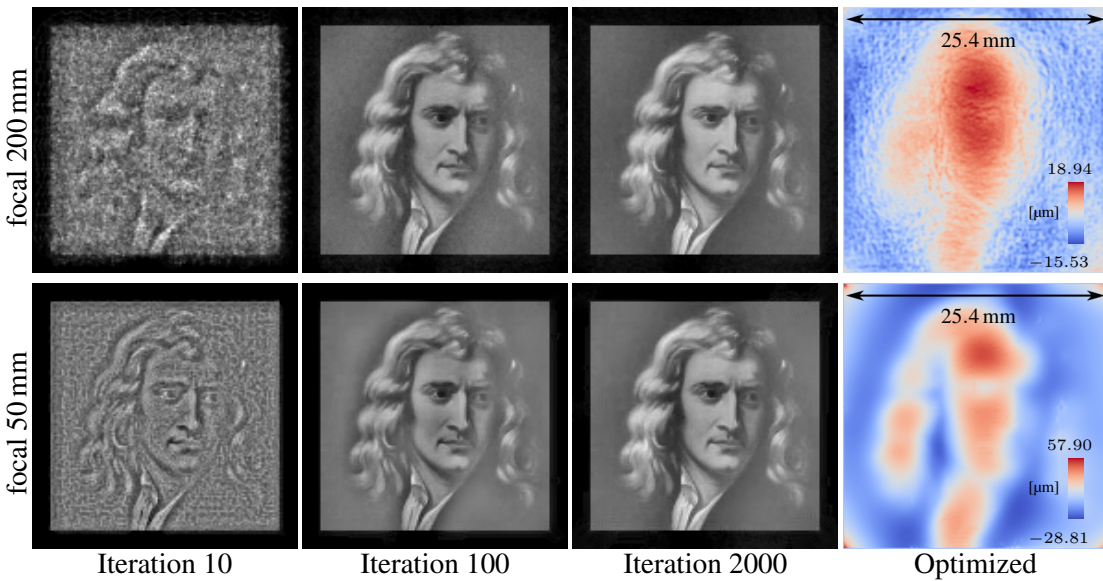


Figure 6.13: Caustic engineering. We optimize a freeform surface to refract collimated light into a target irradiance distribution at two focal lengths, at wavelength 532.8 nm with a refractive index of 1.5. Our engine produces a smooth freeform surface, and optimizes the caustic structures efficiently as shown in the intermediate states.

6.5.2 End-to-end wavefront coding

In wavefront coding, a pupil plane phase modulator is introduced to deliberately distort input lights for PSF engineering, *e.g.*, cubic phase plate [100] that produces depth-invariant PSFs for extended-depth-of-field, and coded aperture [101] and lattice-focal [102] that produce depth-sensitive PSFs for depth retrieval. This process is a joint optical-algorithmic problem

in that the final image is the output from a sequential appliance of the encoding optics and the decoding algorithm. Prior end-to-end approach relies on paraxial approximation [182], ignoring the spatially variant nature of PSFs. Here, our engine provides an initial solution to break this limitation, in that the optical system is faithfully reproduced by ray tracing. We parameterize the phase plate using only third-order XY polynomials, and end-to-end jointly optimize the polynomial coefficients θ_{XY} and U-Net [208] parameters θ_{net} for extended depth of field applications, as in Figure 6.14. Specifically, we aims to minimize a total loss $\mathcal{L}(\theta_{XY}, \theta_{net})$ that consists of an MSE loss \mathcal{L}_{mse} , a total-variation loss \mathcal{L}_{TV} , and a channel feature loss \mathcal{L}_{vgg16} on pre-trained VGG16 [209]:

$$\min_{\theta_{XY}, \theta_{net}} \mathcal{L}(\theta_{XY}, \theta_{net}) = \mathcal{L}_{mse} + \mathcal{L}_{TV} + \mathcal{L}_{vgg16}. \quad (6.18)$$

Initialized from a null zero phase, the optimized phase in Figure 6.14(a) exhibits a similar structure as in [100], verified by the central PSFs in Figure 6.14(b). Given the blurry raw input images, the post-processed images in Figure 6.14(c) reveal sharp features. This example shows the potential of using our differentiable engine for end-to-end joint optimization in computational imaging applications.

6.5.3 Misalignment estimation

Finally, we show real experimental results to leverage potentials of the proposed differentiable pipeline, by using it in reverse to estimate misalignment of an experimental setup. In Figure 6.15(a), a pinpoint light source, consists of an Light-Emitting Diode (LED) (central wavelength 622 nm) and an iris of radius 0.4 mm, is placed far in front of a misaligned plano-convex lens. The lens was able to rotate freely, but the exact angular values were unknown, and the imperfect mounting leads to slight yet noticeable tilting. The setup is imaged by a monochromatic Complementary Metal Oxide Semiconductor (CMOS) sensor (FLIR, GS3-U3-51S5M-C, pixel size of 3.45 μm). Without knowing the exact position and

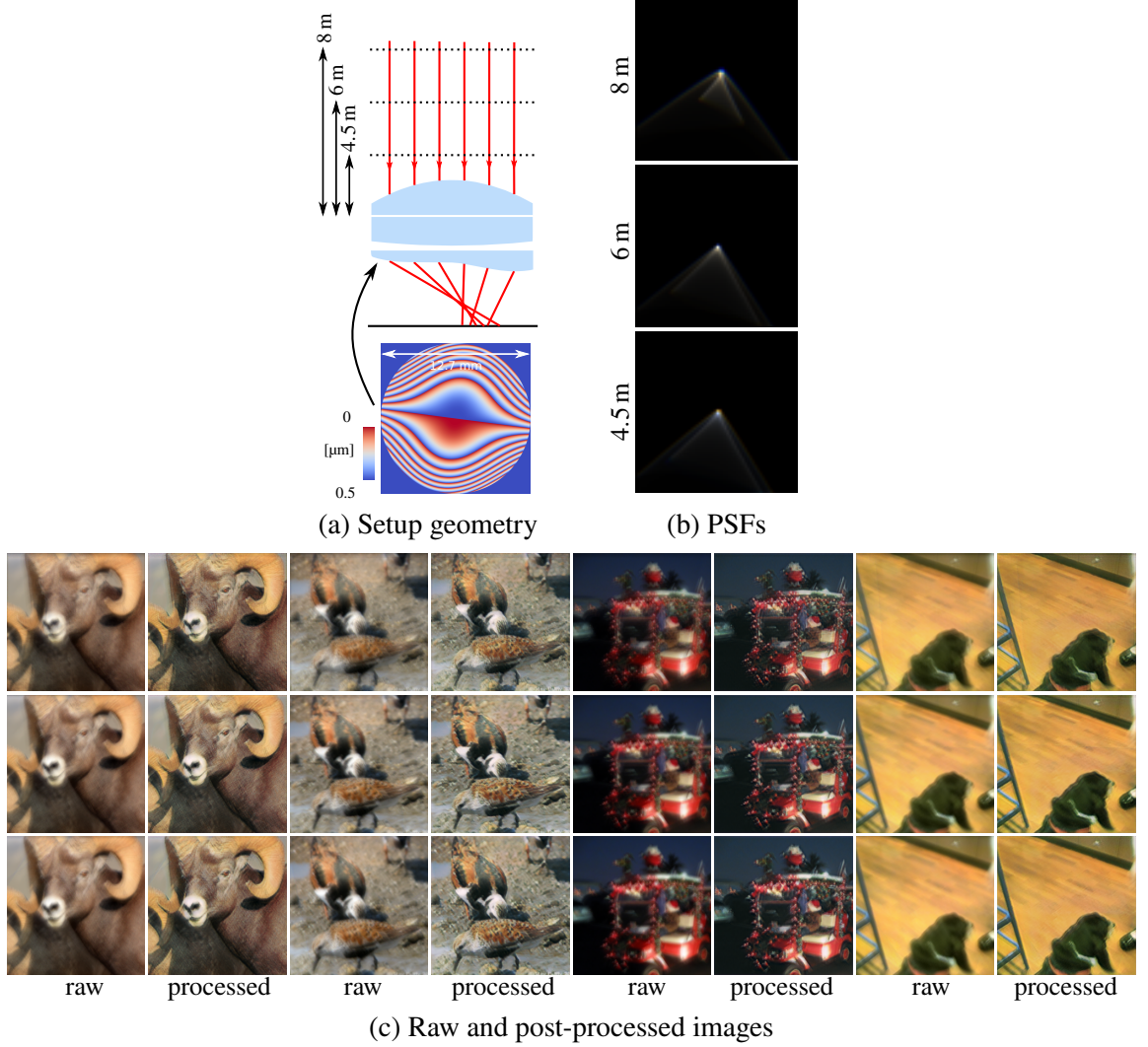


Figure 6.14: Our differentiable engine can perform end-to-end wavefront coding, *i.e.*, jointly optimize phase optics profile and deconvolution algorithm for extended depth of field applications, here by simulation. (a) Setup geometry and optimized phase optics. (b) Central PSFs at different distances. (c) Raw and post-processed images by the neural network.

angle parameters θ , *e.g.*, light source position, sensor to lens distancing, lens yaw/pitch angles, it is very challenging to reproduce experimental measurements by manual parameter tuning a simulation setup. In Figure 6.15, we show the success of our differentiable engine to estimate such misalignment parameters, by minimizing the MSE error between the simulation image $I(\theta)$ and the target real captured image I_{real} . We employ the forward mode to render $I(\theta)$. To escape local stationary points and to regularize gradient computation,

we enforce centroid alignment between the two images, by denoting $\mathcal{C}(\cdot)$ as an operator for calculating image centroid:

$$\min_{\theta} \|I(\theta) - I_{\text{real}}\|^2 + \mu \|\mathcal{C}(I(\theta)) - \mathcal{C}(I_{\text{real}})\|^2, \quad (6.19)$$

where μ is a tradeoff parameter to balance between MSE and alignment errors. Empirically, Eq. (6.19) is optimized by Adam and damped least squares in alternation. The optimization usually takes < 0.5 min to finish for a megapixel image resolution on a GPU (Nvidia, GeForce RTX 2080 Ti).

Two lenses of different focal lengths (Thorlabs, LA1131, focal length of 50 mm; LA1986, focal length of 125 mm) were under investigation, as shown in Figure 6.15(b) and Figure 6.15(c). In Figure 6.15(b), the lens was focused but tilted, and the goal is to re-parameterize the simulation to fit real measurements. In Figure 6.15(c), the lens was slightly de-focused, introducing a blurry bright disk on the sensor plane. With an increase of angular misalignment, the image smears and elongates in the horizontal direction. Initialized from a coarse setup estimation, the final optimized images match real images visually well. This example proves the validity of our forward rendering operator, and demonstrates the possibility of using a differentiable ray tracing engine for setup calibration. The simplicity of using the proposed engine for misalignment estimation allows future self-calibrated applications to be possible for existing solution pipelines. From a broader perspective, we demonstrate the possibility of using a differentiable ray tracer as a general inverse solver for metrology problems.

6.6 Discussion and conclusion

6.6.1 Discussion

In principle, ray optics limits the application range of our differentiable engine in that the wave nature of light is ignored. Resolution demanding imaging applications towards

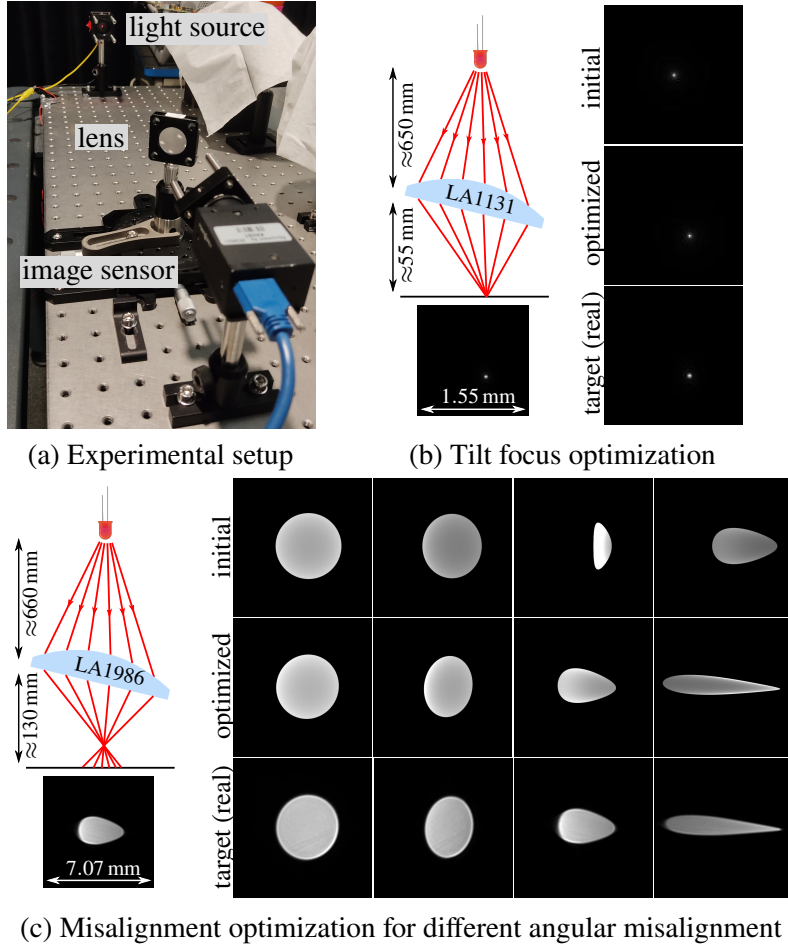


Figure 6.15: Our differentiable engine can be employed as a general-purpose solver to back-engineer real setup misalignment parameters so that simulation and reality match, demonstrated by the high similarity between optimized images and the target (real) ones. (a) Experimental setup includes an LED light source, a lens, and an image sensor. (b) LA1131 was in focus but tilted. (c) LA1986 was out of focus and tilted at the same time. Optimized images share high visual similarity to the real target ones, revealing the success of our approach.

diffraction-limited performance such as telescope or microscope designs are hence not possible at this point. In methodology, we rely on gradient descent and damped least squares as the optimization techniques, and thus a number of iteration steps are required for convergence. Due to its local optimization nature, the solver suffers from the local minima problem and the initialization sensitivity issue. In software, our differentiable tracing engine relies mostly on reverse-mode automatic differentiation, which is known to be memory-consuming especially for large amount of Monte Carlo samples. More memory-efficient

frameworks may be explored. We expect accelerated performance after careful code optimization.

The current ray tracing engine could be further enhanced. From design perspective, more surface representations could be implemented, *e.g.*, Laguerre, Hermite, and Zernike polynomials. New tracing methods are possible, for example paraxial tracing [166] and Gaussian beam tracing [210]. Also, new features could be implemented, *e.g.*, diffraction and gratings, Fresnel equation and polarization ray tracing, coatings, stray light and ghost analysis, and non-sequential tracing. From application perspective, further applications could be explored, *e.g.*, lens metrology [211], realistic lens rendering [212], and wavefront sensor designs [1, 4]. Hardware-software end-to-end optimization for domain-specific applications [181, 182, 213, 214], or semi-supervised training for automatic lens design [189, 190] are also target topics. We believe our framework serves as an initial starting point towards these applications, from a lens design perspective.

6.6.2 Conclusion

To conclude, we have proposed a differentiable ray tracing engine for lens design. Board applications are demonstrated, ranging from classical design optimization and sensitivity analysis, to computationally intensive freeform design, and to challenging experimental misalignment estimation. We envision the potential of such a differentiable ray tracing engine, as it opens up an exciting aspect to bring first-order gradient insights into lens design and relevant problems.

Chapter 7

Differentiable Refractive Deflectometry for Lens Metrology

In this chapter, instead of wavefront design as in Chapter 6, we reverse the purpose and employ the previously proposed differentiable ray tracing engine on a dual-camera deflectometry setup for refractive lens metrology.

Deflectometry, as a non-contact, fully optical metrology method, is challenging to be applied for parameterized refractive elements due to multi-surface entanglement and precise pose alignment. Here, we present a computational self-calibration approach to measure parametric lenses using dual-camera refractive deflectometry. Given the intersection measurements, a differentiable ray tracer models the setup using automatic differentiation, with the unknown lens parameters and its pose optimized by damped least squares. Our approach is able to correctly estimate lens parameters, demonstrated by singlet curvatures and asphere-freeform lens metrology.

7.1 Introduction

Refractive lens metrology plays an important role in lens manufacturing, quality control, and reverse engineering. Various techniques have been proposed for general-purpose freeform optical surface metrology. As a non-interferometry method, deflectometry maintains a strong interest [215] for its simplicity, low-cost, and insensitivity for environments, from specular surface measurement using computerized phase shifting screens [216, 217, 218] to 2D/3D tomography refractive index reconstruction using background oriented Schlieren [12, 13, 219, 3] and variants [14, 1]. However, it is difficult to directly apply phase shifted de-

flectometry to refractive elements, for the following reasons: (i) Multi-surface entanglement that deflection shifts are ambiguous and undetermined for all surfaces; (ii) Sensitive to testing lens alignment that may dominate the actual surface deviation error from nominal design; (iii) Basis representation for freeform surfaces; (iv) High dynamic range. To partially address these issues, there are works demonstrated for multi-surface reconstruction [211, 220], as well as efforts in iterative optimization [221] and with self-calibration [185, 186, 222, 223], pose estimation [224], model-based fitting [225], dual-camera setups [226, 227], and adaptive null testing [228].

This problem of refractive lens testing can be generally rephrased as an inverse problem: Given the metrology measurements (*e.g.*, phase-shifted images, ray intersections, transmitted wavefront maps), estimate a set of unknown parameters characterizing the lens surfaces that fit the measurements reasonably well. Thus, an automated, transparent, controllable data analysis process is desired, as a general-purpose computational solution. Compared to the rapid development of new instruments, computational techniques remain relatively unexplored in the software domain. We believe current metrology techniques could be further improved by advanced computational methods. Inspired by machine learning techniques, gradient-based optimization built on differentiable physical models has found recent success in inverse graphics [229, 202], transparent object reconstruction [230], deep learning automatic lens design by differentiable ray tracing [189, 190], and phase microscopy [194]. By forward modeling the measurements using an automatic differentiation engine [188], a computation graph is constructed, through which the gradients are numerically evaluated. Starting from a proper initial guess, unknown model parameters can be iteratively estimated and updated. This approach can be regarded as a general solution to inverse problems, including refractive deflectometry data analysis, our problem of interest. In this chapter, we introduce differentiable refractive deflectometry, a new computational technique based on automatic differentiation. Our approach is able to perform self-calibrated parameter estimation for multi-surface optical elements. Numerically, we reproduce the physical metrology setup

using a custom-built renderer by realistic ray-tracing all the refractive surfaces by Snell’s law. This physically-accurate ray tracer functions similar to a neuron network, enabling unknown lens parameters and the misalignment pose to be differentiable and their gradients available, enabling optimization by damped least squares [170], a well-appreciated method in lens design. To this goal, we propose techniques to improve ray-surface intersection root finder other than a naïve approach. We believe the proposed framework provides a new and general computational solution to automated data analysis for existing deflectometry techniques.

7.2 Method

The lens metrology process involves hardware image acquisition and software data analysis, as in Figure 7.1. The setup is based on the phase measuring deflectometry [216], but reconfigured in a refractive mode. Figure 7.1(a) shows the schematic diagram. A programmable display screen (Apple MacBook Pro 13.3", pixel pitch 111.8 μm) shows 90° phase-shifted sinusoidal patterns, with the testing lens placed in front of the screen. Two cameras of F-number $f/16$ (FLIR GS3-U3-50S5M, pixel pitch 3.45 μm) are employed to take grayscale images as in Figure 7.1(b). Gamma-correction is applied to ensure a linear relationship between screen and image pixel values. These images are pre-processed using the standard four-step phase shifting method followed by phase unwrapping [231], to retrieve 2D intersections $\hat{\mathbf{p}}_i$ on screen, respectively for both cameras $i = 1, 2$. Testing lens is assumed to be parameterized by θ , with an unknown pose (ϕ, \mathbf{t}) . Possible θ parameterizations are lens curvatures, or freeform coefficients. A differentiable ray tracer numerically reproduces the model setup in Figure 7.1(c), resulting in modeled intersections $\mathbf{p}_i(\theta, \phi, \mathbf{t})$. Given \mathbf{p}_i and $\hat{\mathbf{p}}_i$, a numerical solver in Figure 7.1(d) jointly estimates θ, ϕ, \mathbf{t} such that an error metric (also known as the loss function) is minimized, yielding the metrology values θ^* . Here, we

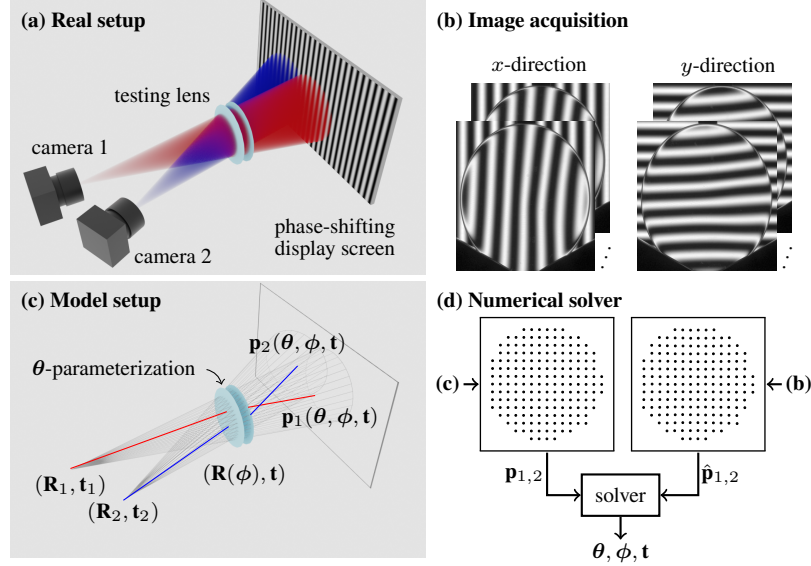


Figure 7.1: Dual-camera refractive deflectometry for lens metrology. **(a)** Hardware setup. **(b)** Captured phase-shifted images, from which on-screen intersections $\hat{\mathbf{p}}_i$ ($i = 1, 2$) are obtained. **(c)** A differentiable ray tracer models the setup by ray tracing each parameterized refractive surface, obtaining the modeled intersections $\mathbf{p}_i(\theta, \phi, \mathbf{t})$. **(d)** Unknown θ and pose (ϕ, \mathbf{t}) are jointly optimized by minimizing the error between \mathbf{p}_i and $\hat{\mathbf{p}}_i$.

minimize the least squared error:

$$\theta^*, \phi^*, \mathbf{t}^* = \arg \min_{\theta, \phi, \mathbf{t}} \sum_{i=1}^2 \|\mathbf{p}_i(\theta, \phi, \mathbf{t}) - \hat{\mathbf{p}}_i\|_2^2. \quad (7.1)$$

We optimize Eq. (7.1) using damped least squares [170], which involves multiple gradient evaluations that are efficiently handled by automatic differentiation. Refer to Section 6.2.3 for details. The following elaborates on computation for $\mathbf{p}_i(\cdot)$, the modeling.

Each object (camera, testing lens) is associated with a rigid transformation (\mathbf{R}, \mathbf{t}) in world coordinate (screen's frame), with a rotation matrix $\mathbf{R} \in \mathbb{R}^{3 \times 3}$ and a translation vector $\mathbf{t} \in \mathbb{R}^3$. Ray tracing is performed in local frames. For pose estimation, the testing lens transformation $(\mathbf{R}(\phi), \mathbf{t})$ can be determined from the six degree-of-freedom parameters (ϕ, \mathbf{t}) where $\phi \in \mathbb{R}^3$ are the rotation angles around (x, y, z) axes.

Cameras are treated as perspective pinholes, with the intrinsic/extrinsic parameters obtained from calibration [232]. Rays are sampled for each image pixel: (i) Starting from

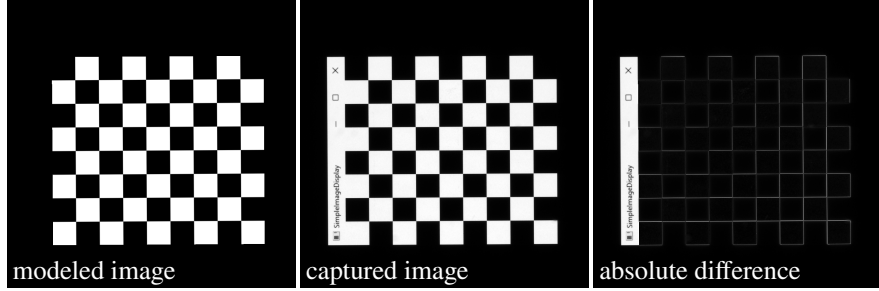


Figure 7.2: Assuming pinhole camera model and planar screen, our ray tracer reproduces real captured images in high fidelity.

camera origins; (ii) Intersecting surfaces of the testing lens via a differentiable root finder, refraction and deflection by Snell’s law, and hence the outgoing rays are associated with lens parameters $\boldsymbol{\theta}$ and pose $(\mathbf{R}(\phi), \mathbf{t})$; (iii) Reaching towards a presumably planar display screen, obtaining the modeled intersections $\mathbf{p}_i(\boldsymbol{\theta}, \phi, \mathbf{t})$ for both cameras. Of these steps, the root finder is the most important to perform ray tracing for asphere or freeform surfaces, in which case there are no closed-form solutions for intersection computation. The intersection problem requires solving for intersection (x, y, z) and a ray marching distance t for optical surface $f(x, y, z; \boldsymbol{\theta}) = 0$, given a ray (\mathbf{o}, \mathbf{d}) of origin $\mathbf{o} = (o_x, o_y, o_z)$ and direction $\mathbf{d} = (d_x, d_y, d_z)$ of unit length. Mathematically:

$$\text{find } t > 0 \quad \text{s.t. } f(x, y, z; \boldsymbol{\theta}) = f(\mathbf{o} + t\mathbf{d}; \boldsymbol{\theta}) = 0. \quad (7.2)$$

Equation (7.2) can be solved using an iterative root finder, with the iterations directly unrolled for gradients, so that ray marching distances t can be related through lens parameters $\boldsymbol{\theta}$ via automatic differentiation. However, this straightforward approach is not efficient and is memory consuming because of storing the intermediate iteration variables. Fortunately, there is an analytic approach for the desired gradient to be computed *outside* of automatic differentiation. Denote the solution to Eq. (7.2) as t^* , and exploit the implicit function theorem for differentiation w.r.t. $\boldsymbol{\theta}$:

$$f(\mathbf{o} + t^*(\boldsymbol{\theta})\mathbf{d}; \boldsymbol{\theta}) = 0 \quad \text{and} \quad (\nabla f \cdot \mathbf{d}) \frac{\partial t^*}{\partial \boldsymbol{\theta}} + \frac{\partial f}{\partial \boldsymbol{\theta}} = 0. \quad (7.3)$$

Rearranging above, yields an analytic formula for gradient:

$$\frac{\partial t^*}{\partial \boldsymbol{\theta}} = -\frac{1}{\nabla f \cdot \mathbf{d}} \frac{\partial f}{\partial \boldsymbol{\theta}}. \quad (7.4)$$

In other words, we can first compute t^* without automatic differentiation (and no intermediate variables stored), and then amend its gradient back to automatic differentiation by Eq. (7.4). We employ Newton's method for obtaining t^* , initialized by a non-singular estimate $t^{(0)} = (z_f - o_z)/d_z$, with iteration stops when the residual is smaller than tolerance. The method converges in a few iterations. When properly setup, with no testing lens present, the modeled image matches the real image reasonably well as in Figure 7.2, demonstrating the physical realism of the ray tracer. Blurry edges are from diffraction, which is ignored in this Chapter, since ray optics is the first principle. Our ray tracer is implemented in PyTorch [201], as the automatic differentiation framework provides a straightforward way to accurately evaluate gradients. For a small set of $\boldsymbol{\theta} \in \mathbb{R}^n$ when $n < 20$, the solver converges in a few seconds on a modern GPU.

Our numerical framework also supports for uncertainty analysis [233], by having the Jacobian matrices \mathbf{J}_i readily obtainable from automatic differentiation. This uncertainty analysis provides us a gauge for robustness data interpretation. We can perform an uncertainty analysis on Eq. (7.1) to understand solution stability. Analyzing the derivatives (ignoring constants):

$$\partial \text{loss} = \sum_{i=1}^2 (\mathbf{p}_i(\boldsymbol{\theta}) - \hat{\mathbf{p}}_i) \cdot \mathbf{J}_i \partial \boldsymbol{\theta} = \mathbf{v} \cdot \partial \boldsymbol{\theta}, \quad \text{where } \mathbf{v} = \sum_{i=1}^2 \mathbf{J}_i^T (\mathbf{p}_i(\boldsymbol{\theta}) - \hat{\mathbf{p}}_i). \quad (7.5)$$

With an independence assumption on $\boldsymbol{\theta} \in \mathbb{R}^n$ (when properly parameterized) and equal prior probabilities, denoting $\text{diag}(\cdot)$ as a diagonal matrix formed by the corresponding vector, the uncertainty variance of each element of variable $\boldsymbol{\theta}$, is hence calculated as:

$$\sigma_{\text{loss}}^2 = \mathbf{v}^T \text{diag}(\sigma_{\boldsymbol{\theta}}^2) \mathbf{v} \quad \Rightarrow \quad \sigma_{\boldsymbol{\theta}}^2 = \frac{\sigma_{\text{loss}}^2}{n|\mathbf{v}|^2}, \quad (7.6)$$

where σ_{loss}^2 can be calculated from the optimal point, and $|\mathbf{v}|^2$ is the element-wise squared of the vector \mathbf{v} .

7.3 Results

7.3.1 Simulation results

Simulation verification are performed to verify the proposed self-calibration method. Figure 7.3 simulates a lens (Thorlabs LE1234) under metrology test for curvature estimation, suffered from a minor misalignment perturbation $\phi = (-0.3^\circ, 0.5^\circ, 0^\circ)$ and $\mathbf{t} = \mathbf{t}_0 + \Delta\mathbf{t}$ where \mathbf{t}_0 is obtained from triangulation but \mathbf{t} is deviated by $\Delta\mathbf{t} = (0.5 \text{ mm}, 0.5 \text{ mm}, 0.5 \text{ mm})$. Synthetic images are corrupted by Gaussian noise. When assuming perfect alignment ($\phi = \mathbf{0}$, $\Delta\mathbf{t} = \mathbf{0}$), the solver fails to predict the correct curvatures, whereas a self-calibration estimation is successful in error reduction. Similar conclusion also holds for freeform metrology, as in Figure 7.4 where an asphere-freeform lens is simulated, suffered from the same misalignment (ϕ, \mathbf{t}), where the task is to estimate the cubic B-spline freeform surface coefficients $\boldsymbol{\theta}$, knowing the asphere profile. This one-surface limitation is necessary to constraint the solution space, in that two arbitrary freeform surfaces can over-fit $\hat{\mathbf{p}}_i$, while being rarely practical in reality. When optimizing only $\boldsymbol{\theta}$, the misalignment affects metrology results. In contrast, a joint optimization of both $\boldsymbol{\theta}$ and (ϕ, \mathbf{t}) significantly reduces the error, showing the benefit of a self-calibration approach.

7.3.2 Experimental results

Experimental results are supportive. Figure 7.5 shows experimental results on lens curvature metrology for a convex-concave lens (Thorlabs LE1234). The lens was amounted and placed in front of the screen at a distance of approximately 5 cm. The testing lens pose $(\phi, \mathbf{t}_0 + \Delta\mathbf{t})$ is assumed to be in perfect angular alignment $\phi = \mathbf{0}$, but suffered from minor displacement errors ($\Delta\mathbf{t} \neq \mathbf{0}$), with the nominal origin \mathbf{t}_0 computed from dual-camera tri-

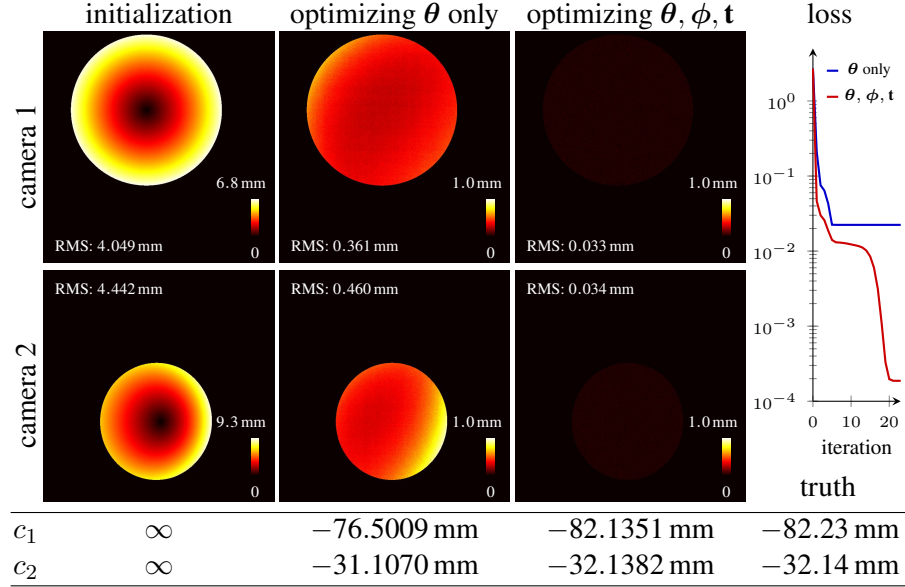


Figure 7.3: Lens curvature $\theta = (c_1, c_2)$ metrology using synthetic data. Intersection error maps $|\mathbf{p}_i - \hat{\mathbf{p}}_i|$ are shown. Metrology data analysis is sensitive to minor misalignment, and a self-calibration approach is preferable by jointly optimizing θ, ϕ, t .

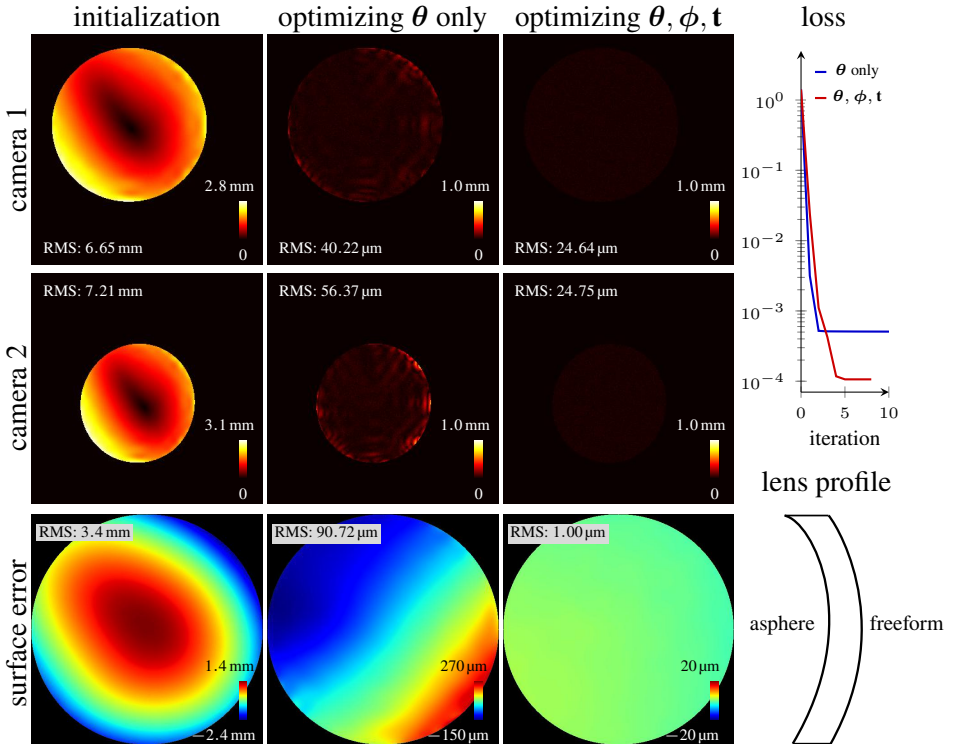


Figure 7.4: Freeform lens metrology using synthetic data. Intersection error maps $|\mathbf{p}_i - \hat{\mathbf{p}}_i|$ and freeform surface error are shown. A self-calibration approach produces better results.

Table 7.1: Experimental singlet lens curvature metrology results.

[mm] / lens name	LA1986	LE1234	LF1822
ours (c_1, c_2)	(62.10, 828.39)	(-82.41, -32.61)	(34.68, 101.41)
truth (c_1, c_2)	(64.38, ∞)	(-82.23, -32.14)	(33.65, 100.00)

angulation. Initialized from planar surfaces ($c_1 = c_2 = \infty$), our optimized curvatures are close to the manufacturer design parameters (Table 7.1), though the fitting error increases slightly at lens boundary. Two other Thorlabs lenses were under the same test, but with both ϕ and $\Delta\mathbf{t}$ optimized. Surface curvatures metrology results are shown in Table 7.1, demonstrating the feasibility of our method to measure multi-surface curvatures. Freeform lens experimental metrology results are also encouraging. The testing optics is an asphere-freeform lens, whose two surfaces were discretely sampled and measured by a Coordinate Measuring Machine (CMM) machine as ground truth. This freeform lens was mounted and placed approximately 5 cm in front of the screen for measurement (see Figure 7.1(b)). Same as in simulation, our assumption is to have the approximate surface profile of the asphere, and would like to solve for the freeform surface, with the pose unknown. Results are shown in Figure 7.6. Our solver optimizes the metrology data to a small residual intersection errors for both cameras, as in Figure 7.6(a). Though wrongly initialized for the asphere surface, the solver optimizes back to the correct orientation, and the reconstruction surfaces are visually similar to the ground truth in Figure 7.6(b), but are spatially transformed due to different alignment in deflectometry experiment and CMM data metrology, and double-surface entanglement as well in that the solution space is too huge to over-fit the data. Yet, our method provides an initial method to qualitatively profile both surfaces, when there is limited prior knowledge available. We have demonstrated the capability of the proposed method for surface metrology, especially for surface curvature estimations.

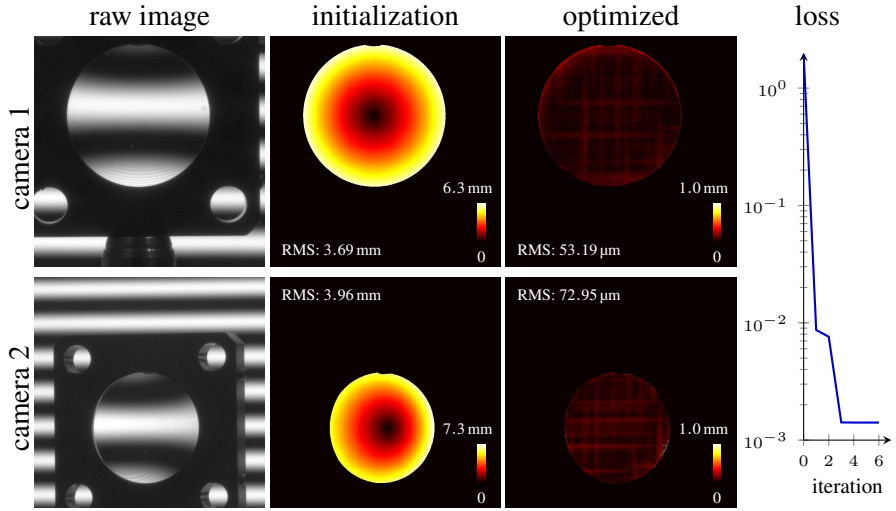


Figure 7.5: Experimental lens curvature metrology for LE1234.

7.4 Discussion and conclusion

Given current results, future investigations are possible for improvements. In hardware, current image acquisition pipeline could be extended to a multi-angle tomography setup, or encode/decode intersections instantaneously to improve acquisition speed [234]. Doublets are also possible by incorporating our technique into existing data fusion model [235]. In software, thanks to automatic differentiation, attainable gradient information allows for a family of solvers to be employed for accelerated convergence, compromising different trade-off factors. Suitable parameterization is also important for a full characterization of optical elements. Lastly, uncertainty analysis deserves more attentions, as deflectometry itself requires a computationally heavy procedure which may introduce data misinterpretation. In conclusion, we have demonstrated differentiable refractive deflectometry for self-calibrated lens metrology. Given the phase-shifting images, a fringe analysis provides measurement intersection points for the method to proceed, where both the unknown lens parameters and the pose are jointly optimized using a differentiable ray tracer. We believe the opened up new computational possibilities for lens metrology data analysis and other relevant application areas.

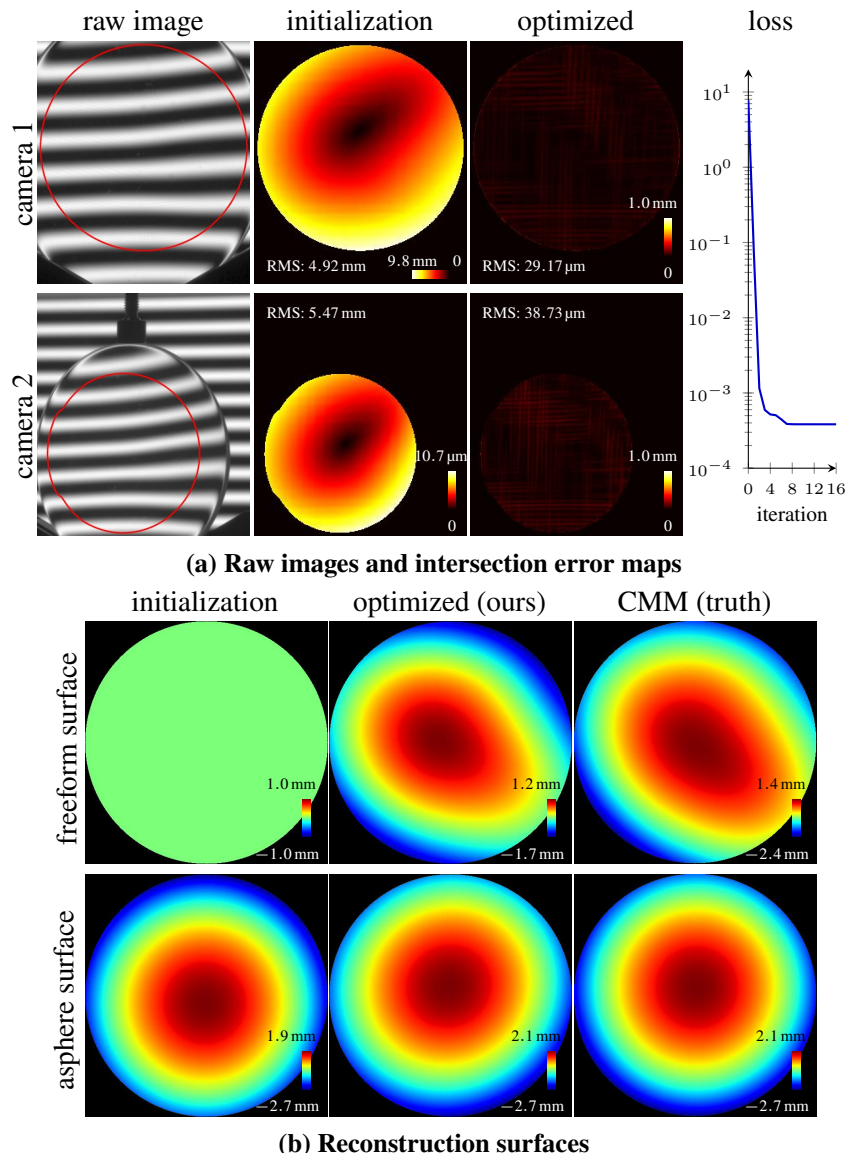


Figure 7.6: Experimental asphere-freeform lens metrology. **(a)** Raw images with the regions of interest (contoured by red lines) and optimization intersection errors. **(b)** Reconstruction comparison against CMM metrology results as ground truth.

Chapter 8

Concluding Remarks

8.1 Summary

Starting with a background introduction in Chapter 2, this dissertation formulates a unified theoretical framework for classical wavefront sensors. Based on which, aiming to maximize the throughput of existing hardware, a new wavefront sensor is proposed in Chapter 3. The wavefront sensor itself is physically implemented by a single binary masked sensor to encode the incoming wavefront, and numerically implemented by an efficient parallelized optimization decoding algorithm on GPU, such that high resolution wavefront acquisition can be achieved in real time. Two specific applications, megapixel adaptive optics in Chapter 4, and single-shot intensity & phase microscopy in Chapter 5, have been demonstrated to show the practical usage of the proposed wavefront sensor.

Inspired by the recent success of learning-based technology, we further propose a differentiable optical ray tracing framework as a general optimization solution to the hardest problems in optics. Specifically, we aim for two applicational situations, lens design in Chapter 6, and metrology in Chapter 7, to show the potentials of this new technique.

8.2 Future work

We may further explore the application range of the proposed wavefront sensor. In hardware, the mask could be further optimized to enable better wavefront frequency acquisition, according to the design rule revealed in this dissertation. In software, the solver could be improved from a deterministic iterative algorithm to a data-driven one, by turning the solver

into a unrolled network trained for optimal convergence performance, or customize and train a deep network as a “black box” solution to the phase retrieval problem behind the scene.

Another direction would be to further explore and develop on the idea of a differentiable ray tracing engine. Currently only geometric optics is considered, whereas wave optics phenomenon is missing, preventing diffractive elements or aperture diffraction to be modeled accurately. These features could be implemented for the proposed differentiable engine to be truly evolving towards a general-purpose optical design engineering software, beyond lens design.

REFERENCES

- [1] Congli Wang, Xiong Dun, Qiang Fu, and Wolfgang Heidrich. Ultra-high resolution coded wavefront sensor. *Optics Express*, 25(12):13736–13746, 2017.
- [2] Congli Wang, Qiang Fu, Xiong Dun, and Wolfgang Heidrich. Megapixel adaptive optics: Towards correcting large-scale distortions in computational cameras. *ACM Transactions on Graphics*, 37(4):115, 2018.
- [3] Congli Wang, Qiang Fu, Xiong Dun, and Wolfgang Heidrich. Quantitative phase and intensity microscopy using snapshot white light wavefront sensing. *Scientific Reports*, 9(1):1–12, 2019.
- [4] Congli Wang, Qiang Fu, Xiong Dun, and Wolfgang Heidrich. Modeling classical wavefront sensors. *Optics Express*, 28(4):5273–5287, 2020.
- [5] Congli Wang, Ni Chen, and Wolfgang Heidrich. DiffLens: A differentiable lens design engine. *Under Submission*, 2021.
- [6] Congli Wang, Ni Chen, and Wolfgang Heidrich. Towards self-calibrated computational lens metrology by differentiable refractive deflectometry. *Under Submission*, 2021.
- [7] Shalin B Mehta and Colin JR Sheppard. Quantitative phase-gradient imaging at high resolution with asymmetric illumination-based differential phase contrast. *Optics Letters*, 34(13):1924–1926, 2009.
- [8] Lei Tian and Laura Waller. Quantitative differential phase contrast imaging in an LED array microscope. *Optics Express*, 23(9):11394–11403, 2015.
- [9] Zachary F Phillips, Michael Chen, and Laura Waller. Single-shot quantitative phase microscopy with color-multiplexed differential phase contrast (cDPC). *PloS One*, 12(2):1–14, 2017.
- [10] Guoan Zheng, Roarke Horstmeyer, and Changhuei Yang. Wide-field, high-resolution Fourier ptychographic microscopy. *Nature Photonics*, 7(9):739–745, 2013.

- [11] Peng Gao, Giancarlo Pedrini, Chao Zuo, and Wolfgang Osten. Phase retrieval using spatially modulated illumination. *Optics Letters*, 39(12):3615–3618, 2014.
- [12] Hugues Richard and Markus Raffel. Principle and applications of the background oriented schlieren (BOS) method. *Measurement Science and Technology*, 12(9):1576–1585, 2001.
- [13] Bradley Atcheson, Ivo Ihrke, Wolfgang Heidrich, Art Tevs, Derek Bradley, Marcus Magnor, and Hans-Peter Seidel. Time-resolved 3D capture of non-stationary gas flows. *ACM Transactions on Graphics*, 27(5):1–9, 2008.
- [14] Gordon Wetzstein, Ramesh Raskar, and Wolfgang Heidrich. Hand-held Schlieren photography with light field probes. In *IEEE International Conference on Computational Photography*, pages 1–8. IEEE, 2011.
- [15] Chao Zuo, Jiasong Sun, Jiaji Li, Jialin Zhang, Anand Asundi, and Qian Chen. High-resolution transport-of-intensity quantitative phase microscopy with annular illumination. *Scientific Reports*, 7(1):7654, 2017.
- [16] Ben C. Platt and Roland Shack. Production and use of a lenticular Hartmann screen. *Journal of the Optical Society of America A*, 61(5):656–660, 1971.
- [17] Jérôme Primot and Nicolas Guérineau. Extended hartmann test based on the pseudoguiding property of a hartmann mask completed by a phase chessboard. *Applied Optics*, 39(31):5715–5720, 2000.
- [18] Roberto Ragazzoni. Pupil plane wavefront sensing with an oscillating prism. *Journal of Modern Optics*, 43(2):289–293, 1996.
- [19] J-C Chanteloup. Multiple-wave lateral shearing interferometry for wave-front sensing. *Applied Optics*, 44(9):1559–1571, 2005.
- [20] Pierre Bon, Guillaume Maucort, Benoit Wattellier, and Serge Monneret. Quadriwave lateral shearing interferometry for quantitative phase microscopy of living cells. *Optics Express*, 17(15):13080–13094, 2009.
- [21] Michael Reed Teague. Deterministic phase retrieval: A Green’s function solution. *Journal of the Optical Society of America A*, 73(11):1434–1441, 1983.
- [22] Francois Roddier. Curvature sensing and compensation: A new concept in adaptive optics. *Applied Optics*, 27(7):1223–1225, 1988.

- [23] Francois Roddier. Wavefront sensing and the irradiance transport equation. *Applied Optics*, 29(10):1402–1403, 1990.
- [24] Percival F Almoro, Laura Waller, Mostafa Agour, Claas Falldorf, Giancarlo Pedrini, Wolfgang Osten, and Steen G Hanson. Enhanced deterministic phase retrieval using a partially developed speckle field. *Optics Letters*, 37(11):2088–2090, 2012.
- [25] Yunhui Zhu, Zhengyun Zhang, and George Barbastathis. Phase imaging for absorptive phase objects using hybrid uniform and structured illumination transport of intensity equation. *Optics Express*, 22(23):28966–28976, 2014.
- [26] Kaye S Morgan, David M Paganin, and Karen KW Siu. Quantitative single-exposure X-ray phase contrast imaging using a single attenuation grid. *Optics Express*, 19(20):19781–19789, 2011.
- [27] Kaye S Morgan, David M Paganin, and Karen KW Siu. X-ray phase imaging with a paper analyzer. *Applied Physics Letters*, 100(12):124102, 2012.
- [28] Sébastien Bérujon, Eric Ziegler, Roberto Cerbino, and Luca Peverini. Two-dimensional X-ray beam phase sensing. *Physical Review Letters*, 108(15):158102, 2012.
- [29] Sébastien Bérujon, Hongchang Wang, Ian Pape, and Kawal Sawhney. X-ray phase microscopy using the speckle tracking technique. *Applied Physics Letters*, 102(15):154105, 2013.
- [30] Pascal Berto, Hervé Rigneault, and Marc Guillon. Wavefront sensing with a thin diffuser. *Optics Letters*, 42(24):5117–5120, 2017.
- [31] Sébastien Bérujon, Hongchang Wang, and Kawal Sawhney. X-ray multimodal imaging using a random-phase object. *Physical Review A*, 86(6):063813, 2012.
- [32] Kaye S Morgan, Peter Modregger, Sarah C Irvine, Simon Rutishauser, Vitaliy A Guzenko, Marco Stampanoni, and Christian David. A sensitive X-ray phase contrast technique for rapid imaging using a single phase grid analyzer. *Optics Letters*, 38(22):4605–4608, 2013.
- [33] Gregory N McKay, Faisal Mahmood, and Nicholas J Durr. Large dynamic range autorefraction with a low-cost diffuser wavefront sensor. *Biomedical Optics Express*, 10(4):1718–1735, 2019.

- [34] Irene Zanette, Tunhe Zhou, Anna Burvall, Ulf Lundström, Daniel H Larsson, M Zdora, P Thibault, F Pfeiffer, and Hans M Hertz. Speckle-based X-ray phase-contrast and dark-field imaging with a laboratory source. *Physical Review Letters*, 112(25):253903, 2014.
- [35] Sébastien Bérujon and Eric Ziegler. Near-field speckle-scanning-based X-ray imaging. *Physical Review A*, 92(1):013837, 2015.
- [36] Xiquan Cui, Jian Ren, Guillermo J Tearney, and Changhuei Yang. Wavefront image sensor chip. *Optics Express*, 18(16):16685–16701, 2010.
- [37] C. David, B. Nöhammer, H. H. Solak, and E. Ziegler. Differential X-ray phase contrast imaging using a shearing interferometer. *Applied Physics Letters*, 81(17):3287–3289, 2002.
- [38] KyeoReh Lee and YongKeun Park. Quantitative phase imaging unit. *Optics Letters*, 39(12):3630–3633, 2014.
- [39] Harold H Wen, Eric E Bennett, Rael Kopace, Ashley F Stein, and Vinay Pai. Single-shot X-ray differential phase-contrast and diffraction imaging using two-dimensional transmission gratings. *Optics Letters*, 35(12):1932–1934, 2010.
- [40] Hongchang Wang, Kawal Sawhney, Sébastien Berujon, Eric Ziegler, Simon Rutishauser, and Christian David. X-ray wavefront characterization using a rotating shearing interferometer technique. *Optics Express*, 19(17):16550–16559, 2011.
- [41] Tong Ling, Dong Liu, Xiumei Yue, Yongying Yang, Yibing Shen, and Jian Bai. Quadriwave lateral shearing interferometer based on a randomly encoded hybrid grating. *Optics Letters*, 40(10):2245–2248, 2015.
- [42] Leslie K. Saddlemyer, Glen Herriot, Jean-Pierre Veran, and J. Murray Fletcher. Design aspects of the reconstructor for the Gemini adaptive optics system (Altair), 1998.
- [43] J Primot and L Sogno. Achromatic three-wave (or more) lateral shearing interferometer. *Journal of the Optical Society of America A*, 12(12):2679–2685, 1995.
- [44] Laura Waller, Lei Tian, and George Barbastathis. Transport of intensity phase-amplitude imaging with higher order intensity derivatives. *Optics Express*, 18(12):12552–12561, 2010.
- [45] Laura Waller, Shan Shan Kou, Colin JR Sheppard, and George Barbastathis. Phase from chromatic aberrations. *Optics Express*, 18(22):22817–22825, 2010.

- [46] Edward H Adelson and James R Bergen. *The plenoptic function and the elements of early vision*, volume 2. Vision and Modeling Group, Media Laboratory, Massachusetts Institute of Technology, 1991.
- [47] Marc Levoy and Pat Hanrahan. Light field rendering. In *Proceedings of the 23rd Annual Conference on Computer Graphics and Interactive Techniques*, pages 31–42, 1996.
- [48] Zhengyun Zhang and Marc Levoy. Wigner distributions and how they relate to the light field. In *IEEE International Conference on Computational Photography*, pages 1–10. IEEE, 2009.
- [49] Ren Ng. Fourier slice photography. *ACM Transactions on Graphics*, 24(3):735–744, 2005.
- [50] Bennett Wilburn, Neel Joshi, Vaibhav Vaish, Eino-Ville Talvala, Emilio Antunez, Adam Barth, Andrew Adams, Mark Horowitz, and Marc Levoy. High performance imaging using large camera arrays. In *ACM SIGGRAPH 2005 Papers*, pages 765–776. 2005.
- [51] Ren Ng and Pat Hanrahan. Light field photography with a hand-held plenoptic camera. *Computer Science Technical Report*, 2(11):1–11, 2005.
- [52] Ashok Veeraraghavan, Ramesh Raskar, Amit Agrawal, Ankit Mohan, and Jack Tumblin. Dappled photography: Mask enhanced cameras for heterodyned light fields and coded aperture refocusing. *ACM Transactions on Graphics*, 26(3):69, 2007.
- [53] Zhimin Xu, Jun Ke, and Edmund Y Lam. High-resolution lightfield photography using two masks. *Optics Express*, 20(10):10971–10983, 2012.
- [54] Kshitij Marwah, Gordon Wetzstein, Yosuke Bando, and Ramesh Raskar. Compressive light field photography using overcomplete dictionaries and optimized projections. *ACM Transactions on Graphics*, 32(4):46, 2013.
- [55] Nicholas Antipa, Sylvia Necula, Ren Ng, and Laura Waller. Single-shot diffuser-encoded light field imaging. In *IEEE International Conference on Computational Photography*, pages 1–11. IEEE, 2016.
- [56] Julian Iseringhausen, Bastian Goldlücke, Nina Pesheva, Stanimir Iliev, Alexander Wender, Martin Fuchs, and Matthias B Hullin. 4D imaging through spray-on optics. *ACM Transactions on Graphics*, 36(4):35, 2017.

- [57] Stephen Boyd, Neal Parikh, Eric Chu, Borja Peleato, and Jonathan Eckstein. Distributed optimization and statistical learning via the alternating direction method of multipliers. *Foundations and Trends in Machine Learning*, 3(1):1–122, 2011.
- [58] Antonin Chambolle and Thomas Pock. A first-order primal-dual algorithm for convex problems with applications to imaging. *Journal of Mathematical Imaging and Vision*, 40(1):120–145, 2011.
- [59] Neal Parikh and Stephen Boyd. Proximal algorithms. *Foundations and Trends in Optimization*, 1(3):127–239, 2014.
- [60] R Tyrell Rockafellar. Augmented lagrangians and applications of the proximal point algorithm in convex programming. *Mathematics of Operations Research*, 1(2):97–116, 1976.
- [61] Ronald E Bruck Jr. An iterative solution of a variational inequality for certain monotone operators in hilbert space. *Bulletin of the American Mathematical Society*, 81(5):890–892, 1975.
- [62] Tom Goldstein and Stanley Osher. The split Bregman method for L1-regularized problems. *SIAM Journal on Imaging Sciences*, 2(2):323–343, 2009.
- [63] Ingrid Daubechies, Michel Defrise, and Christine De Mol. An iterative thresholding algorithm for linear inverse problems with a sparsity constraint. *Communications on Pure and Applied Mathematics*, 57(11):1413–1457, 2004.
- [64] Amir Beck and Marc Teboulle. A fast iterative shrinkage-thresholding algorithm for linear inverse problems. *SIAM Journal on Imaging Sciences*, 2(1):183–202, 2009.
- [65] Donald Geman and Chengda Yang. Nonlinear image recovery with half-quadratic regularization. *IEEE Transactions on Image Processing*, 4(7):932–946, 1995.
- [66] Nikos Komodakis and Jean-Christophe Pesquet. Playing with duality: An overview of recent primal-dual approaches for solving large-scale optimization problems. *IEEE Signal Processing Magazine*, 32(6):31–54, 2015.
- [67] Congli Wang, Qiang Fu, Xiong Dun, and Wolfgang Heidrich. A model for classical wavefront sensors and snapshot incoherent wavefront sensing. In *Computational Optical Sensing and Imaging*, pages CM1A–4. Optical Society of America, 2019.
- [68] Gerwin Damberg and Wolfgang Heidrich. Efficient freeform lens optimization for computational caustic displays. *Optics Express*, 23(8):10224–10232, 2015.

- [69] Claude Roddier and François Roddier. Wave-front reconstruction from defocused images and the testing of ground-based optical telescopes. *Journal of the Optical Society of America A*, 10(11):2277–2287, 1993.
- [70] Timur E Gureyev, David Maurice Paganin, Andrew W Stevenson, Sheridan C Mayo, and SW Wilkins. Generalized eikonal of partially coherent beams and its use in quantitative imaging. *Physical Review Letters*, 93(6):068103, 2004.
- [71] TE Gureyev, A Roberts, and KA Nugent. Partially coherent fields, the transport-of-intensity equation, and phase uniqueness. *Journal of the Optical Society of America A*, 12(9):1942–1946, 1995.
- [72] Timur E Gureyev and Keith A Nugent. Rapid quantitative phase imaging using the transport of intensity equation. *Optics Communications*, 133(1-6):339–346, 1997.
- [73] Shan Shan Kou, Laura Waller, George Barbastathis, and Colin JR Sheppard. Transport-of-intensity approach to differential interference contrast (TI-DIC) microscopy for quantitative phase imaging. *Optics Letters*, 35(3):447–449, 2010.
- [74] Chao Zuo, Qian Chen, Weijuan Qu, and Anand Asundi. High-speed transport-of-intensity phase microscopy with an electrically tunable lens. *Optics Express*, 21(20):24060–24075, 2013.
- [75] Berthold KP Horn and Brian G Schunck. Determining optical flow. *Artificial Intelligence*, 17(1-3):185–203, 1981.
- [76] Joseph W Goodman. *Introduction to Fourier optics*. Roberts and Company Publishers, 2005.
- [77] Kyoji Matsushima and Tomoyoshi Shimobaba. Band-limited angular spectrum method for numerical simulation of free-space propagation in far and near fields. *Optics Express*, 17(22):19662–19673, 2009.
- [78] Jingshan Zhong, Lei Tian, Paroma Varma, and Laura Waller. Nonlinear optimization algorithm for partially coherent phase retrieval and source recovery. *IEEE Transactions on Computational Imaging*, 2(3):310–322, 2016.
- [79] Marco Stockmar, Peter Cloetens, Irene Zanette, Bjoern Enders, Martin Dierolf, Franz Pfeiffer, and Pierre Thibault. Near-field ptychography: Phase retrieval for inline holography using a structured illumination. *Scientific Reports*, 3:1927, 2013.

- [80] Fernando Soldevila, Vicente Durán, Pere Clemente, Jesus Lancis, and Enrique Tjahuerce. Phase imaging by spatial wavefront sampling. *Optica*, 5(2):164–174, 2018.
- [81] Ryoichi Horisaki, Riki Egami, and Jun Tanida. Single-shot phase imaging with randomized light (SPIRaL). *Optics Express*, 24(4):3765–3773, 2016.
- [82] Yicheng Wu, Manoj Kumar Sharma, and Ashok Veeraraghavan. WISH: wavefront imaging sensor with high resolution. *Light: Science & Applications*, 8(1):44, 2019.
- [83] David M Paganin and Kaye S Morgan. X-ray Fokker–Planck equation for paraxial imaging. *Scientific Reports*, 9(1):1–18, 2019.
- [84] Kaye S Morgan and David M Paganin. Applying the Fokker–Planck equation to grating-based X-ray phase and dark-field imaging. *Scientific Reports*, 9(1):1–14, 2019.
- [85] Jean Pierre Guigay. Fourier-transform analysis of Fresnel diffraction patterns and in-line holograms. *Optik*, 49:121–125, 1977.
- [86] Jean Pierre Guigay, Max Langer, Renaud Boistel, and Peter Cloetens. Mixed transfer function and transport of intensity approach for phase retrieval in the fresnel region. *Optics Letters*, 32(12):1617–1619, 2007.
- [87] Yuliy Schwartzburg, Romain Testuz, Andrea Tagliasacchi, and Mark Pauly. High-contrast computational caustic design. *ACM Transactions on Graphics*, 33(4):74, 2014.
- [88] Martin Bawart, Stefan Bernet, and Monika Ritsch-Marte. Programmable freeform optical elements. *Optics Express*, 25(5):4898–4906, 2017.
- [89] Mariana SC Almeida and Mario Figueiredo. Deconvolving images with unknown boundaries using the alternating direction method of multipliers. *IEEE Transactions on Image Processing*, 22(8):3074–3086, 2013.
- [90] Deqing Sun, Stefan Roth, and Michael J Black. Secrets of optical flow estimation and their principles. In *IEEE Conference on Computer Vision and Pattern Recognition*, pages 2432–2439. IEEE, 2010.
- [91] R. G. Lane, A. Glindemann, and J. C. Dainty. Simulation of a Kolmogorov phase screen. *Waves in Random Media*, 2(3):209–224, 1992.

- [92] Bradley Atcheson, Wolfgang Heidrich, and Ivo Ihrke. An evaluation of optical flow algorithms for background oriented schlieren imaging. *Experiments in Fluids*, 46(3):467–476, 2009.
- [93] PN Marsh, D Burns, and JM Girkin. Practical implementation of adaptive optics in multiphoton microscopy. *Optics Express*, 11(10):1123–1130, 2003.
- [94] Jacques M Beckers. Adaptive optics for astronomy: Principles, performance, and applications. *Annual Review of Astronomy and Astrophysics*, 31(1):13–62, 1993.
- [95] T. G. Bifano, J. Perreault, R. Krishnamoorthy Mali, and M. N. Horenstein. Microelectromechanical deformable mirrors. *IEEE Journal of Selected Topics in Quantum Electronics*, 5(1):83–89, 1999.
- [96] Julie A Perreault, Thomas G Bifano, B Martin Levine, and Mark N Horenstein. Adaptive optic correction using microelectromechanical deformable mirrors. *Optical Engineering*, 41(3):561–566, 2002.
- [97] Lijun Zhu, Pang-Chen Sun, Dirk-Uwe Bartsch, William R Freeman, and Yeshaiahu Fainman. Adaptive control of a micromachined continuous-membrane deformable mirror for aberration compensation. *Applied Optics*, 38(1):168–176, 1999.
- [98] Jacques M. Beckers. Increasing the size of the isoplanatic patch with multiconjugate adaptive optics. In *Proc. ESOCW*, volume 30, page 693, 1988.
- [99] E. Diolaiti, R. Ragazzoni, and M. Tordi. Closed loop performance of a layer-oriented multi-conjugate adaptive optics system. *Astronomy & Astrophysics*, 372(2):710–718, 2001.
- [100] Edward R Dowski and W Thomas Cathey. Extended depth of field through wave-front coding. *Applied Optics*, 34(11):1859–1866, 1995.
- [101] Anat Levin, Rob Fergus, Frédo Durand, and William T Freeman. Image and depth from a conventional camera with a coded aperture. *ACM Transactions on Graphics*, 26(3):70, 2007.
- [102] Anat Levin, Samuel W. Hasinoff, Paul Green, Frédo Durand, and William T. Freeman. 4D frequency analysis of computational cameras for depth of field extension. *ACM Transactions on Graphics*, 28(3):97, 2009.

- [103] Oliver Cossairt and Shree Nayar. Spectral focal sweep: Extended depth of field from chromatic aberrations. In *IEEE International Conference on Computational Photography*, pages 1–8. IEEE, 2010.
- [104] Changyin Zhou and Shree Nayar. What are good apertures for defocus deblurring? In *IEEE International Conference on Computational Photography*, pages 1–8. IEEE, 2009.
- [105] Ramesh Raskar, Amit Agrawal, and Jack Tumblin. Coded exposure photography: motion deblurring using fluttered shutter. *ACM Transactions on Graphics*, 25(3):795–804, 2006.
- [106] Anat Levin, Peter Sand, Taeg Sang Cho, Frédo Durand, and William T Freeman. Motion-invariant photography. *ACM Transactions on Graphics*, 27(3):71, 2008.
- [107] Sunghyun Cho, Jue Wang, and Seungyong Lee. Handling outliers in non-blind image deconvolution. In *IEEE International Conference on Computer Vision*, pages 495–502. IEEE, 2011.
- [108] Hui Ji and Kang Wang. Robust image deblurring with an inaccurate blur kernel. *IEEE Transactions on Image Processing*, 21(4):1624–1634, 2012.
- [109] Zhe Hu, Sunghyun Cho, Jue Wang, and Ming-Hsuan Yang. Deblurring low-light images with light streaks. In *IEEE Conference on Computer Vision and Pattern Recognition*, pages 3382–3389. IEEE, 2014.
- [110] Rob Fergus, Barun Singh, Aaron Hertzmann, Sam T Roweis, and William T Freeman. Removing camera shake from a single photograph. *ACM Transactions on Graphics*, 25(3):787–794, 2006.
- [111] Sunghyun Cho and Seungyong Lee. Fast motion deblurring. *ACM Transactions on Graphics*, 28(5):145, 2009.
- [112] Li Xu and Jiaya Jia. Two-phase kernel estimation for robust motion deblurring. In *European Conference on Computer Vision*, pages 157–170. Springer, 2010.
- [113] Dilip Krishnan, Terence Tay, and Rob Fergus. Blind deconvolution using a normalized sparsity measure. In *IEEE Conference on Computer Vision and Pattern Recognition*, pages 233–240. IEEE, 2011.

- [114] Li Xu, Shicheng Zheng, and Jiaya Jia. Unnatural L0 sparse representation for natural image deblurring. In *IEEE Conference on Computer Vision and Pattern Recognition*, pages 1107–1114. IEEE, 2013.
- [115] Jinshan Pan, Deqing Sun, Hanspeter Pfister, and Ming-Hsuan Yang. Blind image deblurring using dark channel prior. In *IEEE Conference on Computer Vision and Pattern Recognition*, pages 1628–1636. IEEE, 2016.
- [116] Jiangxin Dong, Jinshan Pan, Zhixun Su, and Ming-Hsuan Yang. Blind image deblurring with outlier handling. In *IEEE Conference on Computer Vision and Pattern Recognition*, pages 2478–2486. IEEE, 2017.
- [117] Junzhong Liang, David R Williams, and Donald T Miller. Supernormal vision and high-resolution retinal imaging through adaptive optics. *Journal of the Optical Society of America A*, 14(11):2884–2892, 1997.
- [118] Enrique J Fernández, Ignacio Iglesias, and Pablo Artal. Closed-loop adaptive optics in the human eye. *Optics Letters*, 26(10):746–748, 2001.
- [119] Austin Roorda, Fernando Romero-Borja, William J Donnelly III, Hope Queener, Thomas J Hebert, and Melanie CW Campbell. Adaptive optics scanning laser ophthalmoscopy. *Optics Express*, 10(9):405–412, 2002.
- [120] Na Ji, Daniel E Milkie, and Eric Betzig. Adaptive optics via pupil segmentation for high-resolution imaging in biological tissues. *Nature Methods*, 7(2):141–147, 2010.
- [121] Martin J Booth. Adaptive optical microscopy: The ongoing quest for a perfect image. *Light: Science & Applications*, 3(4):e165, 2014.
- [122] B Hermann, EJ Fernández, A Unterhuber, H Sattmann, AF Fercher, W Drexler, PM Prieto, and P Artal. Adaptive-optics ultrahigh-resolution optical coherence tomography. *Optics Letters*, 29(18):2142–2144, 2004.
- [123] Yan Zhang, Barry Cense, Jungtae Rha, Ravi S Jonnal, Weihua Gao, Robert J Zawadzki, John S Werner, Steve Jones, Scot Olivier, and Donald T Miller. High-speed volumetric imaging of cone photoreceptors with adaptive optics spectral-domain optical coherence tomography. *Optics Express*, 14(10):4380–4394, 2006.
- [124] Gordon D Love. Wave-front correction and production of Zernike modes with a liquid-crystal spatial light modulator. *Applied Optics*, 36(7):1517–1524, 1997.

- [125] Fernando Vargas-Martin, Pedro M Prieto, and Pablo Artal. Correction of the aberrations in the human eye with a liquid-crystal spatial light modulator: Limits to performance. *Journal of the Optical Society of America A*, 15(9):2552–2562, 1998.
- [126] Lifa Hu, Li Xuan, Yongjun Liu, Zhaoliang Cao, Dayu Li, and Quanquan Mu. Phase-only liquid-crystal spatial light modulator for wave-front correction with high precision. *Optics Express*, 12(26):6403–6409, 2004.
- [127] Chao Li, Mingliang Xia, Quanquan Mu, Baoguang Jiang, Li Xuan, and Zhaoliang Cao. High-precision open-loop adaptive optics system based on LC-SLM. *Optics Express*, 17(13):10774–10781, 2009.
- [128] Thomas Brox, Andrés Bruhn, Nils Papenberg, and Joachim Weickert. High accuracy optical flow estimation based on a theory for warping. In *European Conference on Computer Vision*, pages 25–36. Springer, 2004.
- [129] Mooseok Jang, Haowen Ruan, Haojiang Zhou, Benjamin Judkewitz, and Changhuei Yang. Method for auto-alignment of digital optical phase conjugation systems based on digital propagation. *Optics Express*, 22(12):14054–14071, 2014.
- [130] Libin Sun, Sunghyun Cho, Jue Wang, and James Hays. Edge-based blur kernel estimation using patch priors. In *IEEE International Conference on Computational Photography*, pages 1–8. IEEE, 2013.
- [131] Tomer Michaeli and Michal Irani. Blind deblurring using internal patch recurrence. In *European Conference on Computer Vision*, pages 783–798. Springer, 2014.
- [132] Enrico Marchetti, Roland Brast, Bernard Delabre, Rob Donaldson, Enrico Fedrigo, Christoph Frank, Norbert Hubin, Johann Kolb, Jean-Louis Lizon, Massimiliano Marchesi, Sylvain Oberti, Roland Reiss, Christian Soenke, Sébastien Tordo, Andrea Baruffolo, Paolo Bagnara, Antonio Amorim, and Jorge Lima. On-sky testing of the multi-conjugate adaptive optics demonstrator. *The Messenger*, 129(8), 2008.
- [133] Frits Zernike. How I discovered phase contrast. *Science*, 121(3141):345–349, 1955.
- [134] G. Nomarski and A. R. Weill. Application à la métallographie des méthodes interférentielles à deux ondes polarisées. *Rev. Met. Paris*, 52:121–134, 1955.
- [135] Gabriel Popescu. *Quantitative phase imaging of cells and tissues*. McGraw Hill Professional, 2011.

- [136] KA Nugent, TE Gureyev, DF Cookson, D Paganin, and Z Barnea. Quantitative phase imaging using hard x rays. *Physical Review Letters*, 77(14):2961, 1996.
- [137] Chao Zuo, Qian Chen, Weijuan Qu, and Anand Asundi. Noninterferometric single-shot quantitative phase microscopy. *Optics Letters*, 38(18):3538–3541, 2013.
- [138] Tong Zhang and Ichiro Yamaguchi. Three-dimensional microscopy with phase-shifting digital holography. *Optics Letters*, 23(15):1221–1223, 1998.
- [139] Wolfgang Osten, Ahmad Faridian, Peng Gao, Klaus Körner, Dinesh Naik, Giancarlo Pedrini, Alok Kumar Singh, Mitsuo Takeda, and Marc Wilke. Recent advances in digital holography. *Applied Optics*, 53(27):G44–G63, 2014.
- [140] Thomas Kreis. Digital holographic interference-phase measurement using the Fourier-transform method. *Journal of the Optical Society of America A*, 3(6):847–855, 1986.
- [141] Etienne Cuche, Pierre Marquet, and Christian Depeursinge. Spatial filtering for zero-order and twin-image elimination in digital off-axis holography. *Applied Optics*, 39(23):4070–4075, 2000.
- [142] Natan T Shaked. Quantitative phase microscopy of biological samples using a portable interferometer. *Optics Letters*, 37(11):2016–2018, 2012.
- [143] Pinhas Girshovitz and Natan T Shaked. Compact and portable low-coherence interferometer with off-axis geometry for quantitative phase microscopy and nanoscopy. *Optics Express*, 21(5):5701–5714, 2013.
- [144] Vani Chhaniwal, Amardeep SG Singh, Rainer A Leitgeb, Bahram Javidi, and Arun Anand. Quantitative phase-contrast imaging with compact digital holographic microscope employing Lloyd’s mirror. *Optics Letters*, 37(24):5127–5129, 2012.
- [145] Zhuo Wang, Larry Millet, Mustafa Mir, Huafeng Ding, Sakulsuk Unarunotai, John Rogers, Martha U Gillette, and Gabriel Popescu. Spatial light interference microscopy (SLIM). *Optics Express*, 19(2):1016–1026, 2011.
- [146] Gabriel Popescu, Takahiro Ikeda, Ramachandra R Dasari, and Michael S Feld. Diffraction phase microscopy for quantifying cell structure and dynamics. *Optics Letters*, 31(6):775–777, 2006.

- [147] Katherine Creath and Goldie Goldstein. Dynamic quantitative phase imaging for biological objects using a pixelated phase mask. *Biomedical Optics Express*, 3(11):2866–2880, 2012.
- [148] Riki Egami, Ryoichi Horisaki, Lei Tian, and Jun Tanida. Relaxation of mask design for single-shot phase imaging with a coded aperture. *Applied Optics*, 55(8):1830–1837, 2016.
- [149] Andrew M Maiden, John M Rodenburg, and Martin J Humphry. Optical ptychography: A practical implementation with useful resolution. *Optics Letters*, 35(15):2585–2587, 2010.
- [150] Joanne Morrison, Lotta Räty, Poppy Marriott, and Peter O’Toole. Ptychography—a label free, high-contrast imaging technique for live cells using quantitative phase information. *Scientific Reports*, 3:2369, 2013.
- [151] Xiaoze Ou, Roarke Horstmeyer, Changhuei Yang, and Guoan Zheng. Quantitative phase imaging via Fourier ptychographic microscopy. *Optics Letters*, 38(22):4845–4848, 2013.
- [152] Timm Weitkamp, Ana Diaz, Christian David, Franz Pfeiffer, Marco Stampanoni, Peter Cloetens, and Eric Ziegler. X-ray phase imaging with a grating interferometer. *Optics Express*, 13(16):6296–6304, 2005.
- [153] Franz Pfeiffer, Timm Weitkamp, Oliver Bunk, and Christian David. Phase retrieval and differential phase-contrast imaging with low-brilliance X-ray sources. *Nature Physics*, 2(4):258, 2006.
- [154] Pierre Thibault, Martin Dierolf, Andreas Menzel, Oliver Bunk, Christian David, and Franz Pfeiffer. High-resolution scanning X-ray diffraction microscopy. *Science*, 321(5887):379–382, 2008.
- [155] P Modregger, F Scattarella, BR Pinzer, C David, R Bellotti, and M Stampanoni. Imaging the ultrasmall-angle X-ray scattering distribution with grating interferometry. *Physical Review Letters*, 108(4):048101, 2012.
- [156] Leonid I. Rudin, Stanley Osher, and Emad Fatemi. Nonlinear total variation based noise removal algorithms. *Physica D: Nonlinear Phenomena*, 60(1-4):259–268, 1992.

- [157] Pan Bing, Xie Hui-Min, Xu Bo-Qin, and Dai Fu-Long. Performance of sub-pixel registration algorithms in digital image correlation. *Measurement Science and Technology*, 17(6):1615, 2006.
- [158] Bruce D Lucas and Takeo Kanade. An iterative image registration technique with an application to stereo vision. In *Proceedings of Imaging Understanding Workshop*, pages 121–130. Vancouver, British Columbia, 1981.
- [159] Mehdi Asghari-Khiavi, Bayden R. Wood, Adam Mechler, Keith R. Bambery, Donna W. Buckingham, Brian M. Cooke, and Don McNaughton. Correlation of atomic force microscopy and raman micro-spectroscopy to study the effects of ex vivo treatment procedures on human red blood cells. *Analyst*, 135(3):525–530, 2010.
- [160] Franz Pfeiffer, Martin Bech, Oliver Bunk, Philipp Kraft, Eric F Eikenberry, Ch Brönnimann, Christian Grünzweig, and Christian David. Hard-X-ray dark-field imaging using a grating interferometer. *Nature Materials*, 7(2):134, 2008.
- [161] Irene Zanette, Timm Weitkamp, Tilman Donath, Simon Rutishauser, and Christian David. Two-dimensional X-ray grating interferometer. *Physical Review Letters*, 105(24):248102, 2010.
- [162] Felix Heide, Qiang Fu, Yifan Peng, and Wolfgang Heidrich. Encoded diffractive optics for full-spectrum computational imaging. *Scientific Reports*, 6:33543, 2016.
- [163] Yifan Peng, Xiong Dun, Qilin Sun, and Wolfgang Heidrich. Mix-and-match holography. *ACM Transactions on Graphics*, 36(6):191, 2017.
- [164] Hongchang Wang, Sebastien Berujon, Julia Herzen, Robert Atwood, David Laundy, Alexander Hipp, and Kawal Sawhney. X-ray phase contrast tomography by tracking near field speckle. *Scientific Reports*, 5:8762, 2015.
- [165] Guangming Zang, Ramzi Idouchi, Ran Tao, Gilles Lubineau, Peter Wonka, and Wolfgang Heidrich. Space-time tomography for continuously deforming objects. *ACM Transactions on Graphics*, 37(4):100, 2018.
- [166] Robert R Shannon. *The art and science of optical design*. Cambridge University Press, 1997.
- [167] Donald P Feder. Automatic lens design methods. *Journal of the Optical Society of America*, 47(10):902–912, 1957.

- [168] Donald P Feder. Automatic optical design. *Applied Optics*, 2(12):1209–1226, 1963.
- [169] C.G. Wynne and P.M.J.H. Wormell. Lens design by computer. *Applied Optics*, 2(12):1233–1238, 1963.
- [170] Joseph Meiron. Damped least-squares method for automatic lens design. *Journal of the Optical Society of America*, 55(9):1105–1109, 1965.
- [171] Joseph Meiron. Automatic lens design by the least squares method. *Journal of the Optical Society of America*, 49(3):293–298, 1959.
- [172] Zemax. Zemax OpticStudio. <https://www.zemax.com/>. 2013.
- [173] Synopsys, Inc. Code V. <https://www.synopsys.com>.
- [174] Michael J Kidger. Use of the levenberg-marquardt (damped least-squares) optimization method in lens design. *Optical Engineering*, 32(8):1731–1739, 1993.
- [175] Jorge Nocedal and Stephen Wright. *Numerical optimization*. Springer Science & Business Media, 2006.
- [176] Jannick P Rolland, Matthew A Davies, Thomas J Suleski, Chris Evans, Aaron Bauer, John C Lambropoulos, and Konstantinos Falaggis. Freeform optics for imaging. *Optica*, 8(2):161–176, 2021.
- [177] William A Parkyn. Design of illumination lenses via extrinsic differential geometry. In *Illumination and Source Engineering*, volume 3428, pages 154–162. International Society for Optics and Photonics, 1998.
- [178] Harald Ries and Julius Muschaweck. Tailored freeform optical surfaces. *Journal of the Optical Society of America A*, 19(3):590–595, 2002.
- [179] Florian R Fournier, William J Cassarly, and Jannick P Rolland. Fast freeform reflector generation using source-target maps. *Optics Express*, 18(5):5295–5304, 2010.
- [180] Yi Luo, Zexin Feng, Yanjun Han, and Hongtao Li. Design of compact and smooth free-form optical system with uniform illuminance for led source. *Optics Express*, 18(9):9055–9063, 2010.
- [181] M Dirk Robinson and David G Stork. Joint design of lens systems and digital image processing. In *International Optical Design Conference*, page WB4. Optical Society of America, 2006.

- [182] Vincent Sitzmann, Steven Diamond, Yifan Peng, Xiong Dun, Stephen Boyd, Wolfgang Heidrich, Felix Heide, and Gordon Wetzstein. End-to-end optimization of optics and image processing for achromatic extended depth of field and super-resolution imaging. *ACM Transactions on Graphics*, 37(4):1–13, 2018.
- [183] Yann LeCun. A theoretical framework for back-propagation. In *Proceedings of the 1988 Connectionist Models Summer School*, volume 1, pages 21–28, 1988.
- [184] Theodore H Hopp. Computational metrology. *Manufacturing Review*, 6:295–295, 1993.
- [185] Evelyn Olesch, Christian Faber, and Gerd Häusler. Deflectometric self-calibration for arbitrary specular surfaces. In *Proc. DGao*, 2011.
- [186] Hongyu Ren, Feng Gao, and Xiangqian Jiang. Iterative optimization calibration method for stereo deflectometry. *Optics Express*, 23(17):22060–22068, 2015.
- [187] Jürgen Werner, Matthias Hillenbrand, Armin Hoffmann, and Stefan Sinzinger. Automatic differentiation in the optimization of imaging optical systems. *Schedae Informaticae*, 21:169–175, 2012.
- [188] Atilim Gunes Baydin, Barak A Pearlmutter, Alexey Andreyevich Radul, and Jeffrey Mark Siskind. Automatic differentiation in machine learning: A survey. *Journal of Machine Learning Research*, 18, 2018.
- [189] Geoffroi Côté, Jean-François Lalonde, and Simon Thibault. Extrapolating from lens design databases using deep learning. *Optics Express*, 27(20):28279–28292, 2019.
- [190] Geoffroi Côté, Jean-François Lalonde, and Simon Thibault. Deep learning-enabled framework for automatic lens design starting point generation. *Optics Express*, 29(3):3841–3854, 2021.
- [191] Sushobhan Ghosh, Youssef SG Nashed, Oliver Cossairt, and Aggelos Katsaggelos. ADP: Automatic differentiation ptychography. In *IEEE International Conference on Computational Photography*, pages 1–10. IEEE, 2018.
- [192] Saugat Kandel, S Maddali, Marc Allain, Stephan O Hruszkewycz, Chris Jacobsen, and Youssef SG Nashed. Using automatic differentiation as a general framework for ptychographic reconstruction. *Optics Express*, 27(13):18653–18672, 2019.

- [193] Ming Du, Saugat Kandel, Junjing Deng, Xiaojing Huang, Arnaud Demortiere, Tuan Tu Nguyen, Remi Tucoulou, Vincent De Andrade, Qiaoling Jin, and Chris Jacobsen. Adorym: A multi-platform generic X-ray image reconstruction framework based on automatic differentiation. *Optics Express*, 29(7):10000–10035, 2021.
- [194] Emrah Bostan, Reinhard Heckel, Michael Chen, Michael Kellman, and Laura Waller. Deep phase decoder: Self-calibrating phase microscopy with an untrained deep neural network. *Optica*, 7(6):559–562, 2020.
- [195] Qi Guo, Huixuan Tang, Aaron Schmitz, Wenqi Zhang, Yang Lou, Alexander Fix, Steven Lovegrove, and Hauke Malte Strasdat. Raycast calibration for augmented reality HMDs with off-axis reflective combiners. In *IEEE International Conference on Computational Photography*, pages 1–12. IEEE, 2020.
- [196] Joseph M Geary. *Introduction to lens design: With practical ZEMAX examples*. Willmann-Bell Richmond, VA, USA:, 2002.
- [197] Craig Kolb, Don Mitchell, and Pat Hanrahan. A realistic camera model for computer graphics. In *Proceedings of the 22nd Annual Conference on Computer Graphics and Interactive Techniques*, pages 317–324, 1995.
- [198] Koichi Wakamiya. Great aperture ratio lens, 1984. U.S. Patent 4448497.
- [199] Max Born and Emil Wolf. *Principles of Optics: 60th Anniversary Edition*. Cambridge University Press, 7 edition, 2019.
- [200] James T Kajiya. The rendering equation. In *Proceedings of the 13th Annual Conference on Computer Graphics and Interactive Techniques*, pages 143–150, 1986.
- [201] Adam Paszke, Sam Gross, Francisco Massa, Adam Lerer, James Bradbury, Gregory Chanan, Trevor Killeen, Zeming Lin, Natalia Gimelshein, Luca Antiga, Alban Desmaison, Andreas Köpf, Edward Yang, Zach DeVito, Martin Raison, Alykhan Tejani, Sasank Chilamkurthy, Benoit Steiner, Lu Fang, Junjie Bai, and Soumith Chintala. PyTorch: An imperative style, high-performance deep learning library. *Advances in Neural Information Processing Systems*, 32:8026–8037, 2019.
- [202] Merlin Nimier-David, Delio Vicini, Tizian Zeltner, and Wenzel Jakob. Mitsuba 2: A retargetable forward and inverse renderer. *ACM Transactions on Graphics*, 38(6):1–17, 2019.

- [203] James G. Baker. Highly corrected objective having two inner divergent meniscus components between collective components, 1949. U.S. Patent 2532751.
- [204] Matt Pharr, Wenzel Jakob, and Greg Humphreys. *Physically based rendering: From theory to implementation*. Morgan Kaufmann, 2016.
- [205] Diederik P. Kingma and Jimmy Ba. Adam: A method for stochastic optimization. In *International Conference on Learning Representations*, 2015.
- [206] M Rimmer. Analysis of perturbed lens systems. *Applied Optics*, 9(3):533–537, 1970.
- [207] Donald P Feder. Differentiation of ray-tracing equations with respect to construction parameters of rotationally symmetric optics. *Journal of the Optical Society of America*, 58(11):1494–1505, 1968.
- [208] Olaf Ronneberger, Philipp Fischer, and Thomas Brox. U-Net: Convolutional networks for biomedical image segmentation. In *International Conference on Medical Image Computing and Computer-Assisted Intervention*, pages 234–241. Springer, 2015.
- [209] Karen Simonyan and Andrew Zisserman. Very deep convolutional networks for large-scale image recognition. In *International Conference on Learning Representations*, 2015.
- [210] Georges A Deschamps. Gaussian beam as a bundle of complex rays. *Electronics Letters*, 7(23):684–685, 1971.
- [211] Daodang Wang, Ping Xu, Zhendong Wu, Xiangyu Fu, Rengmao Wu, Ming Kong, Jian Liang, Bo Zhang, and Rongguang Liang. Simultaneous multisurface measurement of freeform refractive optics based on computer-aided deflectometry. *Optica*, 7(9):1056–1064, 2020.
- [212] Matthias Hullin, Elmar Eisemann, Hans-Peter Seidel, and Sungkil Lee. Physically-based real-time lens flare rendering. *ACM Transactions on Graphics*, 30(4):1–10, 2011.
- [213] Yifan Peng, Qilin Sun, Xiong Dun, Gordon Wetzstein, Wolfgang Heidrich, and Felix Heide. Learned large field-of-view imaging with thin-plate optics. *ACM Transactions on Graphics*, 38(6):1–14, 2019.

- [214] Xiong Dun, Hayato Ikoma, Gordon Wetzstein, Zhanshan Wang, Xinbin Cheng, and Yifan Peng. Learned rotationally symmetric diffractive achromat for full-spectrum computational imaging. *Optica*, 7(8):913–922, 2020.
- [215] Christian Faber, Evelyn Olesch, Roman Krobot, and Gerd Häusler. Deflectometry challenges interferometry: The competition gets tougher! In *Interferometry XVI: Techniques and Analysis*, volume 8493, page 84930R. International Society for Optics and Photonics, 2012.
- [216] Markus C Knauer, Jurgen Kaminski, and Gerd Hausler. Phase measuring deflectometry: A new approach to measure specular free-form surfaces. In *Optical Metrology in Production Engineering*, volume 5457, pages 366–376. International Society for Optics and Photonics, 2004.
- [217] Peng Su, Robert E Parks, Lirong Wang, Roger P Angel, and James H Burge. Software configurable optical test system: A computerized reverse hartmann test. *Applied Optics*, 49(23):4404–4412, 2010.
- [218] Florian Willomitzer, Chia-Kai Yeh, Vikas Gupta, William Spies, Florian Schiffers, Aggelos Katsaggelos, Marc Walton, and Oliver Cossairt. Hand-guided qualitative deflectometry with a mobile device. *Optics Express*, 28(7):9027–9038, 2020.
- [219] Ivo Ihrke, Kiriakos N. Kutulakos, Hendrik P. A. Lensch, Marcus Magnor, and Wolfgang Heidrich. Transparent and specular object reconstruction. In *Computer Graphics Forum*, volume 29, pages 2400–2426. Wiley Online Library, 2010.
- [220] Junqiang Ye, Zhenqi Niu, Xiangchao Zhang, Wei Wang, and Min Xu. Simultaneous measurement of double surfaces of transparent lenses with phase measuring deflectometry. *Optics and Lasers in Engineering*, 137:106356, 2021.
- [221] Logan R Graves, Heejoo Choi, Wenchuan Zhao, Chang Jin Oh, Peng Su, Tianquan Su, and Dae Wook Kim. Model-free deflectometry for freeform optics measurement using an iterative reconstruction technique. *Optics Letters*, 43(9):2110–2113, 2018.
- [222] Yongjia Xu, Feng Gao, Zonghua Zhang, and Xiangqian Jiang. A holistic calibration method with iterative distortion compensation for stereo deflectometry. *Optics and Lasers in Engineering*, 106:111–118, 2018.
- [223] Xueyang Xu, Xiangchao Zhang, Zhenqi Niu, Wei Wang, Yifan Zhu, and Min Xu. Self-calibration of in situ monoscopic deflectometric measurement in precision optical manufacturing. *Optics Express*, 27(5):7523–7536, 2019.

- [224] Chuang Sun, Yamin Zheng, Fa Zeng, Qiao Xue, Wanjun Dai, Wenchuan Zhao, and Lei Huang. Simultaneous measurement of displacement, pitch, and yaw angles of a cavity output mirror based on phase measuring deflectometry. *Applied Optics*, 59(10):3270–3284, 2020.
- [225] Lei Huang, Junpeng Xue, Bo Gao, Chris McPherson, Jacob Beverage, and Mourad Idir. Modal phase measuring deflectometry. *Optics Express*, 24(21):24649–24664, 2016.
- [226] Haolin Zhang, Igors Šics, Jon Ladrera, Marta Llonch, Josep Nicolas, and Juan Campos. Displacement-free stereoscopic phase measuring deflectometry based on phase difference minimization. *Optics Express*, 28(21):31658–31674, 2020.
- [227] Yuk-Ching Leung and Lilong Cai. 3D reconstruction of specular surface by combined binocular vision and zonal wavefront reconstruction. *Applied Optics*, 59(28):8526–8539, 2020.
- [228] Lei Huang, Heejoo Choi, Wenchuan Zhao, Logan R Graves, and Dae Wook Kim. Adaptive interferometric null testing for unknown freeform optics metrology. *Optics Letters*, 41(23):5539–5542, 2016.
- [229] Tzu-Mao Li, Miika Aittala, Frédo Durand, and Jaakko Lehtinen. Differentiable monte carlo ray tracing through edge sampling. *ACM Transactions on Graphics*, 37(6):1–11, 2018.
- [230] Jiahui Lyu, Bojian Wu, Dani Lischinski, Daniel Cohen-Or, and Hui Huang. Differentiable refraction-tracing for mesh reconstruction of transparent objects. *ACM Transactions on Graphics*, 39(6):1–13, 2020.
- [231] Miguel Arevalillo Herráez, David R Burton, Michael J Lalor, and Munther A Gdeisat. Fast two-dimensional phase-unwrapping algorithm based on sorting by reliability following a noncontinuous path. *Applied Optics*, 41(35):7437–7444, 2002.
- [232] Zhengyou Zhang. A flexible new technique for camera calibration. *IEEE Transactions on Pattern Analysis and Machine Intelligence*, 22(11):1330–1334, 2000.
- [233] Hugh W. Coleman and W. Glenn Steele. *Experimentation, validation, and uncertainty analysis for engineers*. John Wiley & Sons, 2018.
- [234] Isaac Trumper, Heejoo Choi, and Dae Wook Kim. Instantaneous phase shifting deflectometry. *Optics Express*, 24(24):27993–28007, 2016.

- [235] Antonín Mikš and Petr Pokorný. Simple method for determination of parameters of cemented doublet. *Applied Optics*, 55(20):5456–5458, 2016.
- [236] Jingfei Ye, Lu Chen, Xinhua Li, Qun Yuan, and Zhishan Gao. Review of optical freeform surface representation technique and its application. *Optical Engineering*, 56(11):110901, 2017.
- [237] Carl de Boor. *A practical guide to splines*, volume 27. Springer-Verlag New York, 1978.

APPENDICES

A Formulas and Derivations

A.1 Diffraction formulas

Rayleigh-Sommerfeld diffraction formula

Let $\mathbf{r} = (x, y)$. Consider in free space a monochromatic scalar field $u_0(\mathbf{r})$ of wavelength λ propagates through a short distance z and becomes $u_z(\mathbf{r})$. These two fields are related through the Rayleigh-Sommerfeld diffraction formula [21, 76]:

$$\text{Spatial domain: } u_z(\mathbf{r}) = \exp \left[jkz \left(1 + \frac{\nabla^2}{k^2} \right)^{1/2} \right] u_0(\mathbf{r}), \quad (\text{A.1})$$

$$\text{Frequency domain: } U_z(\boldsymbol{\rho}) = \exp \left[jkz \left(1 - \lambda^2 |\boldsymbol{\rho}|^2 \right)^{1/2} \right] U_0(\boldsymbol{\rho}), \quad (\text{A.2})$$

where $\boldsymbol{\rho}$ is the Fourier dual of \mathbf{r} , and $U_0(\boldsymbol{\rho})$ and $U_z(\boldsymbol{\rho})$ are Fourier transforms of $u_0(\mathbf{r})$ and $u_z(\mathbf{r})$, respectively. Denote \mathcal{F} as Fourier transform, then $U_0(\boldsymbol{\rho}) = \mathcal{F}\{u_0(\mathbf{r})\}$ and $U_z(\boldsymbol{\rho}) = \mathcal{F}\{u_z(\mathbf{r})\}$. Wave number is $k = 2\pi/\lambda$, and ∇^2 is the Laplacian operator over (x, y) . We follow the convention that $|\cdot|$ denotes the ℓ_2 -norm of a vector, *e.g.*, $|\boldsymbol{\rho}| = (\rho_x^2 + \rho_y^2)^{1/2}$.

Fresnel diffraction formula

The Fresnel diffraction formula can be derived by 1st-order Taylor expansion of the matrix exponential in Eq. (A.1) or the scalar version in Eq. (A.2), that [21]:

$$\left(1 + \frac{\nabla^2}{k^2}\right)^{1/2} \approx 1 + \frac{\nabla^2}{2k^2} \quad \text{or} \quad (1 - \lambda^2|\boldsymbol{\rho}|^2)^{1/2} \approx 1 - \frac{\lambda^2|\boldsymbol{\rho}|^2}{2}, \quad (\text{A.3})$$

under the condition that $\lambda^2|\boldsymbol{\rho}|^2 \ll 1$, or equivalently:

$$\frac{1}{k^2} |\nabla^2 u_0(\mathbf{r})| \ll |u_0(\mathbf{r})|. \quad (\text{A.4})$$

This leads to the Fresnel diffraction formula, with the constant phase $\exp(jkz)$ ignored:

$$\text{Spatial domain: } u_z(\mathbf{r}) = \exp\left(j\frac{z}{2k}\nabla^2\right) u_0(\mathbf{r}), \quad (\text{A.5})$$

$$\text{Frequency domain: } U_z(\boldsymbol{\rho}) = \exp(-j\pi\lambda z|\boldsymbol{\rho}|^2) U_0(\boldsymbol{\rho}). \quad (\text{A.6})$$

Near-field diffraction formula

The Fresnel diffraction formula can be further simplified under the condition of “near-field”, *i.e.* the propagation distance z is small enough so that by another 1st-order Taylor expansion of the matrix exponential in Eq. (A.5), the following approximation holds:

$$\exp\left(j\frac{z}{2k}\nabla^2\right) \approx 1 + j\frac{z}{2k}\nabla^2 \quad \text{or} \quad \exp(-j\pi\lambda z|\boldsymbol{\rho}|^2) \approx 1 - j\pi\lambda z|\boldsymbol{\rho}|^2, \quad (\text{A.7})$$

under the condition that $\pi\lambda z|\boldsymbol{\rho}|^2 \ll 1$, or equivalently:

$$\frac{z}{2k} |\nabla^2 u_0(\mathbf{r})| \ll |u_0(\mathbf{r})|. \quad (\text{A.8})$$

To be compatible with Eq. (A.4), it also requires $1/k^2 \leq z/(2k)$, or:

$$z \geq \lambda/\pi. \quad (\text{A.9})$$

This leads to the near-field diffraction formula:

$$\text{Spatial domain: } u_z(\mathbf{r}) = \left(1 + j\frac{z}{2k} \nabla^2\right) u_0(\mathbf{r}), \quad (\text{A.10})$$

$$\text{Frequency domain: } U_z(\boldsymbol{\rho}) = \left(1 - j\pi\lambda z |\boldsymbol{\rho}|^2\right) U_0(\boldsymbol{\rho}). \quad (\text{A.11})$$

A.2 Wave optics derivations

In the following, small letters denote scalar fields in spatial domain, and capital or calligraphic letters denote scalar fields in Fourier domain, with subscript 0 and z denote the original and diffracted fields, respectively.

We will be using Eq. (A.1) and Eq. (A.2) for total field diffraction (potentially of high frequency), whereas using Eq. (A.10) and Eq. (A.11) for analyzing sample-related diffraction (potentially of low frequency).

Diffraction from optics to sensor

The initial field $u_0(\mathbf{r})$ is a multiplication of general (amplitude or phase) complex transfer function $p_0(\mathbf{r})$ of the optics and a general sample scalar field $f_0(\mathbf{r}) = A(\mathbf{r}) \exp[j\phi(\mathbf{r})]$:

$$u_0(\mathbf{r}) = \underbrace{p_0(\mathbf{r})}_{\text{optics}} \cdot \underbrace{f_0(\mathbf{r})}_{\text{sample}}. \quad (\text{A.12})$$

For diffraction field $u_z(\mathbf{r})$ at distance z , using Eq. (A.1) via expanding the propagation in the Fourier domain, we have [1]:

$$\begin{aligned}
u_z(\mathbf{r}) &\triangleq \exp \left[jkz \left(1 + \frac{\nabla^2}{k^2} \right)^{1/2} \right] u_0(\mathbf{r}) \\
&\stackrel{\mathcal{F}}{=} \int \exp(j2\pi\mathbf{r} \cdot \boldsymbol{\rho}) \exp \left[jkz (1 - \lambda^2 |\boldsymbol{\rho}|^2)^{1/2} \right] \times \int P_0(\boldsymbol{\rho}') F_0(\boldsymbol{\rho} - \boldsymbol{\rho}') d\boldsymbol{\rho}' d\boldsymbol{\rho} \\
&\stackrel{(A.14)}{\approx} \exp(-jkz) \int \exp(j2\pi\mathbf{r} \cdot \boldsymbol{\rho}') \exp \left[jkz (1 - \lambda^2 |\boldsymbol{\rho}'|^2)^{1/2} \right] \times \\
&\quad \int \exp[j2\pi (\mathbf{r} - \lambda z \boldsymbol{\rho}') \cdot \boldsymbol{\rho}''] \exp \left[jkz (1 - \lambda^2 |\boldsymbol{\rho}''|^2)^{1/2} \right] F_0(\boldsymbol{\rho}'') d\boldsymbol{\rho}'' P_0(\boldsymbol{\rho}') d\boldsymbol{\rho}' \\
&= \exp(-jkz) \int \exp(j2\pi\mathbf{r} \cdot \boldsymbol{\rho}') P_z(\boldsymbol{\rho}') \times \left(\int \exp[j2\pi (\mathbf{r} - \lambda z \boldsymbol{\rho}') \cdot \boldsymbol{\rho}''] F_z(\boldsymbol{\rho}'') d\boldsymbol{\rho}'' \right) d\boldsymbol{\rho}' \\
&\stackrel{\mathcal{F}^{-1}}{=} \exp(-jkz) \int \exp(j2\pi\mathbf{r} \cdot \boldsymbol{\rho}') P_z(\boldsymbol{\rho}') f_z(\mathbf{r} - \lambda z \boldsymbol{\rho}') d\boldsymbol{\rho}', \tag{A.13}
\end{aligned}$$

where the third equality of Eq. (A.13) results from the introduction of variable $\boldsymbol{\rho}'' = \boldsymbol{\rho} - \boldsymbol{\rho}'$, and \cdot denotes inner product. The approximation comes from (for $\lambda = 500$ nm and pixel size $\epsilon = 6.45$ μm, at Nyquist frequency $\lambda^2 |\boldsymbol{\rho}|^2 \sim 0.0015 \ll 1$) [21]:

$$(1 - \lambda^2 |\boldsymbol{\rho}|^2)^{1/2} \approx (1 - \lambda^2 |\boldsymbol{\rho}'|^2)^{1/2} + (1 - \lambda^2 |\boldsymbol{\rho}''|^2)^{1/2} - \lambda^2 \boldsymbol{\rho}' \cdot \boldsymbol{\rho}'' - 1. \tag{A.14}$$

To simplify notation, we neglect constant phase, and substitute $\boldsymbol{\rho}'$ with $\boldsymbol{\rho}$ in Eq. (A.13):

$$u_z(\mathbf{r}) = \int \exp(j2\pi\mathbf{r} \cdot \boldsymbol{\rho}) P_z(\boldsymbol{\rho}) f_z(\mathbf{r} - \lambda z \boldsymbol{\rho}) d\boldsymbol{\rho}. \tag{A.15}$$

Notice that Eq. (A.15) is a general formula and is applicable to any field that can be decomposed as $u_0(\mathbf{r}) = p_0(\mathbf{r}) f_0(\mathbf{r})$. We now focus on deriving sample diffraction field $f_z(\mathbf{r} - \lambda z \boldsymbol{\rho})$.

Sample diffraction

Let $g_0(\mathbf{r}) = \exp[j\phi(\mathbf{r})]$, $f_0(\mathbf{r}) = A(\mathbf{r})g_0(\mathbf{r})$ and Eq. (A.15) is applicable to expressing $f_z(\mathbf{r})$:

$$f_z(\mathbf{r}) \stackrel{(A.15)}{=} \int \exp(j2\pi\mathbf{r} \cdot \boldsymbol{\rho}) \mathcal{A}_z(\boldsymbol{\rho}) g_z(\mathbf{r} - \lambda z \boldsymbol{\rho}) d\boldsymbol{\rho}, \quad (A.16)$$

where $\mathcal{A}_z(\boldsymbol{\rho})$ is the Fourier transform of $A_z(\mathbf{r})$, which is the diffraction field of $A(\mathbf{r})$. Assuming near-field for $A(\mathbf{r})$ and $g_0(\mathbf{r})$ respectively, by Eq. (A.10) we have:

$$A_z(\mathbf{r}) \stackrel{(A.10)}{\approx} A(\mathbf{r}) + j\frac{z}{2k} \nabla^2 A(\mathbf{r}) \approx A(\mathbf{r}), \quad (A.17)$$

$$g_z(\mathbf{r}) \stackrel{(A.10)}{\approx} \exp[j\phi(\mathbf{r})] \left(1 - \frac{z}{2k} \nabla^2 \phi(\mathbf{r}) - j\frac{z}{2k} \nabla \phi(\mathbf{r}) \cdot \nabla \phi(\mathbf{r}) \right). \quad (A.18)$$

Since we assume near-field for computing $g_z(\mathbf{r})$, the conditions are, following Eq. (A.8):

$$\frac{z}{2k} |\nabla \phi(\mathbf{r})|^2 \ll 1 \quad \Rightarrow \quad |\nabla \phi(\mathbf{r})| \ll \left(\frac{4\pi}{\lambda z} \right)^{1/2} \stackrel{(A.9)}{\leq} \frac{2\pi}{\lambda}, \quad (A.19)$$

$$\frac{z}{2k} |\nabla^2 \phi(\mathbf{r})| \stackrel{(A.8)}{\ll} 1 \quad \Rightarrow \quad |\nabla^2 \phi(\mathbf{r})| \ll \frac{4\pi}{\lambda z} \sim \frac{2\pi}{\lambda}. \quad (A.20)$$

Notice we have obtained the two identical constraints when deriving Eq. (3.3) in ray optics, justifying the conditions in Chapter 3. For sufficiently small $\lambda z |\boldsymbol{\rho}|$ compared to pixel size ϵ , we have valid 1st-order approximation for $\phi(\mathbf{r} - \lambda z \boldsymbol{\rho})$, and 0th-order approximation for higher orders:

$$\begin{aligned} \phi(\mathbf{r} - \lambda z \boldsymbol{\rho}) &\approx \phi(\mathbf{r}) - \lambda z \boldsymbol{\rho} \cdot \nabla \phi(\mathbf{r}), \\ \nabla \phi(\mathbf{r} - \lambda z \boldsymbol{\rho}) &\approx \nabla \phi(\mathbf{r}), \\ \nabla^2 \phi(\mathbf{r} - \lambda z \boldsymbol{\rho}) &\approx \nabla^2 \phi(\mathbf{r}). \end{aligned} \quad (A.21)$$

By Eq. (A.21), we may obtain $g_z(\mathbf{r} - \lambda z \boldsymbol{\rho})$ from Eq. (A.18), and hence $f_z(\mathbf{r})$ in Eq. (A.16) derives as:

$$\begin{aligned} f_z(\mathbf{r}) &\stackrel{(A.18)}{\approx} \stackrel{(A.21)}{\approx} \left(1 - \frac{z}{2k} \nabla^2 \phi(\mathbf{r}) - j \frac{z}{2k} \nabla \phi(\mathbf{r}) \cdot \nabla \phi(\mathbf{r})\right) \exp[j\phi(\mathbf{r})] \times \\ &\quad \int \exp \left[j2\pi \left(\mathbf{r} - \frac{z}{k} \nabla \phi(\mathbf{r}) \right) \cdot \boldsymbol{\rho} \right] \mathcal{A}_z(\boldsymbol{\rho}) d\boldsymbol{\rho} \\ &\stackrel{\mathcal{F}^{-1}}{\approx} \stackrel{(A.17)}{\approx} \left(1 - \frac{z}{2k} \nabla^2 \phi(\mathbf{r}) - j \frac{z}{2k} \nabla \phi(\mathbf{r}) \cdot \nabla \phi(\mathbf{r})\right) A \left(\mathbf{r} - \frac{z}{k} \nabla \phi(\mathbf{r}) \right) \exp[j\phi(\mathbf{r})]. \end{aligned} \quad (\text{A.22})$$

We further assume smooth sample amplitude $A(\mathbf{r})$ with a small spectrum with respect to sensor sampling frequency $1/\epsilon$. As a result, $A(\mathbf{r} - \lambda z \boldsymbol{\rho}) \approx A(\mathbf{r})$. Thus, and given Eq. (A.22), we may obtain $f_z(\mathbf{r} - \lambda z \boldsymbol{\rho})$ as:

$$f_z(\mathbf{r} - \lambda z \boldsymbol{\rho}) \stackrel{(A.22)}{\approx} \stackrel{(A.21)}{\approx} \left(1 - \frac{z}{2k} \nabla^2 \phi(\mathbf{r}) - j \frac{z}{2k} \nabla \phi(\mathbf{r}) \cdot \nabla \phi(\mathbf{r})\right) A \left(\mathbf{r} - \frac{z}{k} \nabla \phi(\mathbf{r}) \right) \exp[-j\lambda z \boldsymbol{\rho} \cdot \nabla \phi(\mathbf{r})], \quad (\text{A.23})$$

where we neglect the constant phase $\exp[j\phi(\mathbf{r})]$ in the expression.

We should point out another way of deriving $f_z(\mathbf{r} - \lambda z \boldsymbol{\rho})$ is to assume near-field directly on $f_0(\mathbf{r})$, instead of imposing separately on its amplitude and phase as shown previously. Thus, its condition of validity is considered more restrictive. As such, $f_z(\mathbf{r} - \lambda z \boldsymbol{\rho})$ derives as:

$$f_z(\mathbf{r} - \lambda z \boldsymbol{\rho}) \approx \left(1 - \frac{z}{2k} \nabla^2 \phi(\mathbf{r}) - j \frac{z}{2k} \nabla \phi(\mathbf{r}) \cdot \nabla \phi(\mathbf{r})\right) A(\mathbf{r}) \exp[-j\lambda z \boldsymbol{\rho} \cdot \nabla \phi(\mathbf{r})]. \quad (\text{A.24})$$

Notice the small difference in the amplitude term, i.e., $A(\mathbf{r})$ versus $A(\mathbf{r} - (z/k) \nabla \phi(\mathbf{r}))$ in Eq. (A.23).

Final result

With Eq. (A.23), Eq. (A.15) simplifies to:

$$u_z(\mathbf{r}) \underset{\mathcal{F}^{-1}}{\approx}^{(A.23)} A \left(\mathbf{r} - \frac{z}{k} \nabla \phi(\mathbf{r}) \right) \left(1 - \frac{z}{2k} \nabla^2 \phi(\mathbf{r}) - j \frac{z}{2k} \nabla \phi(\mathbf{r}) \cdot \nabla \phi(\mathbf{r}) \right) p_z \left(\mathbf{r} - \frac{\lambda z}{2\pi} \nabla \phi(\mathbf{r}) \right). \quad (\text{A.25})$$

Before deriving the final formula, simply notice reference image $I_0(\mathbf{r})$ is taken under collimated illumination $A(\mathbf{r}) = 1$ and $\phi(\mathbf{r}) = 0$, and is the diffraction pattern of the wavefront sensor optics:

$$I_0(\mathbf{r}) = |p_z(\mathbf{r})|^2. \quad (\text{A.26})$$

Finally, the intensity image is, by preserving only small amount (for $\delta \ll 1$, $(1 + \delta)^2 + \delta^2 \approx 1 + 2\delta$):

$$\begin{aligned} I(\mathbf{r}) &\triangleq |u_z(\mathbf{r})|^2 \\ &\stackrel{(A.25)}{=} \left| A \left(\mathbf{r} - \frac{z}{k} \nabla \phi(\mathbf{r}) \right) \right|^2 I_0 \left(\mathbf{r} - \frac{\lambda z}{2\pi} \nabla \phi(\mathbf{r}) \right) \left[\left(1 - \frac{z}{2k} \nabla^2 \phi(\mathbf{r}) \right)^2 + \left(\frac{z}{2k} \nabla \phi(\mathbf{r}) \cdot \nabla \phi(\mathbf{r}) \right)^2 \right] \\ &\approx \left| A \left(\mathbf{r} - \frac{z}{k} \nabla \phi(\mathbf{r}) \right) \right|^2 I_0 \left(\mathbf{r} - \frac{\lambda z}{2\pi} \nabla \phi(\mathbf{r}) \right) \left(1 - \frac{z}{k} \nabla^2 \phi(\mathbf{r}) \right). \end{aligned} \quad (\text{A.27})$$

Rearranging, with $k = 2\pi/\lambda$, yields:

$$\boxed{I \left(\mathbf{r} + \frac{\lambda z}{2\pi} \nabla \phi \right) = |A(\mathbf{r})|^2 \left(1 - \frac{\lambda z}{2\pi} \nabla^2 \phi \right) I_0(\mathbf{r})}. \quad (\text{A.28})$$

Notice the equivalence between Eq. (A.28) and Eq. (3.3).

B Parameterized Optical Surfaces

We consider three specific types of parameterized lens surfaces to represent lens and freeform surfaces, yet in theory alternative parameterization forms (see [236]) should also work. Surfaces are defined in a Cartesian coordinate system (x, y, z) , with z -axis being chosen as the optical axis (if any).

Recall that we have formulated optical surfaces as parameterized surfaces of parameters $\boldsymbol{\theta}$ in implicit form $f(x, y, z; \boldsymbol{\theta}) = 0$ along with its spatial derivatives $\nabla f(x, y, z; \boldsymbol{\theta})$. Surface normals are normalized spatial derivatives, *i.e.* $\mathbf{n} = \nabla f / \|\nabla f\|$.

B.1 Aspheres

Let $\rho = x^2 + y^2$ since aspheric surfaces are axially symmetric. The sag distance function $g(\rho)$ of aspheric surfaces and its derivative with respect to ρ are:

$$g(\rho) = \frac{c\rho}{1 + \sqrt{1 - \alpha\rho}} + \sum_{i=2}^n a_{2i}\rho^i, \quad (\text{B.1})$$

$$g'(\rho) = c \frac{1 + \sqrt{1 - \alpha\rho} - \alpha\rho/2}{\sqrt{1 - \alpha\rho}(1 + \sqrt{1 - \alpha\rho})^2} + \sum_{i=2}^n a_{2i}i\rho^{i-1}, \quad (\text{B.2})$$

where c is the curvature, $\alpha = (1 + \kappa)c^2$ with κ being the conic coefficient, and a_{2i} 's are higher-order coefficients. In implicit form:

$$f(x, y, z; \boldsymbol{\theta}) = g(\rho) - z, \quad (\text{B.3})$$

$$\nabla f(x, y, z; \boldsymbol{\theta}) = (2g'(\rho)x, 2g'(\rho)y, -1), \quad (\text{B.4})$$

where differentiable parameters $\boldsymbol{\theta} = (c, \kappa, a_{2i})$.

Spherical surfaces are special cases of aspheric surfaces when $\kappa = 0$ and $a_{2i} = 0$ ($i = 2, \dots, n$). For spherical surfaces, there is a closed-form solution to the ray-surface intersection problem in Section 6.2.3, without the need for Newton's iterative method.

B.2 XY polynomials

XY polynomial surfaces extend lens surface representation beyond axial symmetry. The implicit surface function $f(x, y, z; \boldsymbol{\theta})$ and its spatial derivatives are:

$$f(x, y, z; \boldsymbol{\theta}) = \sum_{j=0}^J \sum_{i=0}^j a_{i,j} x^i y^{j-i} + bz^2 - z, \quad (\text{B.5})$$

$$\nabla f(x, y, z; \boldsymbol{\theta}) = \left(\sum_{j=1}^J \sum_{i=0}^j a_{i,j} i x^{i-1} y^{j-i}, \sum_{j=1}^J \sum_{i=0}^j a_{i,j} (j-i) x^i y^{j-i-1}, 2bz - 1 \right), \quad (\text{B.6})$$

where differentiable parameters $\boldsymbol{\theta} = (b, a_{i,j})$.

B.3 B-splines

We employ B-splines [237] to represent high degree-of-freedom freeform surfaces. In general, the sag distance function $g(x, y)$ is represented as a spline of degree (in our case, it is three, *i.e.* the cubic B-spline) on the rectangle area, with predefined number of knots and knot positions. With that, spline functions $S_{i,j}(x, y)$ are fixed, and $g(x, y)$ is determined by spline coefficients $c_{i,j}$:

$$f(x, y, z; \boldsymbol{\theta}) = \sum_i^n \sum_j^m c_{i,j} S_{i,j}(x, y) - z, \quad (\text{B.7})$$

$$\nabla f(x, y, z; \boldsymbol{\theta}) = \left(\sum_i^n \sum_j^m c_{i,j} \nabla_x S_{i,j}(x, y), \sum_i^n \sum_j^m c_{i,j} \nabla_y S_{i,j}(x, y), -1 \right), \quad (\text{B.8})$$

where differentiable parameters $\boldsymbol{\theta} = (c_{i,j})$, and the spatial gradients of the spline functions $\nabla_x S_{i,j}$ and $\nabla_y S_{i,j}$ are efficiently evaluated via modified de-Boor's algorithm [237].

C Publications and Submissions

This dissertation is based on the following works.

1. **Congli Wang**, Xiong Dun, Qiang Fu, and Wolfgang Heidrich. “Ultra-high resolution coded wavefront sensor”, *Optics Express*, 25(12):13736, Jun 2017.
2. **Congli Wang**, Qiang Fu, Xiong Dun, and Wolfgang Heidrich. “Megapixel adaptive optics: Towards correcting large-scale distortions in computational cameras”, *ACM Transactions on Graphics*, 37(4):1-12, Aug 2018 (Proceedings of SIGGRAPH 2018).
3. **Congli Wang**, Qiang Fu, Xiong Dun, and Wolfgang Heidrich. “Quantitative phase and intensity microscopy using snapshot white light wavefront sensing”, *Scientific Reports*, 9(1), Sep 2019.
4. **Congli Wang**, Qiang Fu, Xiong Dun, and Wolfgang Heidrich. “Modeling classical wavefront sensors”, *Optics Express*, 28(4):5273, Feb 2020.
5. **Congli Wang**, Ni Chen, and Wolfgang Heidrich. “Towards self-calibrated computational lens metrology by differentiable refractive deflectometry”, under submission.
6. **Congli Wang**, Ni Chen, and Wolfgang Heidrich. “DiffLens: A differentiable lens design engine”, under submission.

Follows are journal or journal-equivalent publications towards other projects that are not directly related to this dissertation. * denotes equal contribution.

1. Ni Chen*, **Congli Wang***, and Wolfgang Heidrich. “Four-dimensional holographic particle image velocimetry”, *Laser & Photonics Reviews*, May 2021.

2. Qilin Sun, **Congli Wang**, Qiang Fu, Xiong Dun, and Wolfgang Heidrich. “End-to-end complex lens design with differentiable ray tracing”, *ACM Transactions on Graphics* (Proceedings of SIGGRAPH 2021).
3. Simeng Qiu, Qiang Fu, **Congli Wang**, and Wolfgang Heidrich. “Linear polarization demosaicking for monochrome and color polarization focal plane arrays”, *Computer Graphics Forum*, Mar 2021.
4. Ni Chen, **Congli Wang**, and Wolfgang Heidrich. “Holographic 3D particle imaging with model-based deep network”, *IEEE Transactions on Computational Imaging*, 7:288, Mar 2021.
5. Guangming Zang, Ramzi Idoughi, **Congli Wang**, Anthony Bennett, Jianguo Du, Scott Skeen, William L. Roberts, Peter Wonka, and Wolfgang Heidrich. “TomoFluid: Reconstructing dynamic fluid from sparse view videos”. In The IEEE/CVF Conference on Computer Vision and Pattern Recognition (CVPR), Jun 2020.
6. Simeng Qiu, Qiang Fu, **Congli Wang**, and Wolfgang Heidrich. “Polarization demosaicking for monochrome and color polarization focal plane arrays”. In Vision Modeling and Visualization. The Eurographics Association, 2019.

Follows are conference abstracts or patent.

1. **Congli Wang**, Ni Chen, and Wolfgang Heidrich. “Lens design optimization by back-propagation”. In Optical Design and Fabrication Congress. OSA, 2021.
2. Miao Qi, **Congli Wang**, Ni Chen, and Wolfgang Heidrich. “Coded wavefront sensor and non-iterative learning-based reconstruction”. In Imaging and Applied Optics (COSI, IS, MATH, pcAOP). OSA, 2021.
3. Ni Chen, **Congli Wang**, and Wolfgang Heidrich. “Space-time optical imaging framework: Holographic particle tracking velocimetry”. In Imaging and Applied Optics (COSI, IS, MATH, pcAOP). OSA, 2021.

4. **Congli Wang**, Ni Chen, and Wolfgang Heidrich. “Lens design with automatic differentiation”. In Imaging and Applied Optics (COSI, IS, MATH, pcAOP). OSA, 2021.
5. **Congli Wang**, Qiang Fu, Xiong Dun, and Wolfgang Heidrich. “A model for classical wavefront sensors and snapshot incoherent wavefront sensing”. In Imaging and Applied Optics (COSI, IS, MATH, pcAOP). OSA, 2019.
6. **Congli Wang**, Qiang Fu, Xiong Dun, and Wolfgang Heidrich. “Wavefront sensor and method of reconstructing distorted wavefronts”, number US20190265107A1, 2019.